Universidad Autónoma de Madrid

Facultad de Ciencias

Design, fabrication and characterization of photonic crystals for cavity quantum electrodynamics enhanced devices

Thesis presented by Iván Prieto González
to obtain the degree of Doctor of Philosophy in Physical Sciences

2014

Instituto de Microelectrónica de Madrid
Consejo Superior de Investigaciones Científicas

Resumen

En esta tesis, se ha utilizado cristales fotónicos con nano–estructuras cuánticas para conseguir fabricar dispositivos mejorados para experimentos de electrodinámica cuántica en cavidades. Hemos desarrollado varios procesos de fabricación para obtener microcavidades de cristal fotónico en el estado del arte. Varias aplicaciones han sido demostradas durante el curso de esta tesis. Algunas de ellas son presentadas en este manuscrito. En primer lugar, un laser *quasi*–sin–umbral a temperatura ambiente ha sido demostrado en un sistema que consiste en una cavidad de cristal fotónico con una única capa de puntos cuánticos de InAsSb/GaAs de alta densidad. En segundo lugar, se presenta una metodología para estudiar el acoplamiento fuerte entre nanostructuras cuánticas y modos de cavidad con alto factor de calidad y bajo volumen modal mediante diferencias finitas en el dominio temporal.

En tercer lugar, se proponen tres aproximaciones para la obtención de un sistema de punto cuántico acoplado de forma determinista con un modo de cavidad de cristal fotónico. Los resultados están basados en el desarrollo de una estrategia, bien de la fabricación de cavidades de cristal fotónico en posiciones específicas emitiendo en determinadas longitudes de onda, bien especificando el lugar donde se tienen que nuclear los puntos cuánticos. Para fabricar las cavidades de cristal fotónico en posiciones específicas hemos desarrollado un procedimiento de fabricación que hace uso de marcas metálicas de alineamiento, y hemos demostrado precisiones en el posicionamiento mejores que 50 nm. Se han conseguido cavidades fabricadas en una lámina incompleta y luego re–crecidas mediante la técnica de crecimiento por haces moleculares y se ha demostrado su potencial para incorporar uno o varios puntos cuánticos posicionados. Finalmente, hemos demostrado una mejora en la eficiencia cuántica de células solares mediante el uso de cristales fotónicos.

Abstract

In this thesis, photonic crystals with embedded quantum nanostructures were used to achieve enhanced devices for cavity quantum electrodynamics experiments. We have developed several fabrication procedures to obtain *state–of–the–art* photonic crystal microcavities. Several applications have been demonstrated along the course of this thesis. Some of them are presented in this manuscript. First, *near–thresholdless* laser operating at room temperature was demonstrated in a system consisting of a L9–photonic crystal microcavity with embedded single layer of high density of InAsSb/GaAs quantum dots. Second, a methodology was presented to study the strong coupling between quantum nanostructures and cavity modes with high quality factor and low volume by means of finite difference time domain. Third, three different approaches have been proposed towards the deterministic coupling of a single quantum dot with a photonic crystal microcavity mode. Results are based on the development of a strategy either to fabricate PCMS in spectral and spatial specific positions or to specify those positions where the QDs have to be nucleated. To fabricate PCMs in specific positions we have developed a fabrication procedure of photonic crystal microcavities with metallic marks, achieving an accuraccy in the spatial positioning better than 50 nm. Molecular beam epitaxial re–growth of pre–patterned photonic crystal microcavities in a incomplete GaAs slab have been designed, fabricated and tested to demonstrate their capability to integrate one or several isolated QDs. Finally, an enhanced external quantum efficiency in solar cells was demonstrated through the use of a photonic crystal.

Contents

List of Figures

List of Tables

Chapter 1

Introduction

The framework of the present work is the Nanotechnology and Nanophotonics. In this introductory chapter it is presented the concepts of photonic band gap materials, photonic crystals, photonic crystal cavities, as well as an introduction to quantum nanostructures and the fundamentals of the light–matter interaction when those systems are combined.

1.1 Nanophotonics

When Richard Feynman delivered the lecture "There's Plenty of Room at the bottom",[1] the concepts of *nanoscience* and *nanotechnology* were stablished. Nanotechnology aims to handle the matter at the nanoscale, where the interactions among single atoms and molecules are involved. Different fields of science come from nanotechnology, such as nanophotonics, nanoelectronics, nanomechanics, nanoionics and others, depending on the physical porperty we are looking at. To have an idea about how small the nano–issues are, me and a former colleague prepared, cleaned and metalized a human hair and characterized it by scanning electron microscopy (SEM). What we see in Figure 1.1a is the resulting metalized human hair. Figure 1.1b shows a nano–device on a semiconductor GaAs wafer with embedded quantum light nanostructures. The nano–device consists of an array of holes with one missing in the center. This is a photonic crystal nano–cavity and when designed properly, might serve, for instance, as a very small laser. The comparison between both pictures provide an idea about the size of those devices, on the order of 10 to 100 times smaller than the diameter of a human hair. In

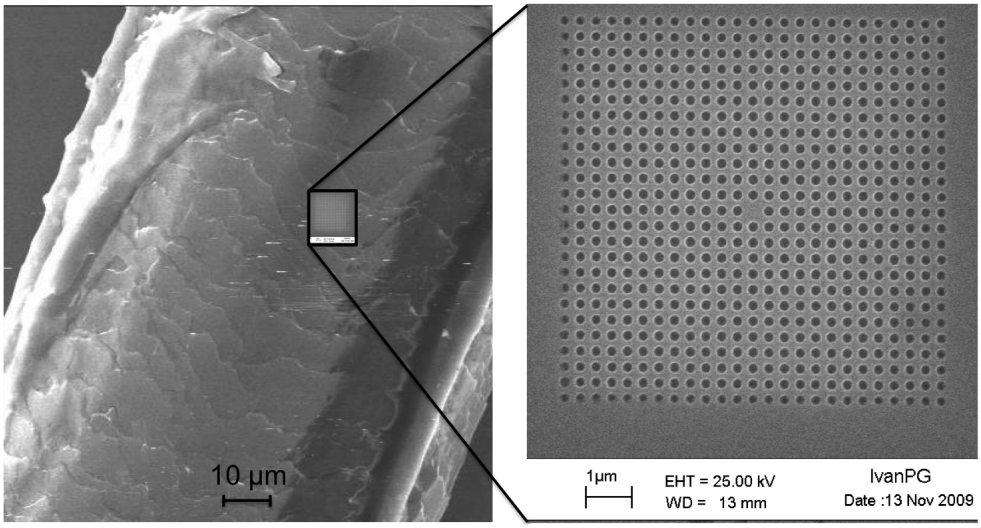

Figure 1.1: **What is the size of a nano–device?** To realize how small are the nano–photonic devices we compare them with a more conventional object. (left) A scanning electron microscopy (SEM) image of a cleaned human hair is presented. (right) A SEM image of a fabricated photonic crystal cavity is shown. Inset in (left) is shown for comparison purpose.

particular, nano–photonics is an exciting field which deals with the interaction of light with matter at the nanometer size scale. During the past decade, the field of nanophotonics has witnessed an exponential growth, mainly driven by the increase demand for on–chip optical signal processing. Nevertheless *nanophotonics* does not claim to supply the best solution for every problem. Instead, it provides exciting opportunities to both understand fundamental mechanisms of quantum electrodynamics occurring in the nanoworld and stablish new technologies for the development of novel devices, more efficient and with a lower consumption. In the context of nanophotonic devices (active light sources or detectors or passive devices), it is particularly interesting introduction of photonic crystals and quantum nanostructures. The major work in the current thesis stem from the combination of those large two fields. A brief introduction to those concepts is introduced in the following sections.

1.2 Photonic crystals

Since the early proposal of the concept of *photonic crystal*,[2, 3] an exponential growth was experienced, thus demonstrating the potential of those devices in

many applications within the framework of the nanophotonics. *Photonic crystals* are ordered structures in which two (or more, in general) media with different refractive indices are arranged in a periodic form. Photonic crystals can be classified according to the dimensionality of the material distribution. We refer to one–dimensional photonic crystals (or Bragg mirror) when the material distribution is assembled in layers of different materials with a certain thickness. In two–dimensional photonic crystals, the material arrangement is in the same plane, thus having a periodic distribution of materials in an infinite depth. Three-dimensional photonic crystals involve an assembly of two materials in the three dimensions.

1.2.1 Photonic bandstructure and bandgap

The symmetry exhibited by the refractive index distribution in photonic crystals is analogous to the ordered atomic arrangement in solid state crystals. In the same way as the periodicity of solid state crystals determines the bandstructure and the conduction properties of the electrons, the periodical structuring of photonic crystals at wavelength scales has turned out to be main viable approach towards the control of the energies and of the fluxes of light ocurring in those materials; we thus refer to *photonic bandstructure*, see an example in Figure 1.2.

Therefore, light with a certain energy and wavevector must be compatible with the states given by the photonic bandstructure of the system is passing through. In particular, there might be a range of energies and wavevectors for which light cannot propagate. When this inhibition is extended to all wavevectors for a certain range of energies, we refere to a *photonic bandgap*. In addition, if the photonic bandgap is manifested for any polarization state, we refer to a *complete photonic bandgap*. Those systems presenting inhibition on the propagation of light within a certain range of frequencies are called *photonic bandgap materials*. It has been here referred to photonic crystals and photonic bandgap materials. It is worth noting that photonic crystals only refer to a spatial periodic arrangement of different materials. The photonic bandgap materials are a particular case of photonic crystals in which a photonic bandgap is present. For simplicity and in agreement with the scientific community, we will refer along the manuscript to photonic crystals in any case.

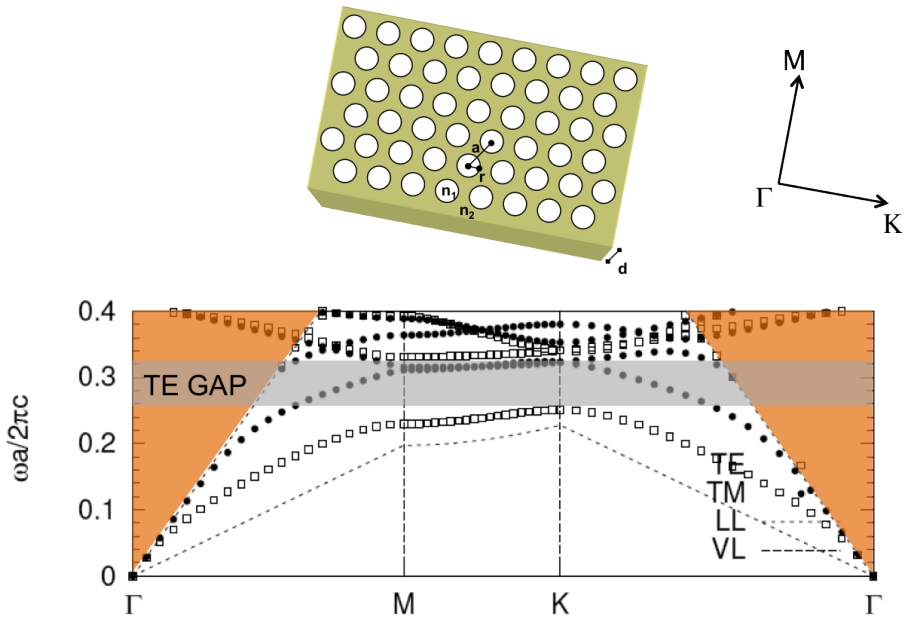

Figure 1.2: **Photonic crystal bandstructure.** Bandstructure of a 2D photonic crystal slab with parameters $a = 250$ nm, $r = 0.30a$ and $d = 140$ nm for a GaAs slab.

1.3 Photonic crystal cavities

In complete analogy with the donor or acceptor defects that might be present within the electronic bandgap in solid state crystals, we can also induce defects within the photonic crystal lattice. This way we can introduce a allowed states within the bandgap for a certain structure. Light coupled to a defect state cannot propagate through the crystal lattice due to the presence of the photonic bandgap, and might be spatially confined in the region where the point defect is created. We will refer to those systems as *photonic crystal cavities*, and the set of available states to photons within the bandgap constitutes the mode structure of the cavity. That fact leads to the concept of *photonic crystal cavities*, where light is spatially confined in the photonic crystal defect. If we construct a linear defect (for instance by removing one of the materials in a row), we might provide a channel for light to be guided from one position in the wafer to another one; we call those systems *photonic crystal waveguides*. In the last decade there has been a growing number or research activities in creating point and extended defects in photonic crystals to produce microcavities and to introduce waveguiding structures, in order to build photonic crystal-based optical circuitry. Under such conditions, if light with this

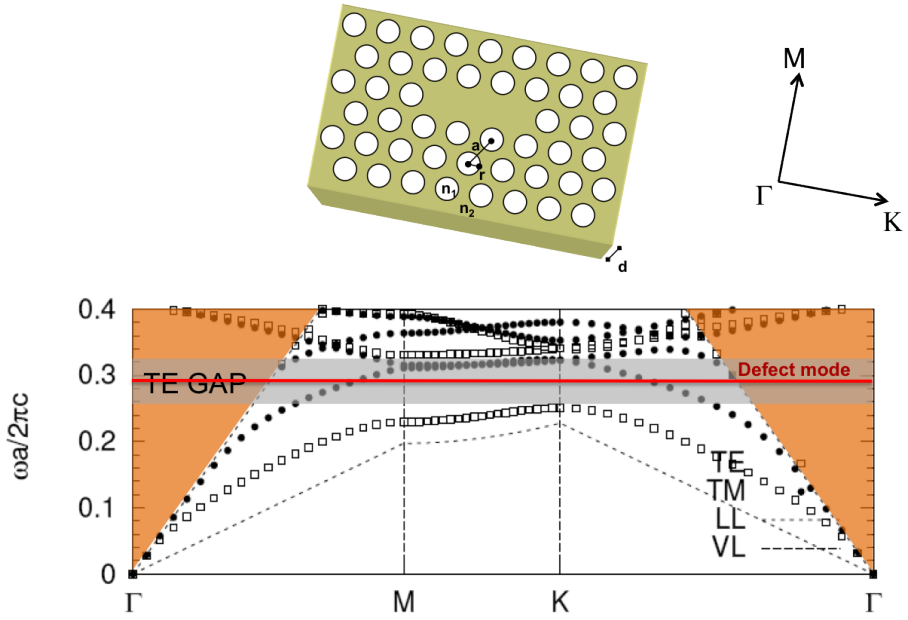

Figure 1.3: **Defects in a photonic crystal.** Bandstructure of a 2D photonic crystal slab with parameters $a = 250$ nm, $r = 0.30a$ and $d = 140$ nm for a GaAs slab. The creation of a defect introduces defect states within the bandgap. In this structure a and r refer to the lattice constant and the radius, and n_1 and n_2 to the refractive index of the cylinder and the host material, respectively.

range of energies is coming from outside, it is reflected, and if light is generated within the structure, it cannot propagate along the crystal. In the work presented in this document, the *photonic crystal* structures are constituted by an array of air cylinders with hexagonal symmetry, within a semiconductor material (either GaAs, InP or InGaP).

1.4 From bulk materials to quantum nanostructures

For systems with a layer thickness similar or smaller than the de Broglie wavelength of thermalized electrons the energy–momentum relation for a bulk–material is no longer valid. In a free–space the interaction potential of the electrons with the medium is either null or constant. In the case of photons, no spatial variation of n occurs and therefore:

$$\begin{aligned} k &= \frac{2\pi}{\lambda} \\ E &= \frac{hc}{\lambda} \\ \omega &= ck \end{aligned} \tag{1.1}$$

It is worth noting that, in the case of electrons,

$$\begin{aligned} E &= \frac{\hbar^2 k^2}{2m} \\ \omega &= \frac{\hbar k^2}{2m} \end{aligned} \tag{1.2}$$

where k is the wavevector (associated either to the electron or photon), $\lambda(\omega)$ is the wavelength (angular frequency) of the photon and m is the mass of the electron. It is clearly seen that even though analogous descriptions can be used for photons and electrons, $E(k)$ is linearly dependent for photons and presents a quadratic dependence for electrons. As one may infer, for free–space propagation, all values of frequency and energies for photons and electrons are permitted. We refer to those permitted states as the band structure, which explains the characteristics of the dependence of the frequency or energy on the wavevector $\mathbf{k}$.

1.4.1 Quantum–wells, –wires, –rings, –dots

In a similar way light can be prohibited to travel through a medium in either zero–, one–, two–dimensions (as explained in the previous sections), the alteration of the bandstructure for electrons can confine them in zero–, one– or two–dimensions, giving raise to the so–called quantum dots (QDs), quantum wires (QWrs) or quantum wells (QWs), respectively. The density of states for electrons $D(E)$ is given by the number of energy states between the energies E and $E + \mathrm{d}E$. Depending on the dimensionality of the medium, the $D(E)$ provides a set of available states that electrons may occupy.

1D electron confinement: quantum well

A quantum well is a structure in which a thin layer of a smaller bandgap semiconductor is sandwiched between the two layers of a wider bandgap semiconductor. The confinement of electrons and holes in those systems is one–dimensional. When the smaller bandgap semiconductor is along one line, we refer to a quantum wire. The structure is one–dimensional, and the confinement of electrons and holes is two–dimensional.

2D electron confinement: quantum wire (QWr)

Quantum wires (QWr) are one–dimensional structures acts as a potential that confines electron and holes in 2D.

3D electron confinement: quantum dot (QD) and quantum ring (QR)

In a quantum dot (QD) the electrons are confined in all three directions. In this case, the allowed energies are discrete so that $D(E)$ is represented by a sequence of delta functions at the allowed energies. Although QDs are composed of tens of thousands of single atoms, they present a discrete bandstructure that leads to call them artificial atoms. Particularly interesting are the quantum rings (QRs), which ideally are like QDs with a hole in the middle. Due to its particular shape, QRs are very interesting for their study under magnetic field.[4]

Both electronic and optical properties of semiconductors reflect manifestations of the quantum confinement that have been found to have technological applications. In the next section we describe some of their application, specifically applied to light sources.

1.5 Light–matter interaction: QD-cavity coupling

Let us we assume a QD as a two level system (E_1 and E_2) located in cavity sustaining a set of cavity modes that provides a set of available states for photons. If the energy of the photon associated to a mode coincides approximately with $E_2 - E_1$, we say those photons match the QD energy–level difference. This kind of interactions are studied by the field of cavity quantum electrodynamics (c-QED). We summarize below the results of this analysis.

1.5.1 Light–matter interaction mechanisms

The interaction between the nanostructure and the cavity mode can result only in three different procedures, i. e., spontaneous emission, stimulated emission and absorption.

Spontaneous emission

One photon is spontaneously emitted by a QD when an electron in the upper state (2) decay spontaneously to the lower state (1). This photon energy is transferred to the cavity mode. That mechanism is the fundamental of the spontaneous emission and the transition occurrence has nothing to do with the amount of photons that are already in the mode.

Absorption

If a photon of the cavity transfer its energy to the QD, an electron that is in the lower state can eventually absorb such energy and promote to the upper state. This action is called absorption and can be induced by the photon of the mode and, thus, only occurs when the mode has at least one photon.

Stimulated emission

If the QD host an electron in the upper state and the cavity mode has one photon, the QD can be stimulated to emit another photon into the same mode. The mechanism occurring is the stimulated emission and it is absolutely the inverse to the

absorption. The emitted photon conincides in propagation direction, polarization and phase with the one it was estimulated through.

1.5.2 Weak– and strong–coupling regimes

For the explanation of the weak– and strong–coupling, we will set up the starting system. Let us consider a single QD embedded in a microcavity and assume that the excitonic transition is on–resonance with the fundamental cavity mode. We prescribe $|e\rangle$ and $|g\rangle$ as two different states of the QD in which the electron is in the upper energy level or in the lower level, respectively. This system can be described by the Jaynes–Cummings Hamiltonian:

$$H = H_{\mathrm{X}} + H_{\mathrm{C}} + H_{\mathrm{int}} \tag{1.3}$$

where H_{X} and H_{C} are the excitonic Hamiltonian and the cavity–mode Hamiltonian; H_{int} accounts for the interaction between the excitonic transition and the cavity mode, and is referred as exciton–mode Hamiltonian. Those terms are expressed as:

$$\begin{aligned} H_{\mathrm{X}} &= \hbar\omega\sigma_z \\ H_{\mathrm{C}} &= \hbar\omega\left(a^{\dagger}a + \frac{1}{2}\right) \\ H_{\mathrm{int}} &= i\hbar\left(g\left(\vec{r}_{\mathrm{X}}\right)a^{\dagger}\sigma_{-} - g^{*}\left(\vec{r}_{\mathrm{X}}\right)\sigma_{+}a\right) \end{aligned} \tag{1.4}$$

In that formulation, ω is the excitonic transition frequency (which also corresponds to that of the cavity mode), $\sigma_{\mathrm{z}} = \frac{1}{2}\left(|e\rangle\langle e| - |g\rangle\langle g|\right)$ is the population operator. The coupling factor $g\left(\vec{r}\right)$ is expressed as:

$$g\left(\vec{r}\right) = g_0\psi\left(\vec{r}\right)cos(\xi) \tag{1.5}$$

where:

$$\begin{aligned} g_0 &= \frac{\mu}{\hbar}\sqrt{\frac{\hbar\omega}{2\epsilon_{\mathrm{M}}V_{\mathrm{eff}}}} \\ \psi\left(\vec{r}\right) &= \frac{E\left(\vec{r}\right)}{\left|E\left(\vec{r}_{\mathrm{M}}\right)\right|} \\ cos(\xi) &= \frac{\vec{\mu}\cdot\hat{e}}{\mu} \end{aligned} \tag{1.6}$$

Here, g_0 is the Rabi frequency, $\psi(\vec{r})$ is a factor that accounts only for the position dependency and $cos(\xi)$ only considers the relative orientation between the emitter and the polarization of the cavity mode. In addition, $\vec{\mu}$ is the dipole moment which corresponds to the emission of the QD, ϵ_{M} is the permitivity at the position $\vec{r}_{\mathrm{M}}$ where the electric field $|\vec{E}|$ is maximum, $\hat{e}$ is the unitary vector along the orientation of the cavity mode and V_{eff} corresponds to the cavity mode volume. Under the conditions of a dipole aprroximation, H_{int} can be expressed as:

$$H_{\mathrm{int}} = -\vec{\mu} \cdot \vec{E} \tag{1.7}$$

The system we are considering presents two kind of losses; on one hand, losses due to the cavity performance and, on the other hand, those associated to any other source of losses. The cavity mode decay rate κ is related to the Q of the cavity mode and the excitonic dipole decay rate γ is limited by other source of losses. In this stage, whenever in our system $g(\vec{r}_{\mathrm{X}}) > \kappa, \gamma$ we will refer to the weak coupling regime, where the Purcell effect dominates the dynamics of the system. On the other hand, if $g(\vec{r}_{\mathrm{X}}) < \kappa, \gamma$, the strong coupling takes place and Rabi oscillations occur. In other words, the time scale of the coherent exciton–mode coupling in comparison with the irreversible recombination channels (either radiative or non–radiative) establishes the two regimes. That channels with the shortest decay time is the one that have more chances to happen first. Therefore, in the case of weak coupling, the irreversible decay is shorter than the coherent decay and viceversa in the case of a system under strong coupling. It is worth noting during the Rabi oscillation process there is an exchange of energy between the cavity mode and the QD excitonic transition.

Purcell Effect

We can obtain the emission decay rate for a system under weak–coupling:

$$\Gamma = \frac{4Q}{\omega} |g(\vec{r}_{\mathrm{M}})|^2 \tag{1.8}$$

If the QD rather were in a surronding free–space, the spontaneous emission rate would be given by:

$$\Gamma_0 = \frac{\omega^3 \mu^2}{3\pi\epsilon_0 \hbar c^3} \tag{1.9}$$

The Purcell effect accounts to the ratio between the emission rate of the QD when coupled to the cavity mode and that when it is emitting in the free space. We define the Purcell factor (F) in the optimum conditions for the coupling, i.e., a QD located at the maximum of the cavity mode and with a polarization of the excitonic transition parallel to that of the cavity mode:

$$F = \frac{\Gamma}{\Gamma_0} = \frac{3\lambda^3\epsilon_0}{4\pi^2\epsilon_{\mathrm{M}}}\frac{Q}{V_{\mathrm{eff}}} \tag{1.10}$$

If the Purcell factor is large, we then conclude that the QD may emit much faster when embedded in the cavity compared to that emitting in the free–space.

Rabi oscillation

Following the above criteria, the strong coupling regime takes place when:

$$g\left(\vec{r}_{\mathrm{X}}\right) < \kappa, \gamma \tag{1.11}$$

Under those conditions, Rabi oscillations account and the rate at which the exchange energy occurs is faster than any other dissipative (incoherent) rates of the system. Those Rabi flops between the photonic and excitonic states are produced at twice the Rabi frequency ($2g_0$) with the dissipation given by the cavity mode quality factor, Q (similar dissipation as in the case of weak coupling). Those strongly coupled systems are of great interest on the quantum communication or quantum information systems.

1.6 Applications of photonic crystals and photonic crystal cavities

In the previous sections, powerful capabilities of the photonic crystals and photonic crystal microcavities where shown to handle the light emitted by the quantum nanostructures almost at will. There is a bunch of applications of the photonic crystal structures based on the engineering of their photonic bandstructure and mode structure. Among all the applications involving photonic crystal structures, I will breafly describe those that were addressed in this thesis.

1.6.1 Photonic crystal cavities embedding QDs to improve solid state lasers

A major commercial application of the quantum–confined semiconductors is in producing energy–efficient and highly compact lasers. Optical communications is an important area of potential application for photonic crystals, where they can be used to produce a light source consisting of low–threshold lasers and photodetectors with enhanced sensitivity. A photonic crystal with a well–defined defect channel can be used to confine light in the defect region and guide it. Guiding through well–controlled defect channels allows sharp bending of light without significant optical loss. Light might be transmitted through a line defect made in a photonic crystal. A particularity that photonic crystal waveguides offer is that the extended defect region can have sharp bends (for instance, a 90° bend) with no considerably optical loss. This effect might allow photonic crystal based chips to miniaturize further. Finally, a photonic crystal platform provides an opportunity for dense integration of emitter, receiver, amplifier transmitter and routs on the same chip. These both active and passive functions can be integrated to produce a true photonic chip. The telecommunications bands are centered in the 980-1300-1550 nm windows. Efficient light sources comprising photonic crystal microcavities and quantum dots emitting in those bands are a hot topic nowadays. The use of InAsSb QDs emitting in the 1.3 μm spectral window within a photonic crystal cavity produce optimized light sources operating at room temperature. The development of those technological procedures has allowed us to fabricate highly efficient light sources emitting at room temperature in the 1.3 μm.

1.6.2 Photonic crystal cavities with embedded QDs as test bed systems for cQED experiments

Cavity quantum electrodynamics (c-QED) is the field that studies the interaction of a quantum particle with a cavity mode. Self–assembled quantum dots lying within a photonic crystal cavity present unavoidable characteristics that might make those systems obscure depending on the properties they exhibit. In particular, quantum dots support a wide variety of single– and multi–particle bound and extended states. Spectra from devices incorporating a set of quantum dots show dozens of emission lines that vary in intensity and linewidth. To get rid

of that set of inconveniences, and to achieve a more ideal system containing a single quantum dot embedded in a photonic crystal cavity, both spectral and spatial matching of the quantum dot to the photonic cavity mode is required to accomplish experiments in the field of c-QED. This fact motivated us to develop a procedure to position a single QD in a photonic crystal cavity.

1.6.3 Photonic crystals to increase the efficiency of solar cells

Solar energy is an abundant and non–polluting source of energy. Nevertheless, the installation of solar cells for energy production is still dependent on subsidies in most parts of the world. One way of reducing the costs of solar cells is to decrease their thickness. This will reduce material consumption and, at the same time, unlock the possibility of using cheaper lower quality solar cell material. However, a thinner solar cell will have a higher optical loss due to insufficient absorption of long wavelength light. Therefore, light–trapping must be improved in order to make thin solar cells economically viable. In this respect, photonic crystals on the surface of the solar cells might be capable to reduce the reflection in the air–semiconductor interface. Therefore, it is possible to design photonic crystal structures to favour the transmission of the incident light, and, therefore, the absorption, thus leading to an enhancement of the efficiency.

1.7 Goals and overview of this Thesis

The goal of this Thesis consists, basically, of the development of a fabrication procedure of photonic crystals that allows to fabricate efficient ligh sources.

In particular, a multi–step fabrication process for GaAs–based materials has been developed. It is based on the use of a hard mask (SiO_x), ZEP–520A resist, electron beam lithography (EBL), reactive ion beam etching (RIBE) and reactive ion etching–inductively coupled plasma (RIE–ICP) and a wet etching. Such scheme is presented in Chapter 3. The acquired fabrication technology allowed us to fabricate a novel laser based on a photonic crystal microcavity (PCM) that embedded InAsSb quantum dots (QDs), operating at room temperature in the 1.3 μm telecom window. This result is presented in Chapter 4.

Additionally, we have followed several approaches towards the deterministic

coupling of a single–QD and a PCM. First, we got insights on the strong coupling regime by analyzing the effects of a quantum well (QW) embedded in a PCM under the strong coupling regime. Such a result is presented in Chapter 5. The first strategy consisted of the fabrication of a pre–patterned PCM in an partial GaAs slab. At this stage an oxide in a specific position was performed with local oxidation lithography by atomic force microscopy (LOL–AFM). The epitaxial re–growth of the slab was performed up to the target thickness was completed. During this process a InAs QD was nucleated in the desired position given by the removed oxide. We called this approach "Re–grown cavity" and is presented in Chapter 6. The holes that conform the PCM evolve in shape and size during the re–growth process and the performance of the structures is degraded. Therefore, we have studied in Chapter 7 the photonic properties of PCMs fabricated through the re–growth process in comparison to the regular cavities fabricated following a regular top–down process. To overcome such an inconvenience we have proposed a second strategy that involved again the LOL–AFM in specific positions but with a non–re–grown (or regular) cavity. To this aim, we have designed and fabricated in a partial slab pre–patterned ruler and alignment marks to fabricate the oxide in a location with given coordinates. After the completion of the re–growth process to complete the slab thickness, the cavity will be fabricated in the desired position in the proper wavelength. This approach was called "Etched ruler" and is presented in Chapter 6 The last approach, referred to as "Golden ruler", involves an epitaxial material with embedded self–asembled QDs over which a mound feature in defined in the surface. The strategy follows with the fabrication of metallic ruler and alignment marks that enclose a region in which we selected a QD. We get the coordinates of the mound feature and fabricate the cavity as a last step. The whole procedure is described in Chapter 8.

As an application of the application of photonic crystals, Chapter 9 includes the demonstration of the improvements experienced by a solar cell when a photonic crystal pattern is performed on the top surface, which favours the transmission of specific wavelengths onto the cell.

Chapter 2

Fabrication of photonic crystal structures

To obtain photonic crystal structures we have developed several fabrication procedures, depending on the characteristics of the structures and the epitaxial material. This chapter provides information of the different equipments and techniques we have used.

Introduction

In this section, we describe the different tools and techiques used for the realization of the devices presented along the course of this thesis. To perform suspended photonic crystal microcavities in GaAs–material, a multistep procedure is necessary. As indicated in Chapter 1, to arise some of the effects predicted by the field of c–QED, it is necessary to optimize the figure of merit Q/V_{eff} of the photonic crystal microcavity mode. To this aim, we adopted L7– or L9–photonic crystal microcavities and tried to maximize the experimental Q.

L7– and L9–photonic crystal microcavities

It is worth noting that there is a broad set of types of photonic crystal cavities whose designs indicate better performance than those of L7– and L9–photonic crystal microcavities.[5, 6, 7, 8, 9, 10, 11, 12] Nevertheless, we have selected those two types of cavities for this thesis mainly due to fabrication consideratios. Although finite difference time domain (FDTD) simulations on other types of

cavities provide larger Q–values and smaller V_{eff}–values, it is worth saying that those cavities are more difficult to be fabricated because they often require accurate tuning of one or several holes, either in size or position. On the contrary, L7– and L9–photonic crystal microcavities (PCMs) do not need of such accurate tunings to support high–Q. Therefore, we adopted only to suppress either 7– or 9–holes of an hexagonal lattice.

Top–down technological procedures

To fabricate L7– or L9–PCMs we followed a so–called top–down technological procedure. After the design of the epitaxial structure, the deposition of a SiO_x hard mask and the coating with a thin film resist, a pattern drawing is performed with electron beam lithography (EBL) onto the resist. After the developing and the post–bake a dry etching is released to transfer the pattern to the hard mask. A subsequent dry etching by means of inductively coupled plasma etching–reactive ion etching (ICP–RIE) is performed to transfer the pattern to the active GaAs slab. The last step consists of the removal of the remaining hard–mask material as well as the sacrificial layer underneath the photonic structures by a selective wet etching. In the following, both the tools and the equipments used are briefly presented.

Molecular beam epitaxy: starting material

The samples designed and processed along the course of this thesis were grown by the molecular beam epitaxy (MBE) technique.[13] This technique provides the possibility of growing heteroepitaxial material y a proper control over the interface quality. In addition, a large control on the material composition, thickness and roughness of materials such as GaAs, $Al_xGa_{1-x}As$, InP, InGaP is obtained. Roughness on the epitaxial material limits dramatically the performance of the cavities,[14] and therefore, an effort was carried out by growers to achieve the maximum performance of the epitaxial material and thus, achieve high–Q.

Plasma enhanced chemical vapour deposition

The plasma enhanced chemical vapour deposition (PECVD) is a technique for depositing a variety of thin films at lower temperatures in comparison to those

used in CVD or MBE reactors. As an example, SiO_x layers were grown for this work at 300 °C, whereas in an MBE equipment the working temperature for the growth of GaAs is 570 °C. PECVD makes use of an electrical energy to generate a discharge (plasma) through which the energy is transferred to a gas mixture. Therefore, the gas is transformed into several species, *i. e.*, ions, neutral atoms, reactive radicals, etc., which, depending on the chemical properties of the substrate and its interaction with those species, producing either an etch of the substrate or a deposition of a thin film over the substrate. Since the formation of the species is produced in the gas phase, it is possible to maintain the substrate at low temperature, which is an advantage of this technique and it is often a requisite in the fabrication process. We have used a PECVD to deposit thin layers of SiO_x that served as hard mask layers for etching procedures. The thickness of those layers was from 85 to 300 nm depending on the purpose.

Spin–coating: a thin layer of resist

The spin–coating tool is used to deposit a thin and homogeneous layer of resist over the hard–mask. The techique consists of the deposition of one or several droplets of resist (depending on the size of the sample) and the revolution at high speeds (1000–6000 rpm). In general, for the fabrication of photonic crystal microcavities, a layer of ZEP–520A 365 nm thick was deposited. Although we normally used ZEP–520A resist, we also worked with PMMA–A4, HSQ (FOX–12, FOX–14 and FOX–17) as electron sensitive resits.

e–beam lithography: generation of the pattern in the resist

Once we have deposited the resist, an electron beam exposes the resist. A large control on the drawing and the physical parameters of the beam (voltage, current, working distance, etc.) is necessary to overcome unexpected results. After the completion of the EBL, we proceed with the developing process. The electron beam alters the physical properties of the resists in those positions where a dose is deposited, and a selective developing process is capable to remove those altered resist regions (in case of positive resits) or those where the electron beam did not expose (case of negative resits). In case of the fabrication of photonic crystals, it is important to address the phenomena referred to as Proximity effect.[15] In an array of holes in a photonic crystal, for instance, the size of each of the holes is

not only due to the local exposition of the electron beam in that region, but it is also altered by the exposure of the surrounding holes. A key requirement is that the resulting holes should have the same size and to prevent this imperfection, we correct the dose of each of the holes by considering the effect of their neighbouring holes. This is known as Proximity effect correction and we have run Montecarlo simulations to overcome such a problem. The main parameters involved in the EBL processes carried ou were: beam current of 20 pA, beam voltage of 30 kV, writing field of 100 μm^2

Dry etching I: reactive ion beam etching: transfer to the hard mask

After the developing process, the pattern is defined onto the resist. We then transfer the pattern to the hard mask through the reactive ion beam etching technique. A mixture of CHF_3:N_2 was selected to drill the SiO_x, using the ZEP–520A resist as a mask. The selectivity of such a process is aproximately 1:1, i.e., we etch the mask and the SiO_x at the same rate.

Dry etching II: inductively coupled plasma–reactive ion etching: transfer to the active slab

The next step consists of the transfer of the patter to the active semiconductor slab. We have developed mainly two etching procedures for the realization of photonic crystals in GaAs; one of them involving low temperature (-10 °C), Cl_2, N_2, Ar, that was practiced either with the presence of a hard mask of SiO_xor directly through the resist. We also made use of the good properties of the inductively coupled plasma etching technique and, a mixture of BCl_3:N_2 was optimized to reach vertical and smooth holes.[16]

Using the SiO_x layer as a mask, we

Wet etching: membrane release

The last step consist on the release of the membrane and the removal of any dust or debris both on the top surface and underneath the photonic structure. The layer underneath the GaAs active slab consists of an AlGaAs layer, that is selectively removed through a diluted HF solution. We have observed that as we

decrease the concentration of the HF solution, flake structures arise underneath the slab. As long as we increase the concentration of the HF solution, the density of flakes is considerably reduced, being inversely proportional to the etch rate.

Chapter 3

Fabrication of high quality factor GaAs/InAsSb photonic crystal microcavities by inductively coupled plasma etching and fast wet etching

I. Prieto,[1] L. E. Muñoz–Camúñez,[1] A. G. Taboada,[1,2] C. Robles,[1] J. M. Ripalda,[1] and P. A. Postigo[1]

J. Vac. Sci. Technol. B **32** 011204 (2014)

[1]IMM–Instituto de Microelectrónica de Madrid (CNM–CSIC), Isaac Newton 8, PTM E–28760, Tres Cantos, Madrid, Spain

[2]Laboratory for Solid State Physics, ETH Zürich (ETHZ) HPF F2 Otto–Stern Weg 1 CH–8093 Zürich, Switzerland

3.1 Context & motivation

Photonic crystal cavities have been demonstrated as ideal for systems that handle the light at the nano–scale. Therefore, those systems were used to fabricate novel lasers, detectors, single photon emitters, test–beds for cQED experiments etc. A *figure of merit* that evaluates the performance of such systems is given by the quality factor (Q) and mode volume (V_{eff}) ratio (Q/V_{eff}). In general, the larger ratio, the better the performance of the cavity we might expect. One might think that the comparison between the ideal and actual values obtained for V_{eff} does not differ much; on the contrary, Q is rather largely affected by imperfections on the structure. Q can be reduced by orders of magnitude in the fabricated devices due to inhomogeneities in the hole size, roughness in the sidewalls, non–vertical holes, presence of debris either over, below or within the structure and others (absorption and other light or carrier–trapping mechanisms). The fabrication is based in multi–step procedures each of them involving an specific equipment or technique that needs to be improved and thus overcome the above mentioned drawbacks. As a consequence of those many effects, the achievement of the right fabrication parameters and make them reproducible often take a very long time. The reproducibility along the fabrication procedure is affected not only by the system itself, but also due to other processes in a multi–user environment.

3.2 Contribution

My contributions to this work are:

- Design of the epitaxial structure,
- Design of the L9–photonic crystal microcavity,
- Development of the fabrication procedures,
- Fabrication of the samples,
- Partial optical characterization of the devices,
- Analysis and writing of the results.

3.3 Publication

3.3.1 Abstract

In this work we demonstrate high quality factor GaAs–based L9 photonic crystal microcavities (PCMs) with embedded InAsSb quantum dots with emission in 1.3 μm at room temperature. The fabrication process uses reactive ion beam etching with a CHF_3/N_2 gas mixture and reactive ion etching with a BCl_3/N_2 gas mixture to form PCMs on air–suspended slabs. An optimum N_2 partial flux content of 0.65 and a successful removal of deposits formed during the membrane release by a fast wet etching in HF provide optical quality factors (Q–factors as high as 30000). In what follows, it is presented the fabrication procedures followed in order to realize high–quality factor photonic crystal microcavities (PCMs). A technological multi step procedure, based on electron beam lithography (EBL), and plasma etching by means of both reactive ion beam etching (RIBE) and inductively coupled plasma reactive ion etching (ICP–RIE) are practiced to obtain the hole pattern onto the active slab (either InP or GaAs based materials). A last step based on a wet chemical etching is used to suspend the photonic structure.

3.3.2 Introduction

Photonic crystal microcavities (PCMs) provide a strong localization of light, since they may exhibit small mode volume (V_{eff}) and a large quality factor (Q). When embedded in a PCM, quantum nanostructures may be tuned to a high–Q/V_{eff} mode and interesting applications arise, such as efficient LEDs,[17] lasers,[18, 19, 20, 21, 22] or filters.[23] In addition, such systems can be test beds for cavity quantum electrodynamics (c–QED) effects.[24, 25, 26, 8, 27, 28] Both classical and quantum light sources working on the telecom windows are crucial for quantum key distribution or quantum information. Research groups working on state–of–the–art nanotechnology have produced photonic systems within the telecommunications O–band (1260–1360) nm such as efficient single photon emitters,[29, 30] electrically injected LEDs[31] or low threshold lasers,[32] with Q–factors of 9700 in a nanobeam,[33] 13000 in a microdisk,[12] 17000 in a H1–PCM,[34] 15000 and 24000 in a L3–PCM.[35, 36] The achievement of high Q on these systems plays an important role towards the realization of efficient light sources. This work shows the fabrication of suspended PC–based systems with

high Q (up to 30000) GaAs based L9 PCMs with emission in 1.3 μm at room temperature (RT) through a careful control of the dry and wet etching parameters.

3.3.3 Design of the L9 photonic crystal microcavity

L9–type PCMs belongs to the Ln–type PCMs, which consists of a periodic lattice of air holes with hexagonal symmetry with 9 consecutive missing holes in the ΓK direction. Contrary to other types of photonic cavities, such as nanobeams, H1 or L3–PCMs, which often present high Q/V_{eff} through a careful control in the size and the position of several holes, the L9–PCMs provide large Q/V_{eff} values with no need of tuning any of the holes (either in size or position); this makes L9–PCMs very robust to fabrication imperfections. We have designed L9 configurations to operate in the 1.3 μm optical telecom window, based in GaAs material. The structure consists of a GaAs slab (190 nm thick) grown by molecular beam epitaxy (MBE) on top of an $Al_0.70Ga_0.30As$ sacrificial layer (500 nm thick). The slab contains a single InAsSb QDs layer emitting at 1.3 μm at RT.[36, 37, 38] The average QD surface density, estimated from transmission electron microscopy (TEM) measurements, is $\sim 10^{10}$ cm^{-2}. Figure 3.1a shows a photoluminescence spectrum of an L9–PCM fabricated on this epitaxial material. Four sharp resonances are observed and identified as the first high–Q even modes. We have reproduced the L9 mode structure by three dimensional finite difference time domain (3D–FDTD) calculations (insets Figure 3.1a),[39] to estimate their optical properties, i. e., wavelength λ, Q, mode effective index n_{eff}, and V_{eff} (see Table 3.1) as well as to determine the optimum structural parameters of the PCMs, pitch a, hole radius r, and slab thickness d (not shown). Since the fundamental mode exhibits the highest Q/V_{eff}, it is the preferred mode to be coupled to the QD emission. The electric field profiles ($|E|^2$) of the fundamental mode and the first three excited modes are shown in the insets of Figure 3.1a. A scanning electron microscope (SEM) image of an L9–PCM is displayed in Figure 3.1b. The design of the structural parameters of the L9–PCMs has been optimized to maximize the Q of the fundamental mode while emitting in the 1.3 μm optical telecom window. From the simulations we have obtained the optimum parameters for the slab thickness $d = 190$ nm, the lattice constant $a = 350$ nm, and the radius of the holes $r = 100$ nm, and we have used them as target values to fabricate high Q L9–PCMs tuned to the emission of the InAsSb QDs around

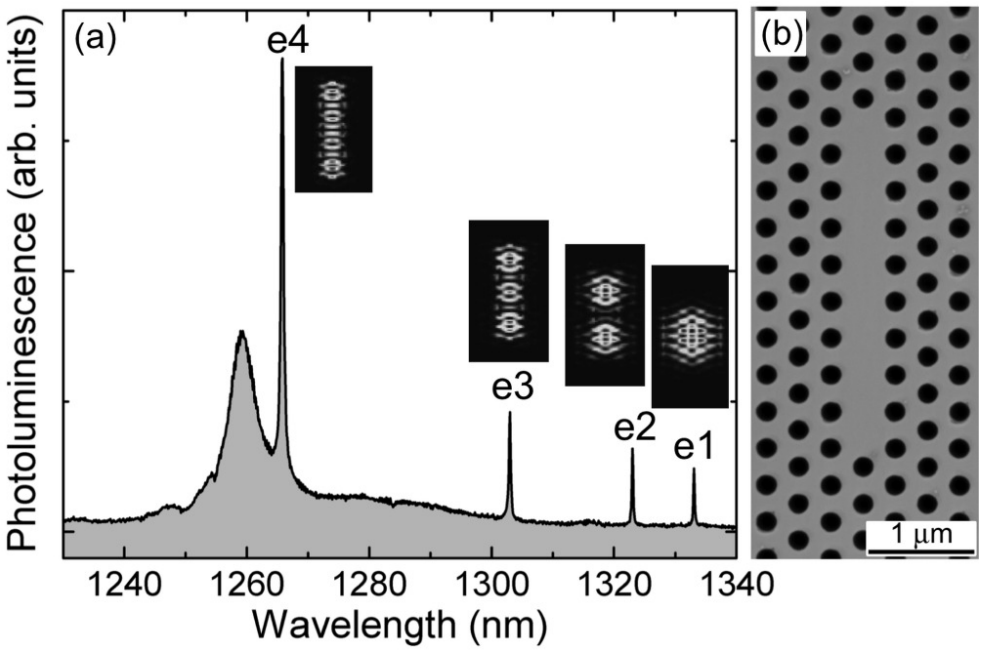

Figure 3.1: **L9–photonic crystal microcavity.** a) Measured spectrum showing the mode structure of a L9 photonic crystal microcavity (L9–PCM); insets show finite difference time domain (FDTD) simulations with the $|E|^2$ mode profile of the first 4–modes. b) Scanning electron microscopy (SEM) image of a L9–PCM designed for emission in the 1.3 μm telecom window.

Mode	Q	λ (nm)	V_{eff} $(\lambda/n_{\text{eff}})^3$	$Q/V[\times 10^5(\lambda/n_{\text{eff}})^{-3}]$
e1	440239	1291	1.43	3.078
e2	45486	1285	1.60	0.284
e3	8541	1269	1.42	0.060
e4	2038	1236	1.39	0.001

Table 3.1: **Optical properties of the L9–photonic crystal microcavity (L9–PCM) obtained by finite difference time domain (FDTD) simulations.** Calculated optical properties for the L9–PCM with $a = 350$ nm, $r = 0.28a$, and $d = 190$ nm. The e–label refers to the even symmetry of the modes.

1.3 μm.

3.3.4 Fabrication process

A fabrication procedure based on electron beam lithography (EBL) and plasma etching was developed to fabricate PCMs emitting in the 1.3 μm telecom window. The first step involves plasma enhanced chemical vapor deposition (PECVD) to grow a thin layer of SiO_x (85 nm) as a hard mask for the future transfer of the pattern onto the active GaAs slab. On top of that, a 360 nm thick layer of ZEP–520A resist is deposited by spin coating. A large homogeneity in the hole size of the PC pattern is necessary to obtain high–Q PCM modes.[40] The low electron beam voltage (30 kV maximum) in our LEO 1455 e–beam writer implies that the apparatus is operating near its resolution limit to define the required patterns. Consequently, the dose received by each circle is altered by the dose received by the surrounding holes. Nevertheless, by using a dose correction factor that considers the presence of other surrounding holes (proximity effect correction) we can achieve excellent results during e–beam exposure. The point exposure function f accounts for the alteration of the hole size depending on the presence of surrounding holes.[41, 42] A series of Monte Carlo simulations were performed to obtain the characteristics of the energy transferred to the resist, taking into account the multilayer on the substrate ($GaAs/Al_{0.70}Ga_{0.30}As/GaAs/SiO_x$/ZEP–520A). The resulting f function considers the backscattering, the forward scattering, the finite beam size and the beam voltage. In our case, the best fit corresponds to a double Gaussian plus exponential function, parameterized as follows:

$$f(r) = \frac{1}{\pi(1+\eta+\nu)}\left[\frac{1}{\alpha^2}\exp\left(-\frac{r^2}{\alpha^2}\right) + \frac{\eta}{\beta^2}\exp\left(-\frac{r^2}{\beta^2}\right) + \frac{\nu}{2\gamma^2}\exp\left(-\frac{r}{\gamma}\right)\right] \quad (3.1)$$

where r represents the distance to the incidence point of the exposing beam, α accounts for the forward scattering, β corresponds to the backscattering contribution, η represents the ratio of the backscattered exposure to the forward exposure. The third exponential term accounts for a correction in the mid–range r–values, where some limitations arise from the double Gaussian approach.[43] The optimum set of parameters that define $f(r)$ is: α = 14 nm, β = 1.375 m, γ = 655 nm, η = 0.3383, ν = 0.7553. After EBL, the patterns are defined on the resist by developing with a mixture containing N–amyl acetate, methyl isobutyl ketone (MIBK) and deionized water (DI). Figure 3.2a shows a cross section of a hole in

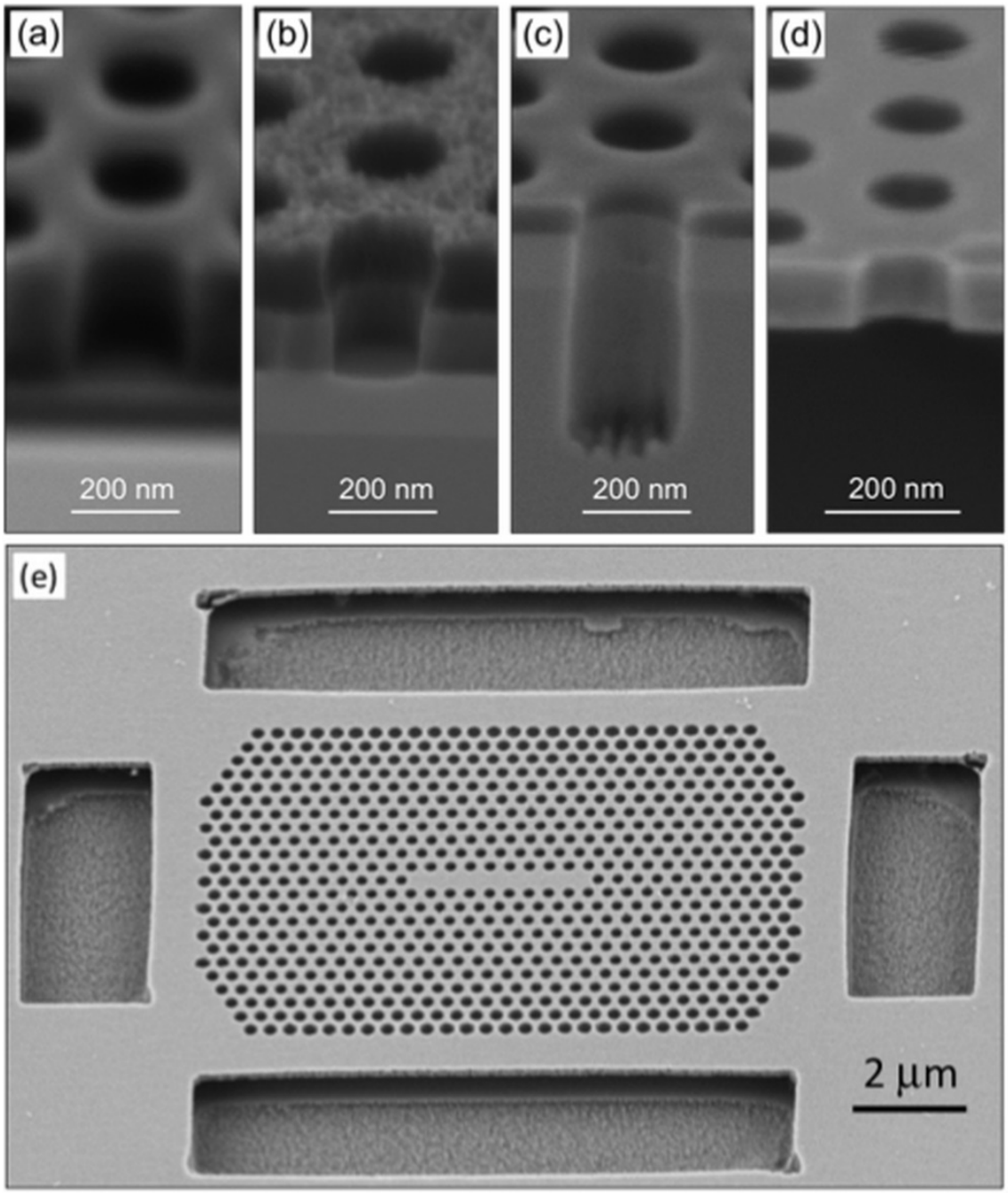

Figure 3.2: **Fabrication procedure for GaAs based L9–PCMs.** (a) Electron beam lithography (EBL) and developing of ZEP–520A positive resist, (b) Reactive ion beam etching (RIBE) based on CHF_3/N_2 to transfer the pattern to the SiO_x hard mask, (c) Inductively coupled plasma reactive ion etching (ICP–RIE) based on BCl_3/N_2 to transfer the pattern to the active GaAs slab, and (d) removal of the $Al_0.70Ga_0.30As$ sacrificial layer and remaining SiO_x layer with diluted HF to suspend the structures. (e) Tilted view of the final structure.

the obtained photonic crystal lattice. A post–bake (100 °C, 1 min) is required to increase the smoothness of the sidewalls of the holes, as well as the selectivity for the following plasma etching step. Reactive ion beam etching (RIBE) based on a CHF_3/N_2 gas mixture is used[43] to transfer the hole pattern to the SiO_x hard mask. Figure 3.2b shows a profile of the holes after this step. The etching produces smooth and vertical holes in the SiO_x hard mask.[44] Next, inductively coupled plasma–reactive ion etching (ICP–RIE) in an Oxford Plasmalab 80 equipment is performed. ICP power of 300 W and a BCl_3/N_2 gas mixture are used to transfer the hole pattern to the active GaAs slab. Further details of this plasma etching process are chamber pressure: 2.5 mTorr, ICP power: 300 W, RIE power: 20 W, wafer temperature: 30 °C, output DC Bias: 55 V. In a previous work, Atlasov et al., carried out an study on the benefits of such gas mixture focusing on the verticality of the hole profile by varying the N_2 flux content.[45] Our results reproduce and confirm the variation in the verticality and shape of the holes for the range of variation of N_2–flux content presented in that work. In our case we have focused on the fine optimization of the range of values for the BCl_3/N_2 flux in which the shape of the holes is vertical and the Q–factor of the fundamental mode of the L9–PCMs is maximized (Section 3.3.5). Also, we have found that it is important to deeply penetrate in the $Al_{0.70}Ga_{0.30}As$ sacrificial layer during the ICP–RIE etching in order to favor the sacrificial layer removal with HF:DI dilution avoiding the formation of AlF–based microcrystalline structures under the active GaAs slab (Section V) that may degrade the photonic performance (i.e. Q–factor). Figure 3.2c and Figure 3.2d show respectively the shape of the holes before and after the release of the photonic crystal membrane. We have etched four large holes surrounding the PCM (Figure 3.2e) to improve the flow of the HF–based dilution during the wet etching step.[46] The described method produces very smooth and highly vertical holes in the suspended GaAs active slab (Figure 3.2e shows a SEM image of an entire L9–PCM), resulting in improved optical performance, as it will be described in Section 3.3.5.

3.3.5 Optical characterization

In order to evaluate the optical properties of the fundamental mode of the L9–PCMs we have used optical micro–photoluminescence (μ–PL) at RT. The excitation source was a 785 nm continuous wave (CW) laser diode. An objective lens (0.5 NA) was used to focus a small excitation spot ($\sim$ 1.5 μm) centered on the

photonic crystal defect. The light emitted by the PCM is collected through the same objective and focused to an optical fiber that drives the signal to a 0.85 m focal length double spectrometer with a cooled InGaAs photodiode array detector. For each spectrum (for instance, see Figure 3.1a) the Q–factor of the fundamental mode of the L9–PCMs is given by the ratio of the wavelength over the linewidth at half maximum ($Q = \lambda/\Delta\lambda$). We have determined the optimum conditions of the ICP–RIE plasma etching through the analysis of a set of L9–PCMs in 4–different samples, each of them processed with the same parameters for the PECVD, EBL and RIBE steps. Figure 3.3a shows the variation in the Q–factor of the PCM modes with the relative N_2 flux content for a specific range (55–70%). We assume that any influence of the material properties on the Q–factor can be disregarded, since every PCM considered in Figure 3.3a is spectrally tuned at 1280 ± 5 nm. Specifically, in the 60–70% range of relative N_2 flux content, the overall shape and verticality of the holes is close to 90∘ although Q–factors can change from 11000 to 20000. From that analysis we concluded that the optimum partial N_2 flux content is 0.65 (BCl_3/N_2 flux content: 6.0/11.1 sccm). We have measured Q–factors up to 30000 in this series. SEM analysis suggests that the evolution in the Q–factors with the N_2–flux content is strongly related to an increase in roughness of the sidewalls due to small voids (insets Figure 3.3a) and a slight deviation in the verticality of the holes.

3.3.6 Flake formation during the wet etching

We have found a high production of debris under the active GaAs slab during the membrane release with a HF–based wet etching, which might affect dramatically the Q–factor. Figure 3.4 shows SEM images of the debris, which depending on the amount and size of the particles, might not be easily observed under the optical microscope (500×) and sometimes the effect is just noted by a very slight, inhomogeneous change in the color of the PCM membrane. When few particles (flakes) are present, only a careful optimization of the parameters during SEM inspection makes the flakes visible (Figure 3.4a) as slight shadows underneath the PCM membrane. Similar debris was observed either over[14] or underneath[32] the PCM structures. In particular, we have observed these flake–like structures especially underneath the slab (Figures 3.4a–c). Flakes can easily be observed if some openings surrounding the PCM are performed to suspend the structure in large membranes (Figure 3.4b). Close SEM inspection of the flakes (Figure

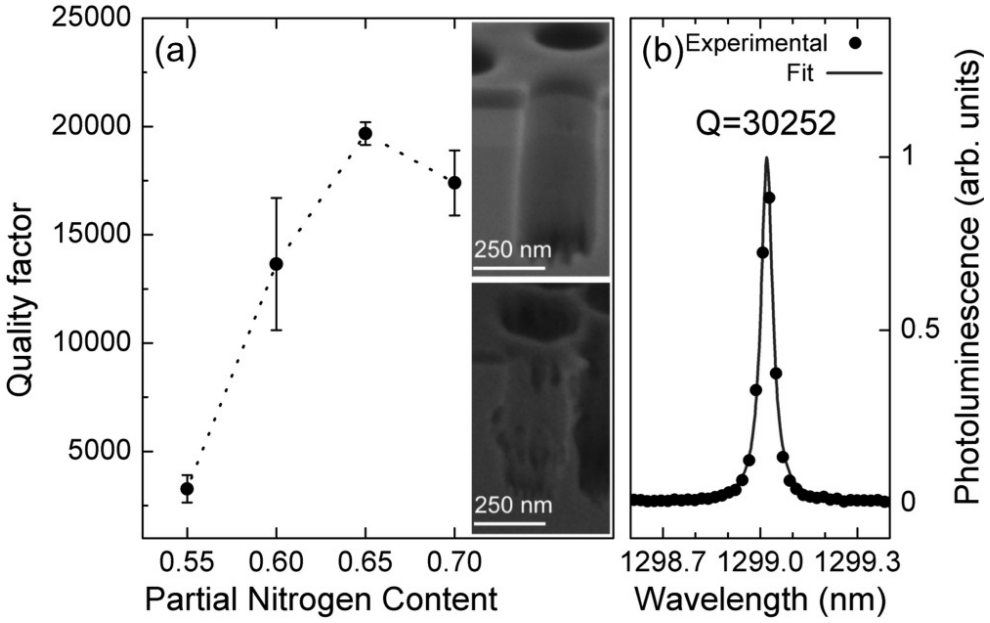

Figure 3.3: **Optimization of the quality factor.** (a) Impact of the partial N_2 flux content on the quality factor (Q) of the photonic crystal microcavity (PCM) fundamental mode in an L9. The error bars represent the range of the Q measured for series with identical fabrication parameters; insets with SEM images show the hole–cross section after the Inductively coupled plasma–reactive ion etching (ICP–RIE) etching for 0.55 (bottom) and 0.65 (top) N_2 partial flux content; the shape and roughness for the highest and lowest Q–factors obtained with N_2 flux content 0.65 (top) and 0.55 (bottom), respectively. The dashed line represents a guide to the eye. (b) Detail of the line shape for a measured high Q ($Q = 30000$) fundamental mode of an L9–PCM fabricated with the optimum partial N_2 flux content (0.65). The line represents the best Lorentzian fit corresponding to the experimental data.

3.4c) reveals their crystallographic faceting. The sizes of such particles range from few nanometers to several microns. We suspect they might affect the Q–factor of the PCMs if they are located in the proximities of the photonic crystal defect. We have determined the chemical composition of the flakes by energy dispersive X–ray analysis (EDAX). We have selected a single isolated flake (Figure 3.4d) and obtained the EDAX spectra inside (Figure 3.4e–top) and outside of the flake (Figure 3.4e–bottom). From the analysis we can conclude that the flakes contain Al, F and O, and the amount of F is around three times the amount of Al or O. A common chemical reaction involving Al in presence of water and HF is the formation of aluminum fluoride compounds, like AlF_3 or its trihydrite form ($AlF_3 3H_2O$, Rosenbergite) which results in crystals which are transparent and very resistant to chemicals and mechanical damage. Depending on the concentration of the HF dilution, we can control the formation of such crystals. Figure 3.5a presents a high density of flake structures resulting from a HF:DI 1:10 during 1 minute. Figure 3.5b shows a significant reduction on the flake formation due to a larger concentration of the HF:DI (1:3) for 20 seconds. We have practiced wet etching on different GaAs/AlGaAs wafers varying the HF concentration and the time duration of the etching. We therefore concluded that rapid wet etching with higher concentrations of HF:DI (1:3) during the membrane release might prevent the flake formation and may prevent any degradation of the high Q–factor.

3.3.7 Summary and conclusions

We have developed a fabrication procedure for the release of high–Q PCMs on GaAs with embedded InAsSb/GaAs QDs emitting in the 1.3 μm telecom window at RT. A thin layer (85 nm) of SiO_x is deposited by PECVD and serves as a hard mask for etching. After the coating of 360 nm of ZEP–520A resist, EBL and developing procedures define the holes on the resist. Two dry etching procedures (RIBE and ICP–RIE) are performed to define the pattern on the active slab. Optimum conditions for the partial N_2 flux content for the ICP–RIE process have been found to yield vertical and smooth sidewalls. The suspended membrane is released by removing the $Al_{0.70}Ga_{0.30}As$ sacrificial layer with diluted HF. A careful control of both the duration of the wet etching and the concentration of the hydrofluoric dilution is needed to prevent the formation of the flake structures. Q–factors up to 30000 are obtained. These results pave the way towards the study

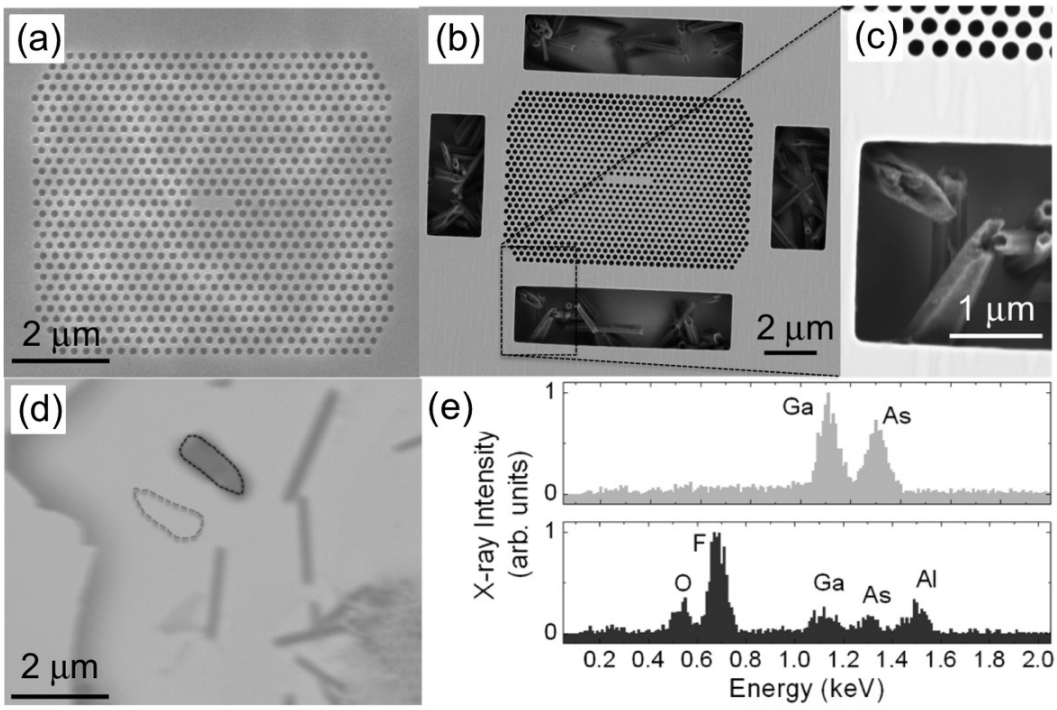

Figure 3.4: **Observation of flakes.** (a) under specific conditions, flakes can be observed through the membrane during scaning electron microscopy (SEM) inspection as shadowed areas, (b) flakes observed through the openings practiced around the photonic crystal microcavity (PCM) structure, (c) close–up of the flakes revealing the crystallographic morphology of the flakes, (d) opened area with low density of flakes to analyze their composition, and (e) Energy dispersive X–ray analysis (EDAX) corresponding to the regions indicated in (d) and showing the elements found in the material outside (top) and within (bottom) the flakes.

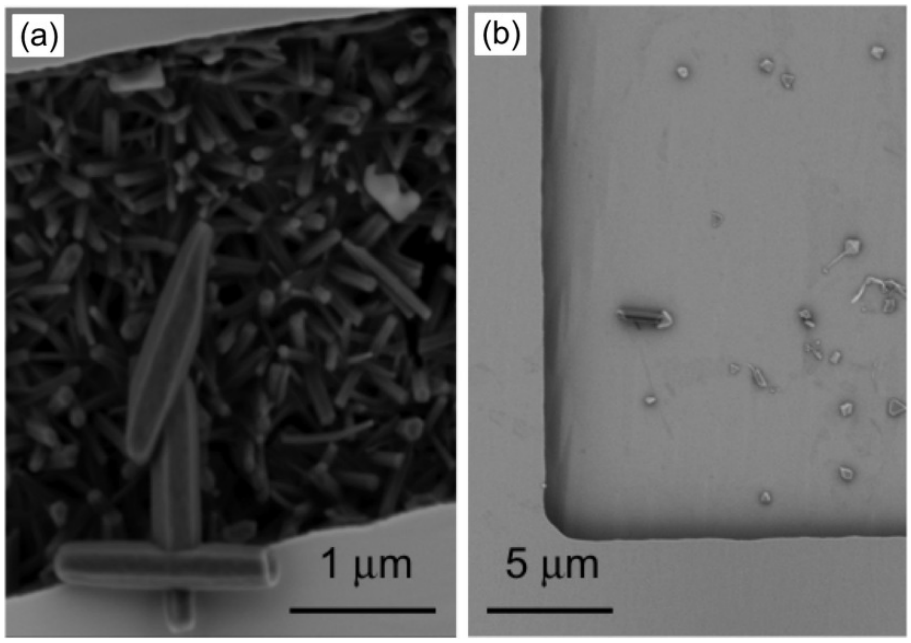

Figure 3.5: **Control of the density of flake residuals.** (a) 1:10 hydrofluoric dilution yielding slow lateral etch rate (1 μm/min) of the sacrificial layer and high density of residual flakes. (b) 1:3 hydrofluoric dilution yielding a rapid etch (12 μm/min) of the sacrificial layer that removes most of the flake residuals.

of the emission properties of the InAsSb QDs coupled to high–Q PCMs.

3.4 On–going work

We have developed a fabrication procedure of suspended photonic crystal microcavities in a GaAs–based material. That procedure was demonstrated in a GaAs–based epitaxial material embedding InAsSb–QDs. After the completion of this fabrication procedure, several on–going projects could be addressed. We have used the presented fabrication procedure to demonstrate RT lasing characteristics in our L9 & InAsSb–QDs at the 1.3 μm window. We have also performed that fabrication procedure with optimized parameters within the 980 nm window. It is worth noting that as soon as the lattice parameters (a and r) are reduced, the fabrication release is more difficult. With the evaluation of the *figure of merit* of the cavities for such smaller parameters, we gain insights in the limitations of the fabrication procedure.

Chapter 4

Near thresholdless laser operation at room temperature

I. Prieto,[1] L. E. Muñoz–Camúñez,[1] J. M. Llorens,[1] A. G. Taboada,[1,2] J. Canet–Ferrer,[3] J. M. Ripalda,[1] C. Robles,[1] G. Muñoz–Matutano,[3,4] J. P. Martínez–Pastor,[3] and P. A. Postigo[1]

Not published

[1]IMM–Instituto de Microelectrónica de Madrid (CNM–CSIC), Isaac Newton 8, PTM, Tres Cantos, Madrid E-28760, Spain

[2]Laboratory for Solid State Physics, ETH Zürich (ETHZ) HPF F2 Otto–Stern Weg 1 CH–8093 Zürich, Switzerland

[3]UMDO (Unidad asociada al CSIC), P.O. Box 22085, E–46071 Valencia, Spain

[4]Optics and Quantum Communications Group, ITEAM, UPV, Valencia, Spain

4.1 Context & motivation

One of the main applications of the photonic crystal microcavities with embedding quantum nanostructures is their capability to construct a very efficient lasing source. The ultimate laser, referred to as thresholdless laser, consists of a photonic cavity with light emitters that emit almost no spontaneous emission.[18] QDs are ideal light emitters to be introduced in those cavities.[47, 48] [49, 7, 28] Those works rely on the combination of the high–Q and low–V_{eff} presented by the appropiated photonic cavities and the low transparent carrier density and large carrier confinement exhibited by the QDs. The operation of those devices at room temperature and under continuous wave excitation [19] of those devices is necessary for future applications. In this work, we demonstrate the achievement of near thresholdless lasing operating at room temperature in the 1.3 μm telecom window. The system consists of a L9–photonic crystal microcavity with a single layer of InAsSb QDs. The dynamics of the laser was analyzed through the rate equation model.[50]

4.2 Contribution

My contributions to this work are the following:

- Design of the epitaxial material,
- Design of the L9–photonic crystal microcavity,
- Fabrication of the samples,
- Partial optical characterization of the devices,
- Calculation and analysis of the confinement factor (Γ),
- Analysis and writing of the results.

4.3 Publication

4.3.1 Abstract

The development of a thresholdless laser operating at room temperature is key for the future replacement of electronics with photonic integrated circuits, en-

abling an increase of several orders of magnitude in computing speeds.[51, 18] Khajavikhan et al. recently demonstrated thresholdless lasing characteristics at low temperature (4 K).[52] However, for practical applications, room temperature laser emission becomes necessary. Here we report a laser based on InAsSb quantum dots [37] embedded in a photonic crystal microcavity, which exhibits ultra–low power threshold (860 nW) and high efficiency ($\beta = 0.85$) thus operating in the near thresholdless regime at room temperature in the 1.3 μm spectral window. The results open up a wide range of opportunities for room temperature applications of ultra–low threshold lasers, such as integrated photonic circuitry or high sensitivity biosensors.

4.3.2 Introduction

The early demonstration of lasing emission in a photonic crystal microcavity (PCM)[53] opened new avenues towards very low threshold and highly efficient solid state lasers by taking advantage of two aspects: on one hand, PCMs allow a strong confinement of the light, through high quality factors (Q) and small mode volumes (V_{eff}). On the other hand, zero–dimensional nanostructures or quantum dots (QDs) were proposed as an optimal active region to reach low threshold and highly efficient laser sources.[47, 48] Even though it has been argued that a truly thresholdless laser is not possible in practice,[54] the term thresholdless is used in the literature[18] to identify lasers presenting two main features: a spontaneous emission coupling factor (β) close to 1 and low non radiative losses. Non radiative losses are reduced by several orders of magnitude at cryogenic temperatures, although they can never be completely suppressed. Therefore, a lasing threshold remains measurable in so called thresholdless lasers. An ultimate thresholdless laser[55, 56, 18] operating at room temperature (RT) will have a strong impact in optical communications[57] in the near infrared as well as, for instance, in bio–organic sensing, where the 1.3 μm spectral window has been used for single–cell photonic nanocavity probes.[58] Ultra–low threshold lasing was achieved using an ever–decreasing number of QDs within photonic crystal cavities.[49, 7, 19, 32, 59, 28] That strategy was adopted by Strauf et al.[7] to demonstrate near thresholdless lasing at low temperature (4.5 K) using few QDs (2–4) as active emitters. The authors reported power threshold values as low as 124 nW (corresponding to an absorbed power of 4 nW) and a high $\beta = 0.85$. Khajavikhan et al. have recently demonstrated thresholdless lasing at low

temperature (4 K).[52] The authors also reported RT lasing, although without thresholdless characteristics. In this work we report a RT continuous wave (c.w.) laser with emission characteristics close to those of an ideal thresholdless laser.

4.3.3 Design and fabrication of the L9 photonic crystal microcavity

Our L9–PCM laser was fabricated in GaAs/AlGaAs epitaxial material with a single layer of InAsSb QDs emitting in the 1.3 μm telecommunications spectral window at RT.

Design

We have designed a PCM that consist of a hexagonal lattice of air holes with 9–missing holes along the ΓK direction (i.e., L9–PCM) fabricated on a GaAs suspended slab.[60] For that PCM, the best Q/V_{eff} ratio is obtained for the fundamental mode. Therefore, the design of the L9–PCM was optimized to achieve spectral matching of the fundamental mode with the emission of the QDs. Figure 4.1a shows the mode profile of the L9–PCM fundamental mode, calculated by the finite difference time domain (FDTD) method (see Supplementary information). The calculated values for Q and V_{eff} are 4.4×10^5 and $1.43\times(\lambda/n_{\text{eff}})^3$ respectively, where λ represents the spectral position and n_{eff} is the effective refractive index of the fundamental mode.

Fabrication

The fabrication of the L9–PCM involved a BCl_3/N_2 based plasma etching procedure, optimized for the enhancement of the Q of the fundamental mode.[16] Figure 4.1b shows a scanning electron microscope image of the resulting L9–PCM. Further information of the fabrication procedure can be found in Methods.

Epitaxial material

The spectrum of the QD ensemble shows the fundamental transition that corresponds to the excitonic emission centered at 1280 nm with an inhomogeneous broadening of 23 meV. The incorporation of Sb in the InAs QDs induces an upward shift of the conduction and valence band edges; it results in a deeper hole

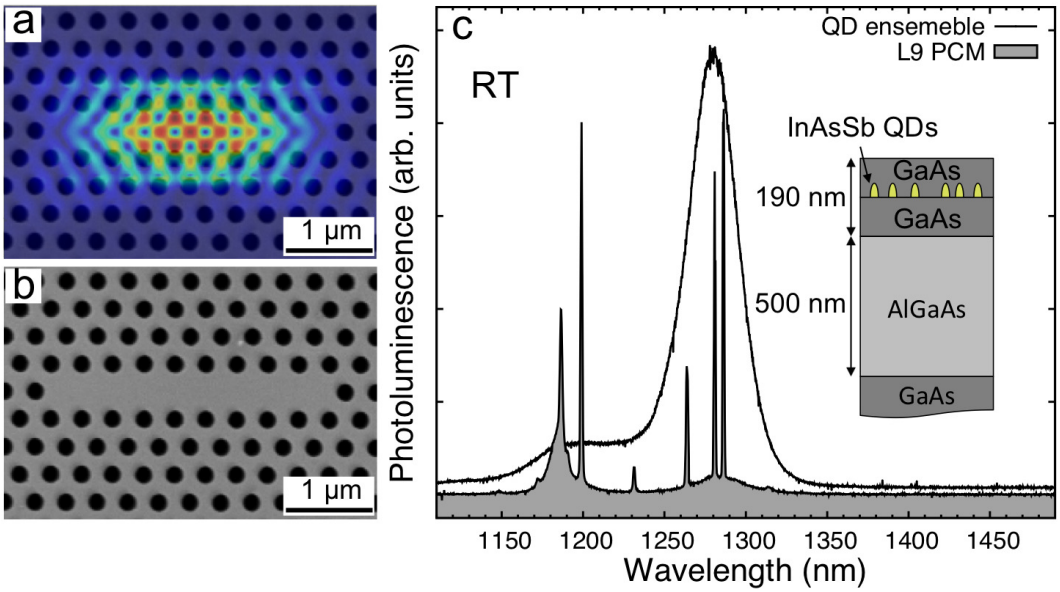

Figure 4.1: **Design, fabrication and optical characterization of the epitaxial material and the L9 photonic crystal microcavity (PCM) at room temperature. (a)** Calculation of the electric field distribution $|E|^2$ of the L9–PCM fundamental mode. **(b)** Scanning electron microscopy image of a L9–PCM. **(c)** Photoluminescence (PL) of the ensemble of the quantum dots (QDs) outside of the PCM (black line) and PL of a L9–PCM (filled grey) showing the mode structure. The inset presents a schematic diagram of the epitaxial material.

confinement and more efficient emission at RT,[61, 36, 37, 38, 62] thus overcoming the thermal ambipolar escape of carriers that reduces the RT efficiency of conventional InAs QDs.[63, 64] The observed resonances from the PL spectrum of the L9–PCM correspond to the cavity mode structure, with the fundamental mode emitting at 1286 nm.

4.3.4 Optical characterization

Figure 4.2a presents the integrated intensity of light emitted by the fundamental mode of the L9–PCM laser as a function of c.w. optical pump power (i.e., L_{in} vs. L_{out} or LL–curve) at RT. We have estimated an effective power lasing threshold of 860 nW (see Supplementary information). To determine β we used a coupled rate equation model where $\beta = 0.85$ optimizes the fit to the experimental data (see Supplementary information). Figure 4.2a also shows the calculated LL–curves for different β–values (grey curves), including the fit for $\beta = 0.85$ (red curve). This value is comparable to those reported in state–of–the–art lasers designed for

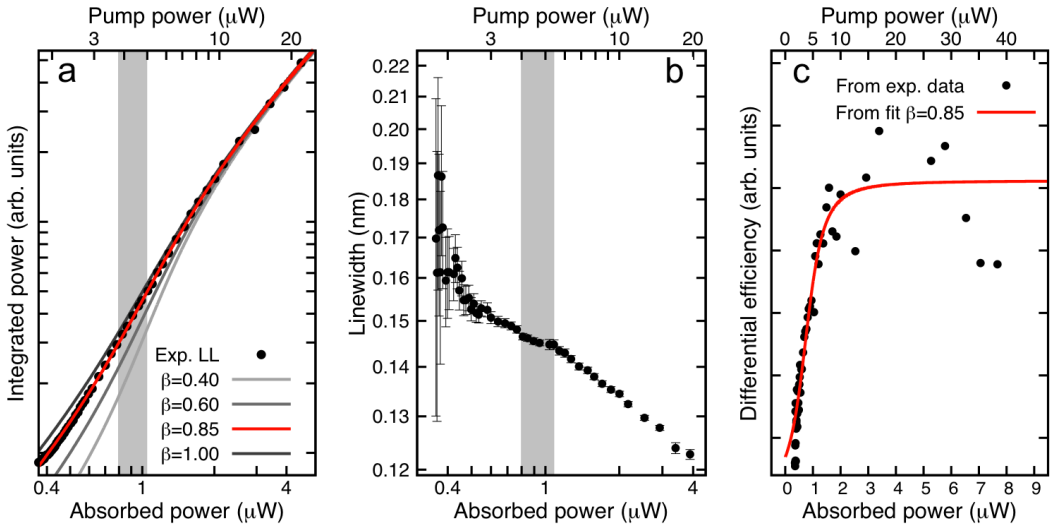

Figure 4.2: **Output characteristics of the L9 photonic crystal microcavity (PCM) laser at room temperature. (a)** Light in vs. Light out (LL–curve) characteristics of the L9–PCM laser for different β–values (grey lines) in logarithmic scale; the best fit (red line) is for $\beta = 0.85$. **(b)** Evolution of the linewidth of the L9–PCM resonant mode with the excitation power. **(c)** Analysis of the differential efficiency calculated from the LL data (dots) and from the fit for $\beta = 0.85$ (line). Error bars in **(b)** are referred to the statistical deviation analysis. Grey region in **(a-b)** marks the amplified spontaneous emission (ASE) region.

their operation at temperatures few degrees above absolute zero.[52, 7]

4.3.5 Linewidth

The assertion that the device indeed reaches lasing is further substantiated by the linewidth dependence on pump power (Figure 4.2b). Three regions corresponding to different emission regimes are identified[52] from the linewidth behavior: the photoluminescence (PL) region, below threshold, where the light is predominantly spontaneously emitted;[65] the lasing region, above threshold, where light is mostly influenced by the stimulated emission; and the amplified spontaneous emission (ASE) region around the threshold (grey region in Figure 4.2a) as a transition between both regimes. In the ASE region, a small plateau in the evolution of the linewidth ($\Delta\lambda$) with the power is observed [7, 19, 21, 52] whereas a linewidth–narrowing behavior can be measured both within the PL and the lasing regions.[52] Such behavior is observed in our device at RT. The Q–factor, given by $\lambda/\Delta\lambda$ at the lowest excitation power ($P_{\text{exc}} = 370$ nW) is $Q = 7400$.[65] As the

excitation power increases, the optical mode becomes narrower due to gain mechanisms in lasing systems.[66] At high excitation power above threshold ($P_{\text{exc}} = 10.14\ \mu\text{W}$), $\lambda/\Delta\lambda = 12100$ (see Supplementary information). The evolution of the linewidth of the fundamental mode with the excitation power at RT follows a similar trend as that observed in near–thresholdless lasers at 4.5 K.[7, 18]

4.3.6 Differential efficiency

Finally, an important feature of a laser system is the differential efficiency (DE) given by the derivative $dL_{\text{out}}/dL_{\text{in}}$.[21] For a lasing device the DE increases with the power tending to a constant value. The DE at RT is represented in Figure 4.2c (dots) with the calculated DE curve (line) for $\beta = 0.85$. The calculated DE follows the experimental data and deviates at excitation powers well above the threshold. This effect is due to the saturation of the QDs, which was not considered in the model.

4.3.7 Summary and conclusions

In summary, continuous wave and near thresholdless laser operation in the 1.3 μm telecom window at room temperature was demonstrated for a system combining a single layer of InAsSb QDs with a photonic crystal microcavity. We showed that thermally activated processes, such as non radiative recombination, are not an insurmountable obstacle to the realization of laser sources with characteristics similar to those observed in near thresholdless lasers at temperatures few degrees above absolute zero. Such highly–efficient systems are very promising candidates for applications in optical integrated circuits, potentially enabling low consumption electrically–injected devices based on PCMs [67] at RT.

4.4 Methods

4.4.1 Fabrication

The epitaxial material was grown by solid–source molecular beam epitaxy (MBE) on a semi–insulating GaAs substrate. The inset in Figure 4.1c shows the epitaxial structure of the wafer which consisted of the active region embedded in a 190 nm thick GaAs layer and a 1 μm thick $Al_{0.75}Ga_{0.25}As$ sacrificial layer underneath.

The active region includes a single layer of InAsSb QDs with luminescence at 1.3 μm. The microcavities were patterned by electron beam lithography on a 365 nm thick ZEP–520A resist homogeneously spun onto a 90 nm thick SiO_x hard mask deposited by plasma enhanced vapor deposition (PECVD). Reactive ion beam etching (RIBE) was performed to drill the SiO_x layer previously deposited on the epitaxial material and inductively coupled plasma–reactive ion etching (ICP–RIE) was used to transfer the pattern to the active GaAs slab. The final step consisted of the removal of the sacrificial layer underneath the L9–PCMs by means of HF:H_2O wet etching. Four large rectangular holes surronding every structure were fabricated to facilitate the renewal of the HF solution and the removal of the remaining material underneath every structure during the wet etching.[16]

4.4.2 Optical characterization

A 785–nm laser diode (LD) operating in continuous wave mode was used for the optical pumping of the photonic structures. The excitation beam was focused down to a 1.5 μm diameter spot by means of a microscope objective (20×, $NA = 0.4$). The same objective was used to direct the light emitted from the sample to a 0.85 m length double spectrometer through an optical fiber. An InGaAs cooled photodiode array was used as a detector.

4.4.3 Appendix A: Design of the L9 photonic crystal microcavity

There are several types of PCMs that present high Q/V_{eff} ratio, although they often require an accurate positioning and a size tuning of specific holes within the lattice [S1–S8] which also makes them very sensitive to fabrication imperfections. The use of elongated line–defect PCMs of the type L_n, where n stands for the number of holes suppressed to create the defect, has been shown to provide a good compromise for the Q/V_{eff} ratio.[60] We have designed L9–PCMs with lattice constant $a = 350$ nm, slab thickness $d = 190$ nm and 11 rows of neighbouring holes ($N = 11$). We have carried out simulations by the finite difference time domain (FDTD) method [39] that have allowed us to evaluate the quality factor (Q), the spectral position (λ), the effective volume (V_{eff}) and the effective refractive index (n_{eff}) of the fundamental mode of the L9–PCM. Further details on the

simulation of similar structures can be found elsewhere.[68] Figure 4.3 shows the results of the simulations varying the size of the holes of the PCM from $r/a = 0.20$ to 0.38 in steps of 0.01. The PCMs present an increasing Q as r/a increases, with a maximum Q for $r/a = 0.35$; for higher r/a–values the performance of the cavity is dramatically degraded and at $r/a = 0.38$ the Q–value is only several hundreds (Figure 4.3a). Figure 4.3b and 4.3c show the variation with r/a of the spectral position of the fundamental mode (λ) and the effective mode volume (V_{eff}), respectively. V_{eff} is related to the degree of confinement of the photonic mode and is defined as:[69]

$$V_{\text{eff}} = \frac{\int_{V_{\text{total}}} \varepsilon E^2 \mathrm{d}^3\mathrm{r}}{\max(\varepsilon E^2)} \tag{4.1}$$

where ε and E^2 are the permittivity of the material and the electric field intensity of the mode, respectively, over the entire simulation window (V_{total}). As Q increases V_{eff} decreases and both drastically decrease for $r/a > 0.35$. At very high r/a–values, the mode is not confined anymore, i. e. V_{eff} increases, which corresponds to a strong decrease in Q. The effective refractive index (n_{eff}) or, alternatively, the effective permittivity (ε_{eff}) of the mode are defined as:[70]

$$\varepsilon_{\text{eff}} = n_{\text{eff}}^2 = \frac{\int_{V_{total}} n^2 E^2 \mathrm{d}^3\mathrm{r}}{\int_{V_{\text{total}}} E^2 \mathrm{d}^3\mathrm{r}} \tag{4.2}$$

Figure 4.3d shows the variation of n_{eff} with r/a: n_{eff} is relatively constant ($n_{\text{eff}} \simeq 2.75$) for a wide range of r/a–values, although it decreases strongly for $r/a > 0.35$. This is an evidence of the smaller confinement within the microcavity for very high r/a values, which dramatically degrades Q. Our calculations did not consider the influence of both the imperfections introduced during fabrication and the absorption losses of the active region, which produce the main deviations from experimental measurements. We have experimentally determined that the highest Q–factors are obtained for the devices with r/a between 0.26 and 0.31 (not shown). For the device presented in the manuscript, the calculated parameters are: $r/a = 0.30$, $Q = 440200$, $\lambda = 1290.6$ nm, $V_{\text{eff}} = 1.43\ (\lambda/n_{\text{eff}})^3$ and $n_{\text{eff}} = 2.78$.

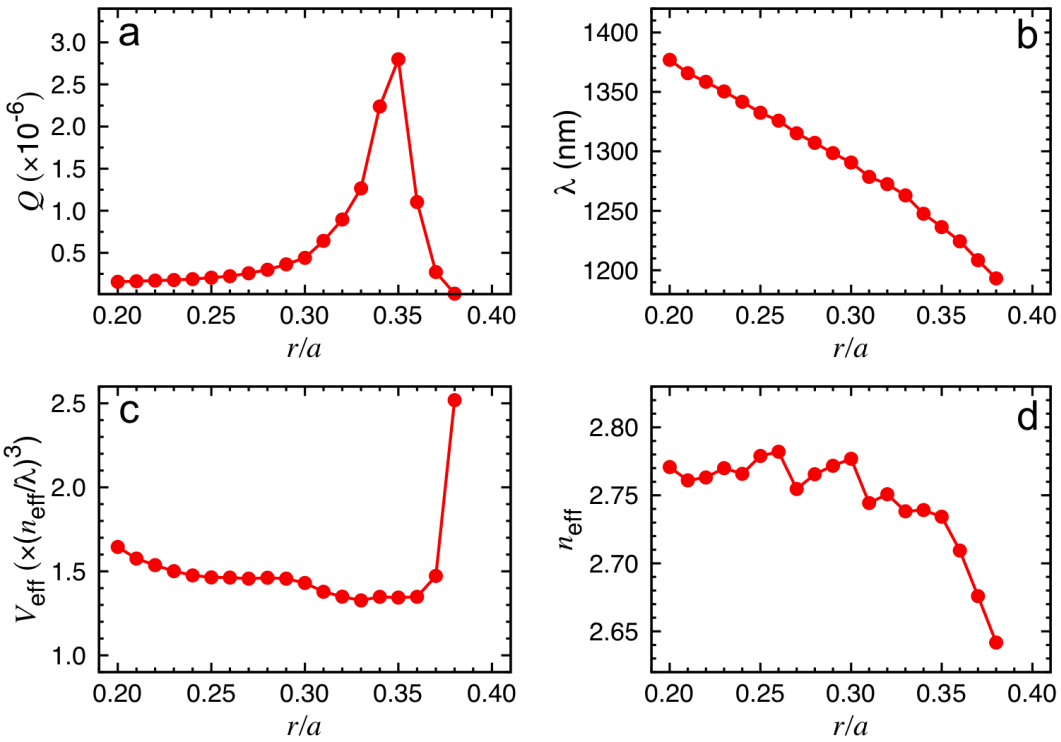

Figure 4.3: **Calculation of the optical parameters of the L9 photonic crystal microcavity.** **(a)** Quality factor (Q). **(b)** Spectral position (λ). **(c)** Effective volume (V_{eff}). **(d)** Effective refractive index (n_{eff}). The calculation has been made for the fundamental mode with pitch and slab thickness $a = 350$ nm and $d = 190$ nm, respectively.

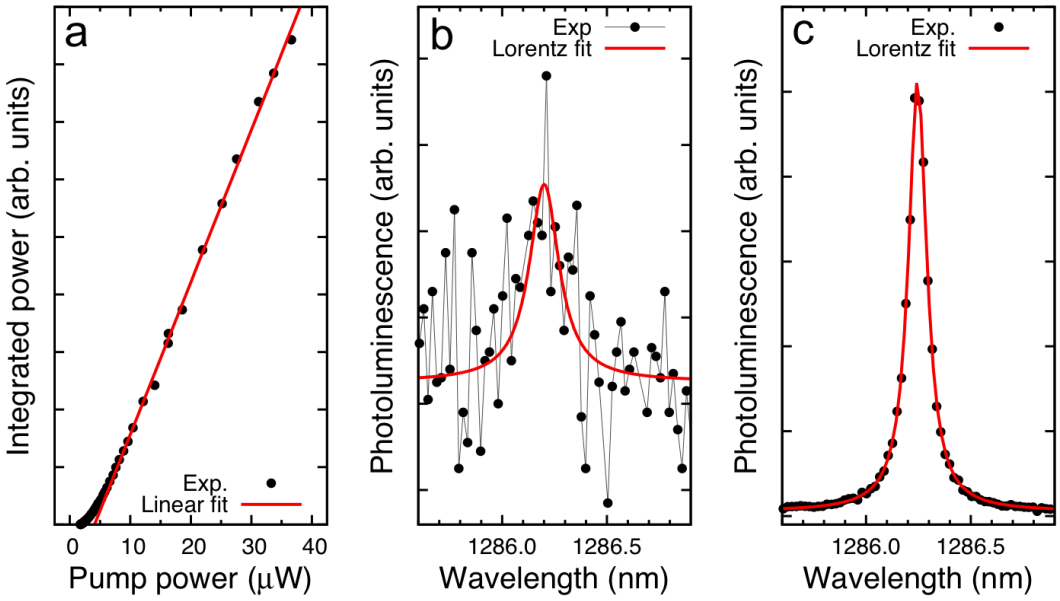

Figure 4.4: **Optical properties of the L9 photonic crystal microcavity laser at room temperature. (a)** Light in – light out curve of the laser (black dots). The red line shows the linear fit used to obtain an estimated total power threshold $P_{\text{th}} = 4.1 \pm 0.2\ \mu W$. **(b)** Photoluminescence (PL) of the fundamental cavity mode (FM) measured (black dots) at the lowest excitation power $P_{\text{exc}} =$ 370 nW. The best lorentzian fit (red line) provides $Q = 7400$. **(c)** PL of the FM measured (black dots) at high excitation power $P_{\text{exc}} = 10.14\ \mu$W. The best lorentzian fit (red line) provides $\lambda/\Delta\lambda = 12100$.

4.4.4 Appendix B: Power threshold

Figure 4.4a shows the integrated power emitted by the fundamental mode versus the excitation power (LL–curve) at room temperature (RT). The curve presents a rather smooth transition within the ASE region which is typical from high–β lasers.[66] We have performed a linear fit of the LL–curve for high excitation powers. A threshold of $P_{\text{th}} = 4.1 \pm 0.2\ \mu W$ is obtained by extrapolation of the red line to zero output.[71, 7] That value corresponds to the total irradiated power. The estimation of the actual excitation power absorbed by the slab is obtained by considering the reflectivity of the GaAs surface (∼33%), the slab thickness (190 nm) and the absorption coefficient of GaAs for the excitation wavelength of 785 nm (10^4 cm^{-1}). Therefore, the absorbed pump power is a ∼21% of the total incident power [72] and the effective threshold pump power is 860 nW. Figure 4.4b shows the spectrum of the fundamental mode at the lowest excitation ($P_{\text{exc}} =$ 370 nW) with a $Q = 7400$. We should notice that Q is referred to empty cavities,

where no material gain or loss mechanisms are considered. For a lasing system, the stimulated emission affects the linewidth and the term Q is thus no longer valid. In general, a fraction of stimulated emission is always expected at powers well below threshold.[65] Therefore, we have considered Q of the fundamental mode as that measured at the lowest excitation power, and we have used $\lambda/\Delta\lambda$ as an effective Q altered by gain and loss mechanisms. For $P_{\mathrm{exc}} = 10.14\ \mu$W, well above the threshold, an intense emission from the mode is observed with $\lambda/\Delta\lambda = 12100$.

4.4.5 Appendix C: Rate equation analysis

We have fitted the LL–curve to a rate equations model:[50]

$$\frac{\mathrm{dN}}{\mathrm{dt}} = R_{\mathrm{p}} - \frac{N}{\tau_{\mathrm{r}}} - \frac{N}{\tau_{\mathrm{nr}}} - g\frac{c}{n_{\mathrm{eff}}}\left(N - N_{\mathrm{tr}}\right)P \tag{4.3}$$

$$\frac{\mathrm{dP}}{\mathrm{dt}} = \Gamma g\frac{c}{n_{\mathrm{eff}}}\left(N - N_{\mathrm{tr}}\right)P + \Gamma\beta\frac{N}{\tau_{\mathrm{r}}} - \frac{P}{\tau_{\mathrm{c}}} \tag{4.4}$$

where N and P are the carrier and photon densities within the microcavity, R_{p} is the pumping rate, g is the differential gain coefficient and N_{tr} is the transparency carrier density. A cavity photon lifetime $\tau_{\mathrm{c}} = 6.14$ ps is obtained from the linewidth of the mode below the threshold. The confinement factor $\Gamma = 0.0018$ accounts for the overlap between the PCM mode with the QDs (see Appendix C1). The radiative and non radiative recombination lifetimes are $\tau_{\mathrm{r}} = 1.20$ ns and $\tau_{\mathrm{nr}} = 0.24$ ns, respectively (see Appendix C2). The Purcell effect [S19–S21] is not expected to modify the effective radiative recombination rate in our sytem, mainly due to the large linewidth broadening of the emitters at RT.[73] Therefore we have excluded this effect from our rate equations model. We have used β, g and N_{tr} as fitting parameters and obtained $\beta = 0.85$, $g = 1.495{\times}10^{-11}$ cm^2 and $N_{\mathrm{tr}} = 1.0{\times}10^{14}$ cm^{-3}. Using those values we can estimate the pumping threshold:[50]

$$R_{\mathrm{p,th}} = \left(1 - \beta\right)\frac{N_{\mathrm{th}}}{\tau_{\mathrm{r}}} + \frac{N_{\mathrm{th}}}{\tau_{\mathrm{nr}}} \tag{4.5}$$

$$N_{\mathrm{th}} = \frac{1}{\tau_{\mathrm{c}}\Gamma\frac{c}{n_{\mathrm{eff}}}g} + N_{\mathrm{tr}} \tag{4.6}$$

where $R_{\mathrm{p,th}}$ and N_{th} are the pumping rate and the carrier density, respectively, evaluated at threshold in the steady state. We have obtained $R_{\mathrm{p,th}} = 884.1$ nW and $N_{\mathrm{th}} = 11.1{\times}10^{14}$ cm^{-3}, which are consistent with the values extracted from the linear fitting to experimental data.

4.4.6 Appendix D: Confinement factor Γ

The confinement factor (Γ) accounts for the matching between the active region and the optical mode. The conventional definition of Γ assumes that the entire active region is spectrally matched to the optical mode.[50] Nevertheless, that statement is no longer valid when the active region consists of a set of QDs, because the inhomogeneous broadening of the QDs is much larger than the linewidth of the cavity mode. Therefore, we have defined Γ as:

$$\Gamma = \xi \Gamma_{\mathrm{spatial}} \tag{4.7}$$

where ξ is the spectral matching factor and $\Gamma_{\mathrm{spatial}}$ is given by:[50]

$$\Gamma_{\mathrm{spatial}} = \frac{\int_{\mathrm{active}} n_{\mathrm{a}}^2 E^2 \mathrm{d}^3\mathrm{r}}{\int_{\mathrm{cavity}} n^2 E^2 \mathrm{d}^3\mathrm{r}} \tag{4.8}$$

where E^2 is the electric field intensity of the cavity mode and n_{a} and n are the refractive indexes of the active region and the host material, respectively.

Spectral matching: ξ

To determine ξ it is necessary a comparative analysis of the emission properties of the ensemble of QDs with respect to the cavity mode. The analysis (not shown) of the PL spectrum of the QD ensemble at RT reveals the presence of a family of QDs centered in 1280 nm with an inhomogeneous linewidth of 23 meV.[36] Considering a homogeneous broadening of the QDs at RT of 10 meV [74] only those QDs within a spectral window of 10 meV around the fundamental mode are expected to be spectrally matched to the cavity mode. The analysis, similar to that of Ref. [19] shows that 60% of the QDs are spectrally matched to the mode at RT, i. e., $\xi = 0.6$.

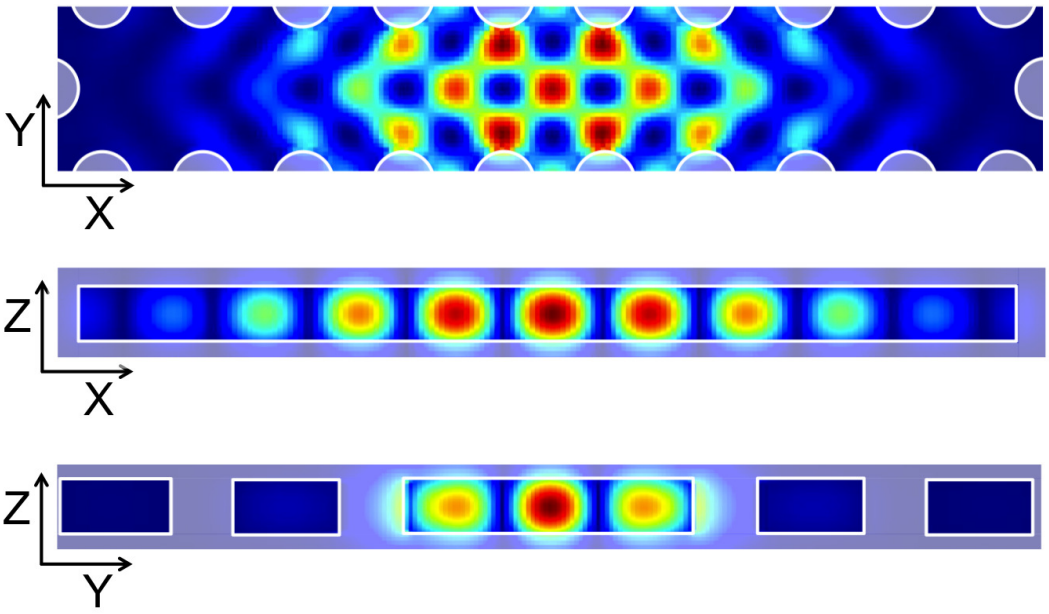

Figure 4.5: **Spatial distribution of the electric field ($|E|^2$) of the fundamental mode of the L9 photonic crystal microcavity. (top)** Planar view (XY) in the mid–slab. **(middle)** XZ cross section through the center of the cavity. **(bottom)** YZ cross section through the center of the cavity. The calculation has been made for pitch, radius and slab thickness $a = 350$ nm, $r = 105$ nm and $d = 190$ nm, respectively.

Spatial matching: Γ_{spatial}

To evaluate Γ_{spatial} we performed FDTD simulations varying the total number of QDs within the cavity defect (N) in random positions. The spatial distribution of the L9–fundamental mode profile is presented in Figure 4.5. We assumed that every QD is independent on the others and that the final value results from the sum of each of the individual contributions of the QDs. We modeled each QD as a 3D box with the same size than a single FDTD cell in X and Y axes and twice the size of the FDTD cell in Z axis. The dimensions in X, Y and Z axes are $L_{\text{QD,x}} = 17.5$ nm, $L_{\text{QD,y}} = 15.1$ nm, and $L_{\text{QD,z}} = 9.5$ nm. Those dimensions agree well with experimental and theoretical estimations.[37] We used a statistical analysis to evaluate the impact of the random character of the positions of the QDs on Γ. One thousand random configurations for the QD positions were realized for each of the systems containing $N = 1$, 3, 5, 10, 100, 200, 300 or 1000 QDs within the defect. The value of E^2 was evaluated in the position of every QD.

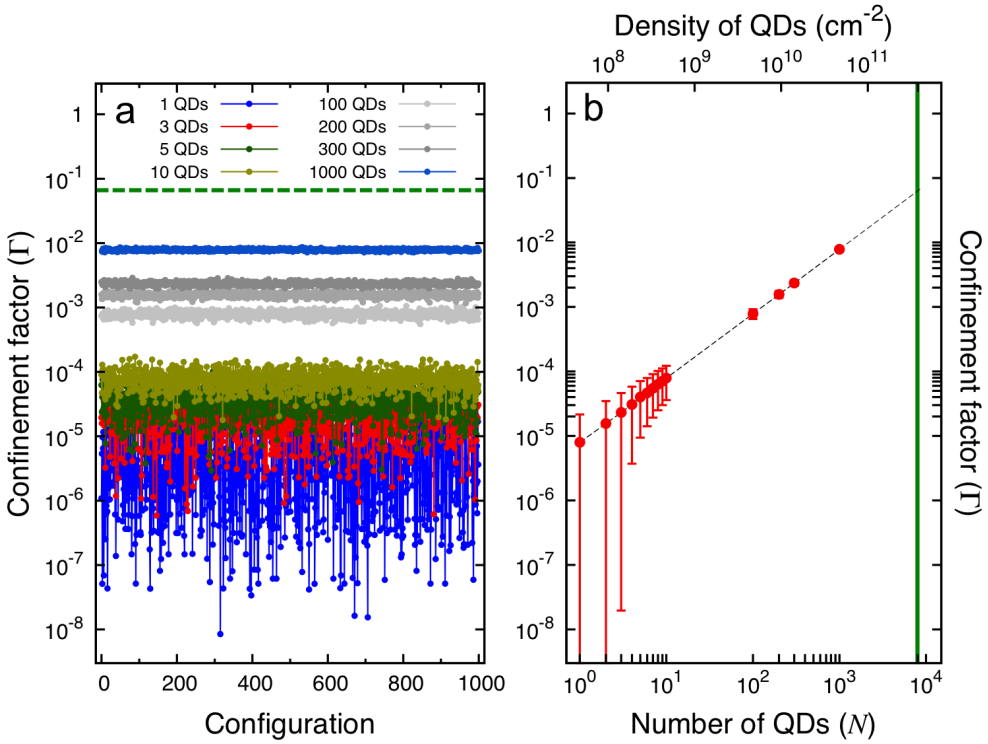

Figure 4.6: **Determination of the confinement factor for the fundamental mode of the L9 photonic crystal microcavity with self–assembled QDs.** **(a)** Value of Γ for different configurations with N QDs (N = 1, 3, 5, 10, 100, 200, 300, 1000) in random positions. The green dashed line sets the maximum value of Γ (Γ_{max} = 0.07). **(b)** Statistical analysis of Γ from data in **(a)**. The dashed line is shown for guidance purposes. The green line sets the maximum number of QDs that the cavity defect can host ($N_{max} \simeq 8000$). The calculation has been made for L9–PCMs with pitch, radius and slab thickness a = 350 nm, r = 105 nm and d = 190 nm, respectively. Error bars account for the statistical deviation of the data.

The resulting confinement factor: Γ

The value of Γ was calculated from Equation 4.7. Since more than 70% of the cavity mode is localized within the cavity defect, we have restricted the calculation to the cavity defect. Figure 4.6a shows Γ for each of the 1000 random configurations. Each configuration has N QDs inside the cavity defect. The large dispersion of the results for configurations with a small amount of QDs (aprox. $N < 100$) is attributed to the strong role of the position of the QDs with respect to the mode profile distribution. As the number of QDs increases, Γ is less sensitive to the random distribution of the QDs. The maximum value of Γ (Γ = 1) is achieved when every spatial position where the mode profile is non–zero is occupied by a

QD that is also spectrally tuned to the mode. That is expected to occur when the amount of QDs in a single layer within the defect is as large as $\sim 10^5$, i.e., the averaged QD density on the wafer is $\sim 10^{13}$ cm^{-2}. Neverthless the cavity defect can only host a maximum number of QDs $N_{\max} \simeq 8000$ which corresponds to a QD density of 3.8×10^7 cm^{-2}. Therefore the maximum value of the confinement factor is $\Gamma_{\max} = 0.07$. On the other side, Γ equals 0 when the active region is either spatially located in the nodes and/or is not spectrally tuned to the mode. In particular, for the determination of Γ in our case, it is necessary to evaluate the number of QDs lying within the defect. We have performed transmission electron microscopy (TEM) and atomic force microscopy (AFM) analysis (not shown) to determine an averaged density of QDs of 10^{10} cm^{-2}.[16] Therefore, we have estimated the total number of QDs lying within the cavity defect to be approximately 210 QDs and $\Gamma = 0.0018 \pm 0.0002$.

4.4.7 Appendix E: Radiative ($\tau_{\rm r}$) and non radiative ($\tau_{\rm nr}$) lifetimes

We have determined the radiative ($\tau_{\rm r}$) and the non radiative ($\tau_{\rm nr}$) lifetimes from time resolved photoluminescence (TRPL) experiments (Figure 4.7) outside of the cavities for a wide range of temperatures from 10 K to RT. Whereas at low temperatures the total decay time (τ) can be related to radiative processes, as the system reaches high temperatures the dynamics is rather governed by the non radiative mechanisms. At temperatures below 180 K, the τ–values are within 1.20–1.6 ns and at T close to RT $\tau = 0.2$ ns. Assuming that $\tau_{\rm r}$ does not present strong variations with T and

$$\frac{1}{\tau} = \frac{1}{\tau_{\rm r}} + \frac{1}{\tau_{\rm nr}} \tag{4.9}$$

we have obtained $\tau_{\rm nr} = 0.24$ ns using $\tau_{\rm r} = 1.20$ ns.

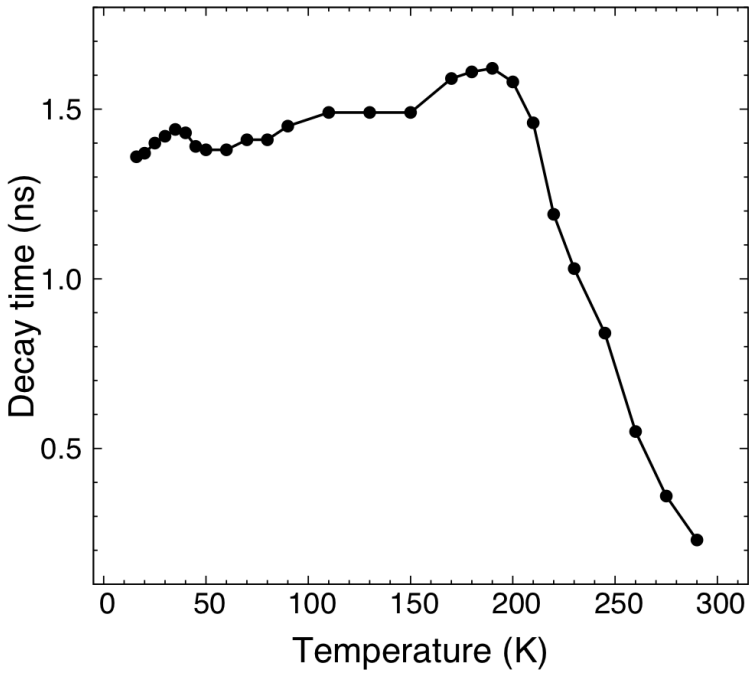

Figure 4.7: **Determination of the radiative and non radiative lifetimes from the total decay time.** The plot shows the total decay time (τ) measured by time–resolved photoluminescence (TRPL) as a function of the temperature for an ensemble of the InAsSb QDs outside of the photonic crystal structures.

4.5 On–going work

To get more insights on the optical properties of the devices at room temperature, we have designed and characterized cavities to operate at low temperature ($\lambda \sim 1200$ nm). At such low temperatures the analysis of the optical properties of the QDs is more feasible and their behavior when embedded in appropriate cavities will give as important information to go further with our devices operating at room temperature. Further work is necessary to implement the multimode character of our L9–PCM on the rate equation model.

Chapter 5

Analysis of the strong coupling regime of a quantum well in a photonic crystal microcavity and its polarization dependence studied by the finite–difference time–domain method

J. M. Llorens, I. Prieto, L. E. Muñoz–Camúñez, and P. A. Postigo

J. Opt. Soc. Am. B **30** (5) 1222–1230 (2013)

IMM–Instituto de Microelectrónica de Madrid (CNM–CSIC), Isaac Newton 8, PTM, Tres Cantos, Madrid E-28760, Spain

5.1 Context & motivation

The field of cavity quantum electrodynamics (cQED) has proved to be a tool to investigate quantum phenomena. One of the main applications has been in the field of quantum information. Finite difference time domain (FDTD) is a suitable method to understanding the physical phenomena in realistic structures. A method to properly establish the design of photonic crystal microcavities (PCMs) is presented. The framework of the work is the finite difference time domain, in which Maxwell equations are solved in the time domain.[75] Although the analysis has been particularized for an L7–photonic crystal microcavity in InP with an embedded quantum well, it is worth noting that the method can be generalized to other systems with other materials and other quantum nanostructures, like the Purcell effect in PCMs containing quantum wires (QWrs).[76, 65]

5.2 Contribution

My contributions in this work are:

- Set up of the parameters for the starting simulation by finite difference time domain (FDTD) of the L7–PCM,
- Optimization of the convergence of the cold cavity in the FDTD simulation,
- Scripting for the determination of the quality factor of the cavities through the discrete fourier transform (DFT),
- Discussion of the results.

5.3 Publication

5.3.1 Abstract

We provide a methodology for the study of a photonic crystal microcavity and a quantum well (QW) in the strong coupling regime by finite difference in the time domain. Numerical results for an InP L7 photonic crystal microcavity coupled to an ideal QW are provided. A comparison of the time analysis processed by the discrete Fourier transform, the Padé approximant, and harmonic inversion is

presented to optimize the computation time. We present a method to solve the uncertainty of the frequency spectrum depending on the starting time used in the spectral analysis. The influence of the polarization anisotropy on the strong coupling is studied. The Rabi splitting is exactly zero only when the induced polarization in the quantum well is aligned with a field component incompatible with the symmetry of the mode.

5.3.2 Introduction

There is an extensive number of devices based on the interaction between light and fundamental excitations of matter. When such an interaction overcomes a certain limit, the system enters into a coherent regime referred to as the strong coupling regime (SCR). Since the first experimental observation by Weisbuch *et al.*[77] of such regime in a planar microcavity embedding one or a few semiconductor quantum wells (QWs), there has been an steep rise in the scientific and technological advances in the field; see for instance the comprehensive monographes.[78, 79] The SCR technology has reached a level of maturity that allows its integration in more complex systems such as polaritonic integrated circuits. The design of optical circuits requires powerful numerical modeling tools to parametrize the circuit elements in an accurate way. In the field of electrodynamics, and recently at optical frequencies, the finite–difference time–domain method (FDTD) is among the most employed numerical methods.[75] Establishing a proper methodology for studying SCR systems by FDTD is the matter of this paper.

In this study, we present a numerical simulation of an L7 photonic crystal slab microcavity (PCM) embedding a single QW. The L7 microcavity is the result of removing seven consecutive holes of a row along the ΓK direction of a triangular lattice photonic crystal, hence creating a defect. This defect breaks the in-plane translational invariance. The impact on the photonic structure is the appearance of a series of discrete photonic modes characterized by a spatially localized distribution of its electric and magnetic fields. If the extension of the photonic crystal in its perpendicular direction is truncated (case of a slab), the electromagnetic field is confined in three dimensions as a result of the refractive index contrast. An exciton in a QW is also confined in the perpendicular direction as a results of the lack of translational invariance when compared to the semiconductor in its bulk form. Given that the QW is embedded within the photonic slab, the exciton would then also be sensitive to the holes of the photonic crystal. Such

holes act as barriers of infinite height on the electronic potential, breaking also the QW's in–plane translational invariance.[80] However, the exciton in–plane radius (typically of ∼10 nm in InAs/InP QWs[81, 82]) is significantly smaller than the typical triangular lattice constant (∼400 nm as it will be shown in the following sections) meaning that the quantization energies are expected to be very small. Even though the exciton confinement is weak, its wave function and the cavity modes are subject to an effective potential resembling the in–plane pattern, which formally means that both exhibit the same dimensionality making it possible to build up coherent polariton states.[80]

A similar system to that discussed here consists of a micropillar bounded by two distributed Bragg mirrors (DBM) embedding one or a few QWs at the antinode of the defect mode.[83] In this type of structure the cavity modes and exciton states are also confined in three dimensions. An in depth theoretical study of this system was reported by Panzarini and Andreani.[84] The authors noted that all photonic modes successfully couple with the exciton states once their relative difference in energy (detuning) is small enough. This happens because the quantization energies of the excitons are very small, and the exciton resonance can be seen as being composed of many degenerated states. However, the coupling is only significant when their respective quantum numbers take the same value. Therefore, by sweeping the micropillar radius a different mode couples efficiently to one of the exciton states of the degenerate energy level once their respective energies get close enough. Such behaviour is characteristic of a system which lacks of translational invariance, where the wave vector matching condition is not valid anymore.

We have adopted here a semi–classical approach, where the coupling between the QW and the PCM is accounted for implicitly by describing the fundamental exciton resonance as a Lorentzian–medium (full details are presented in Section 5.3.3).[85, 86, 87, 88, 89, 90] The phenomenology to be presented responds to a dynamic or AC Stark effect, *i.e.,* the effect of a rapidly varying field on a two–state system. In contrast to an accurate fully quantum treatment[84, 80, 91, 92], we assume that there always exists an exciton state with the same spatial extension as the QW that couples with the cavity modes if the energies of the states match. Our approach to the problem is that of a model study. To that end, we have used ideal parameters for the QW that serve for discussing specific physical situations. Perhaps, the most *idealized* parameter in this work is the exciton res-

onance linewidth. The exciton linewidth in InGaAs/GaAs QWs can been found between 2.7 meV in early experimental results on strong–coupling systems[86] to reach values smaller than 0.6 meV.[93] However, for InGaAs/InP QWs with emission at 1.5 μm the smallest exciton linewidth reported so far is 5.3 meV[94], further reduced to 3.5 meV in the presence of a magnetic field by removing the free carrier contribution to the broadening[95]. In the numerical computations presented in this paper, we have considered exciton linewidths smaller than 2 meV. However, the main conclusions of the study are not affected by this choice.

We have performed the simulation of the coupled system with a commercial software[39] to show that it is possible to identify the most characteristic features of a system in the SCR without the need of developing a customized solution. This is not the first time that a PCM coupled to a dipole is studied by FDTD.[96, 97] However, in these studies the system damping rates of the dipole and PCM mode are greater than the characteristic coupling, the system being in the weak coupling regime (WCR). The authors aim at system features of particular interest for laser applications. Recently, Taniyama *et al.* explored the SCR of a two–level system coupled to an L3-PCM by FDTD.[98] In their model, the initial condition of the calculation is the current density of a dipole corresponding to a Lorentz–like dispersive medium, as described by the auxiliary differential equation method.[75] Then, the dipole describing the two–level system serves as excitation source in the FDTD calculation. Our model is implicitly equivalent to that developed by Taniyama *et al.* We also describe the QW as a Lorentz–like dispersive medium, but we use an additional dipole to set the initial conditions. As a result of this approach, we are free to choose the properties of the excitation source in the FDTD simulation, *e.g.* position, bandwidth, etc. In the particular case of studying the stationary solution of Maxwell's equations, the excitation source should play the role of a fictitious source that injects its energy into the system without interacting with it. As we will see in the following section, H. Taniyama's approach results more appropriate for strictly studying the coupling between the PCM and the exciton dipole, while ours can in principle be generalized to a broader type of problems, although we limited ourselves here to using a dipole as the excitation source. The key issue tackled here lies in the freedom of choosing the excitation source. It introduces an uncertainty in determining the right time origin to perform the spectral analysis. There is a transient time, in principle unknown, between the injection of the energy and the start of the co-

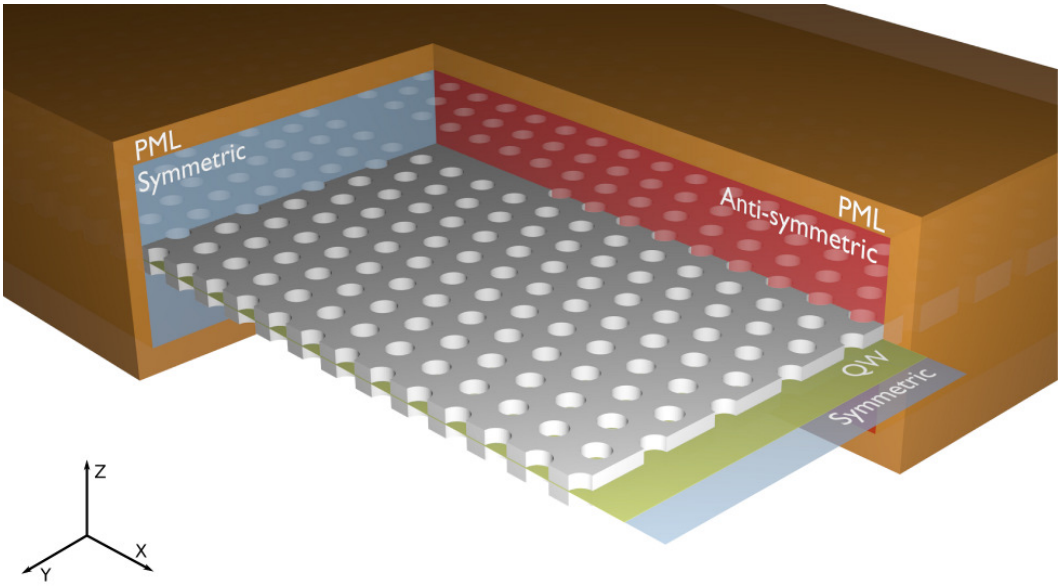

Figure 5.1: **Scheme including all the elements of the model.** Schematics of the modeled suspended L7–photonic crystal microcavity embedding a quantum well. Boundary conditions along X, Y and Z are used considering the symmetry of the cavity fundamental mode.

herent oscillation of the coupled PCM and QW. We will show that such difficulty can be easily overcome using the harmonic inversion method[99] for the spectral analysis. We further prove that we are able to reproduce the characteristic spectral features of a system in the SCR, namely the doublet spectral structure, the vacuum Rabi splitting maximum at equal damping rate and the anti–crossing as a function of the energy detuning. We close the study by exploring the dependence of the vacuum Rabi splitting on the polarization of the exciton dipole.

5.3.3 Theoretical model and time–signal analysis

Model details

The optical resonances of the PCM as well as those of the PCM embedding a QW are obtained by means of the FDTD method. The implementation of the FDTD adopted in the present work corresponds to that of the commercial package FDTD Solutions.[39] In Figure 5.1 we present a scheme of the PCM together with the simulation box and the symmetry planes for the sake of clarity. All the details of the simulation are described in the Appendix 5.3.6.

It is well established that within the linear response theory the polarization

induced in a nanostructure has a nonlocal character. It extends farther out from the nanostructure limits as a result of the exciton wave function penetration into the confining barrier.[100, 101, 102] Nevertheless, the local response theory was applied for the first time to study the SCR of barium atoms by Zhu *et al.*[103] Since then, it has been proven to be quite successful in modelling planar–like microcavities embedding QWs.[85, 86, 87, 90] In our model the QW is represented by a layer located at the centre of the slab with a local permittivity described by the functional form:[104]

$$\varepsilon(\omega) = \varepsilon_\infty \left(1 + \frac{\hbar\omega_{\mathrm{LT}}}{E_{X_0} - \hbar\omega - i\Gamma_{X_0}/2}\right), \quad \text{where} \quad \hbar\omega_{\mathrm{LT}} = \frac{1}{4\pi\varepsilon_0}\frac{2\pi\hbar^2 e^2}{\varepsilon_\infty m E_{X_0} L_{\mathrm{QW}}}\frac{f}{S}, \tag{5.1}$$

being $\hbar\omega_{\mathrm{LT}}$ the effective longitudinal/transverse splitting and, ε_0 and ε_∞ the vacuum and background permittivity, respectively; the Lorentzian–like resonance is centered at the exciton energy E_{X_0} presenting a linewidth Γ_{X_0}. The exciton oscillator strength per unit area is f/S in a quantum well of width L_{QW}. Finally, e and m are the free electron charge and mass. For the sake of simplicity in the discussion of the results, we assume that ε_∞ takes the same value as that of InP. Otherwise, only a small rigid shift of the spectral response would be expected given that $L_{\mathrm{QW}} \ll d$. As we are interested in the interaction of the PCM fundamental mode with the QW, we will consider the parameters of Eq. 5.1 to take empirical values. It is out of the scope of the present paper to perform a calculation of the QW electronic structure. This particular expression for describing the ground state of the exciton resonance of a QW (also known as $1s$ exciton), has been employed successfully for describing the polariton dispersion in photonic crystals [89] and, very recently, by Liscidini *et al.* in studying guided Bloch surface wave polaritons.[90]

We are leaving out of consideration the interaction of polaritons with other excitations of the solid, such as phonons or other polaritons. These interactions are the most effective channels of thermalization available to an eventual population of polaritons formed by a nonresonant optical excitation or electrical excitation.[**?**] The polariton–polariton interaction resulting from the coulomb interaction between the excitonic part of the quasiparticle plays a key role in physical systems such as polariton lasers.[105] In contrast, the polariton–electron interaction is a

very effective mechanism in cooling a polariton population down to its ground state giving rise to a Bose–Einstein condensate.[106] Finally the polariton–phonon scattering plays also an important role in thermalizing the "hot" polaritons along the exciton dispersion curve, which is crucial for explaining the photoluminescence spectra.[107, 108] In summary, our approach is only valid to provide a picture of a fully thermalized system.

A systematic approach of light–matter interaction effects where electron–hole pair excitations, their many–body interactions with material excitations and their coupling to the light field are treated on equal footing requires of very sophisticated microscopic models[109, 110, 111]. In combination with the FDTD method, some examples can be found in the literature, where the gain media is described by means of rate equations.[112, 97, 113].

Time–signal analysis

A very important part of the work relies on an accurate analysis of the electric field time evolution. Therefore, we devote the following lines to this particular issue. The solution of Maxwell's equations obtained by FDTD contains the electric and magnetic field spatial and temporal distribution. Photonic devices are commonly defined in terms of their spectral response. Therefore it is necessary to express this solution in frequency, *i.e.*, to compute its Fourier transform. We will show in the next section that FDTD predicts quality factors (Q factor) of ∼75000 for InP L7-PCMs ringing at ∼1.5 μm, meaning resonances of ∼0.2 Å linewidth. Profiling such sharp peak would require sampling frequencies smaller than ∼1 GHz. The time step at the wavelengths of interest is ∼0.1 fs, which would result in a simulation time of 1 ns or 10^7 time steps. Three approaches have been followed in this work to mitigate this computational burden: (i) discrete Fourier transform (DFT), (ii) harmonic inversion (HI) and (iii) Padé–Baker approximant (PBA). In the first case, the resonance position is located by direct inspection of the Fourier spectra. An error as big as the frequency resolution is expected. The Q factor is determined by fitting the curve to an exponentially damped signal.[39] The HI relies on fitting the signal to a superposition of harmonic signals, from which the resonance position and damping constant can be extracted.[99] We perform this task by means of the publicly available implementation Harminv.[114] The PBA approach exploits the ability of the Padé approximant to reproduce a function expressed as a power series. Our implementation relies on the Baker recursion

formula, as in [**?**]. From the computation of the approximant, the position and the width of the peaks can be easily and accurately determined, either by direct inspection or by fitting to Lorentzian curves.

Time–signal analysis of two oscillators

The analysis of the time signal of more than one harmonic oscillator presents a few difficulties that require clear identification to avoid misinterpretations. In FDTD simulations using a nonphysical excitation source, it is important to analyze the time signal once the energy of that source has been completely transferred to the elements of the simulation. Therefore, if the time signal analysis is taken over the whole of the simulation time, the spectral information of the source would be brought into the final field spectrum distorting the final result. A time window filtering is implicitly applied over the field components being monitored before moving to the frequency domain. We will see in Section 5.3.3 that depending on the starting time of the window, the final spectrum profile might notably change. We will derive here a few expressions corresponding to the power spectrum of the time signal of two harmonic oscillators filtered by a time window. Such a filter represents the starting time of monitoring and the final simulation time. The expressions depend on parameters that in the following sections will be used to fit the spectrum of two coupled oscillators representing the cavity mode and exciton resonance. The bounds of the time window are a key point to be considered when a time signal produced by more than one oscillator is analyzed, in particular the starting time, *i.e.*, the lower bound.

In general, the electric field resulting from an FDTD simulation of a PCM fundamental mode can be described as a single harmonic oscillator:

$$f(t) = \Theta(t - t_{\mathrm{i}})\Theta(t_{\mathrm{f}} - t)A\mathrm{e}^{i(\omega_0 t + \phi + i\alpha t)}, \tag{5.2}$$

where $\Theta(x)$ represents the step function and serves to filter the field signal between the time t_{i} and t_{f}. The field oscillations are characterized by an amplitude A, a frequency ω_0, a phase origin ϕ and a damping constant α. For simplicity, we will neglect from the analysis the upper limit of the time window t_{f}, which is fully justified as long as it is much bigger than $2\pi/\omega_0$. Under these considerations, the

Fourier transform of Eq. 5.2 is:

$$F(\omega) = A\mathrm{e}^{i\phi}\frac{\mathrm{e}^{-it_\mathrm{i}(\omega-\omega_0-i\alpha)}}{\alpha+i(\omega-\omega_0)}, \tag{5.3}$$

and its power spectrum:

$$P(\omega) = F(\omega)F^*(\omega) = A^2\mathrm{e}^{-2t_\mathrm{i}\alpha}\frac{1}{\alpha^2+(\omega-\omega_0)^2}. \tag{5.4}$$

In the case of a time signal resulting of the superposition of two oscillators $f(t) = f_1(t)+f_2(t)$, its power spectrum can be casted as $P(\omega)= P_1(\omega)+P_2(\omega)+P_\mathrm{c}(\omega)+P_\mathrm{c}^*(\omega)$, with $P_\mathrm{c}(\omega)=F_1(\omega)\ F_2^*(\omega)$. The explicit expression of $P_\mathrm{c}(\omega)$ for two general oscillators contains many terms that make the discussion difficult. For the sake of simplicity, we consider here two identical oscillators detuned one to each other by a frequency shift Δ and equal phase origin:

$$P_\mathrm{c}(\omega) = A^2\mathrm{e}^{-2t_\mathrm{i}\alpha}\mathrm{e}^{-it_\mathrm{i}\Delta}\left[\frac{1}{\alpha+i(\omega-\omega_0)}\frac{1}{\alpha-i(\omega-\omega_0-\Delta)}\right]. \tag{5.5}$$

The time t_i not only appears as a damping term as in Eq. 5.4, but also introduces a relative phase that would change the shape of the spectra depending on which portion of the time signal $f(t)$ is Fourier transformed. This change in phase introduces a serious difficulty if one employs direct spectrum analysis methods as DFT or PBA, while it should not pose any trouble to HI–like methods. We will go more deeply into this in the next section.

In practice, it is very difficult to determine the value of t_i in an FDTD calculation. Time–domain methods start by exciting one or few artificial sources and follow by letting the time to evolve until all the energy from that sources is fully transferred to the physical system–in our case, the fundamental mode of an L7–PCM. Therefore, there is not an exact time point at which the field oscillation starts, but a transitory time lapse. In order to get an accurate description of the power spectrum from the time signal, we have proceeded by making a nonlinear fit of PBA to $P(\omega)$ for the L7–PCM embedding a QW system. As we will see in the next section, a very good agreement is found with HI's output. The nonlinear regression has been performed using the self–adapting differential evolution algorithm[115] as implemented in the open–source optimization toolbox PyGMO.[116]

5.3.4 Results and Discussion

The numerical results have been obtained for a single InP L7-PCM of $r/a = 0.27$ with a lattice parameter $a = 410$ nm and a slab thickness $d = 237$ nm. This system has been studied in the past by some of us.[20] The dielectric constant of the InP layer is set to $\varepsilon_{\mathrm{InP}} = \varepsilon_\infty = 10.1$, *i.e.*, its value at $\lambda = 1458$ nm.[117] We have disregarded any dispersion of the InP given that we are looking at narrow–band effects. The QW excitonic resonance is tuned to the PCM fundamental mode. For the oscillator strength we have chosen the representative value of $f/S = 5{\times}10^{12}$ cm^{-2} and $L_{\mathrm{QW}} = 4$ nm. The rest of material parameters are chosen to meet the specific needs of the matter being discussed.

Spectral properties of InP L7-PCM

In what follows, we use the InP L7–PCM without QW as a testbed for comparing the results of the time analysis algorithms introduced in the preceding section, namely PBA, HI and DFT. The comparison is made from a simulation evolved for 75 ps at a time step of 0.026 fs. The first two methods put to test agree on a value $\hbar\omega_0 = 847.667$ meV for the fundamental resonance of the E_y component, while DFT finds that resonance at 847.656 meV, *i.e.*, a relative shift of 0.001%. This error is completely negligible when compared with the reported experimental values of the vacuum Rabi splitting for analogous systems[118, 119]. The corresponding quality factor values are: 77790 (DFT), 77790.8 (PBA) and 77796.4 (HI). The differences are again very small. However, a simulation of 75 ps takes significant computational resources ($\sim 2.9{\times}10^6$ time steps).

In order to establish a suitable simulation time we have studied the dependence of the resonance position and quality factor as a function of this parameter. The resonance position is well reproduced by all methods even for times as short as 1 ps. The convergence of the quality factor is shown in Figure 5.2 panel (a). DFT and PBA methods show very good convergence with respect to the value obtained for a 75 ps simulation. However, HI shows a fast oscillating behaviour and a much larger error. Indeed, we have multiplied its relative error y a factor $4{\times}10^{-4}$ to bring it to scale. Such convergence difficulties of the HI method are already reported in the literature.[120] The power spectrum corresponding to the fundamental defect mode of the PCM is shown in Fig. 5.2(b). The spectra corresponding to two cases are displayed. The first is a simulation of 3 ps, where

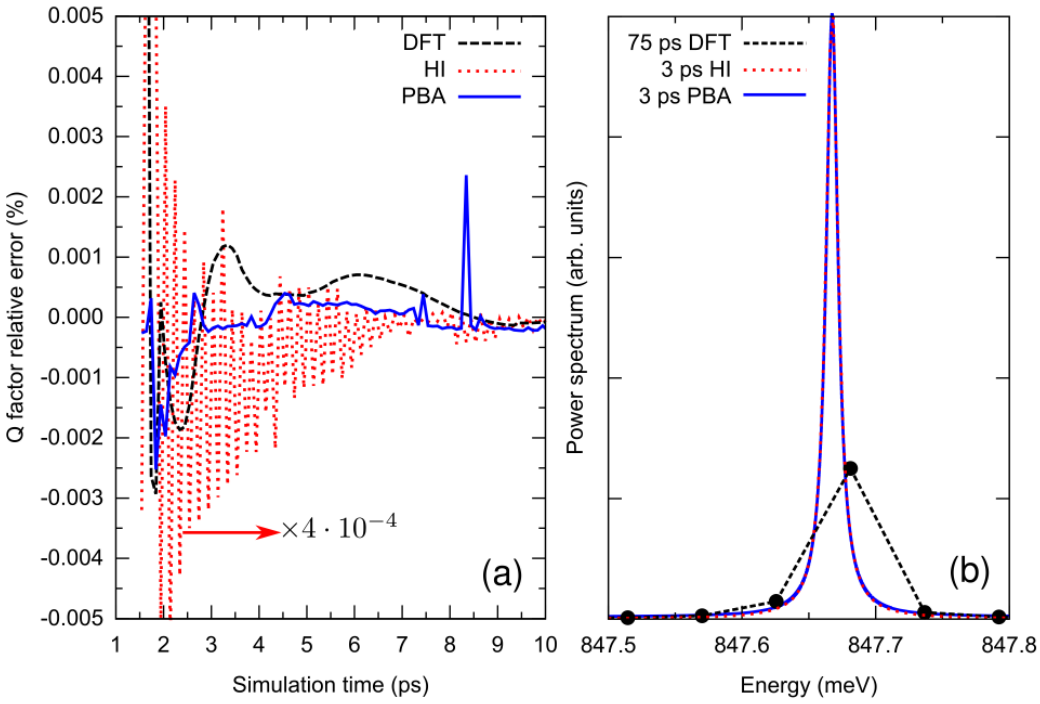

Figure 5.2: **Analysis of the quality factor of the cavity fundamental mode.** (a) Quality factor relative error with respect to its value at 75 ps. The results corresponding to the HI method are multiplied by a factor $4{\times}10^{-4}$. (b) Comparison of the fundamental resonance power spectrum obtained by applying DFT of the E_y component simulated during 75 ps (dot line) with the spectra obtained by PBA (solid line) and HI (dashed line) of E_y simulated for 3 ps.

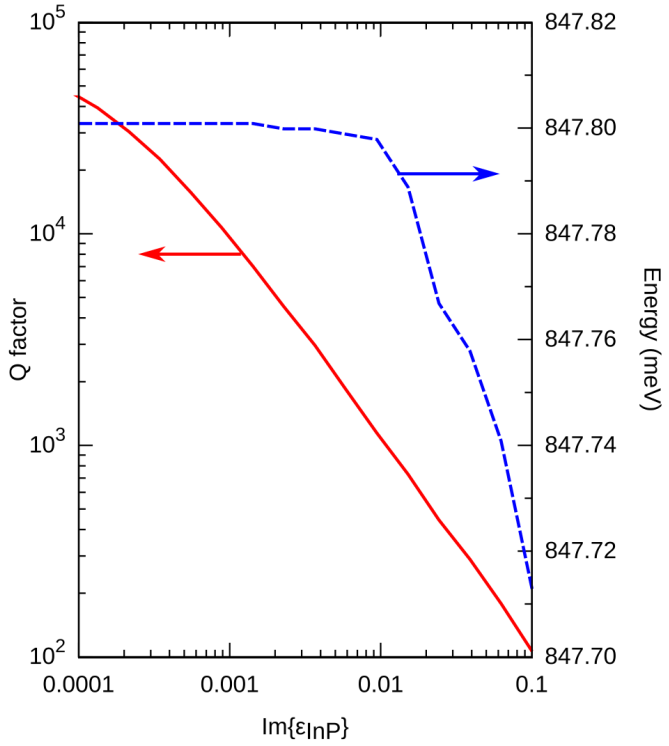

Figure 5.3: **Quality factor of the cavity fundamental mode in an absorbing medium.** Impact of a nonzero imaginary part of the dielectric constant of the InP material on the quality factor of the fundamental mode (solid red line) and on its resonance position (dashed blue line).

the power spectrum of the E_y component is obtained by HI and PBA methods. The second is of the same field component but simulated for 75 ps and obtained by DFT. The interpolation power of HI and PBA methods is evidenced in the plot. Even after $\sim 2.9\times10^6$ time–step calculation, the DFT method can only roughly reproduce the spectrum, otherwise, clearly outlined by HI and PBA of a 3 ps signal.

We close the part of the work devoted to the empty cavity by studying the effect of changing the imaginary part of the InP dielectric constant. We show in Fig. 5.3 that changing $\mathrm{Im}\{\varepsilon_{\mathrm{InP}}\}$ between 1×10^{-3} and 0.2, affects greatly the Q factor, while preserving almost unaffected the resonance position. Indeed, it experiences a variation of 88 μeV, *i.e.*, a 0.01% relative change. This result will let us tune the Q factor of our cavity at will, allowing us to study the dependence of the Rabi frequency on the PCM losses. We address this problem in the following sections.

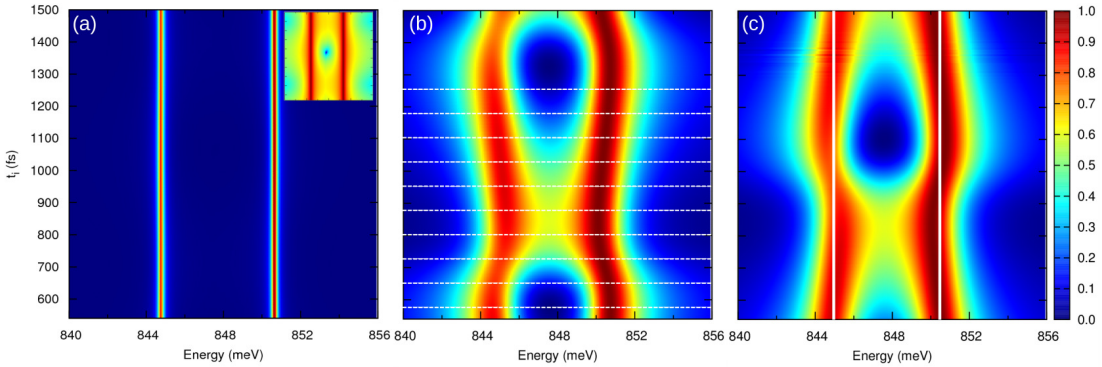

Figure 5.4: **Doublet on the L7–photonic crystal microcavity embedding a quantum well.** (a) Normalized power spectrum obtained by the PBA method taking different initial times $t_{\rm i}$ up–to 1500 fs of an InP L7–PCM embedding a QW of $E_{X_0} = 847.657$ meV, $\Gamma_{X_0} = 0.5$ meV (in logarithmic scale in inset). (b) Similar to (a) but for an InP with $\mathrm{Im}\{\varepsilon_{\rm InP}\}$ =6×10^{-3} (≈0.5 meV linewidth) embedding a QW of $\Gamma_{X_0} = 5.0$ meV. (c) Similar to (b), except the power spectrum is obtained by the HI method.

Spectral properties of InP L7-PCM embedding a QW

The insertion of a QW at the centre of the PCM has a notable impact on the power spectrum. If the QW emission is close to resonance with one of the defect modes of the PCM and the excitonic lifetime is long enough, the single peaked spectrum of Fig. 5.2(b) becomes a doublet, as shown in Fig. 5.4(a). We first consider the case of a QW defined by an exciton energy of 847.657 meV and a linewidth of 0.5 meV. The contour plot represents the power spectra obtained by the PBA method windowing the E_y component of the electric field values at different times $t_{\rm i}$. The two parallel straight lines of the contour plot denote the two resonances associated to the vacuum Rabi splitting. The two peaks are located at 850.652 and 844.717 meV, with FWHM 0.252 and 0.255 meV, respectively. Hence, the Rabi splitting results to be 5.935 meV. This value is consistent with the experimental values reported for comparable systems, five QWs in GaAs[118] and three QWs in InP.[119] However, a detailed study should be made before extracting any quantitative conclusion because these experimental systems contain a few QWs and we have considered only one (see Chapter 4 of Ref.[121] for particularities on this matter). In addition, the optical properties of InGaAsP/InP QWs emitting at 1.5 μm are different from those operating at shorter wavelengths (0.835 μm in [118] and 0.911 μm in [119]). In Section 5.3.3 we worked on the analytical expression of the power spectrum of two oscillators.

There, we found that the power spectrum could exhibit a strong dependence on the starting time of the data–window applied to the electric field signal (see Eq. 5.5). The two main effects are (i) an exponential damping of the spectra (second factor in r.h.s of Eq. 5.5) and (ii) a phase difference (third factor in the same equation). The damping is unnoticeable because we have normalized the spectra for the sake of clarity; otherwise the spectra doublet structure would become blurred. The impact of the phase difference between resonators is very faint for this system. It is however not fully negligible, as can be appreciated in the log plot shown in the inset of the figure, but it is safe to be ignored in the present case. The situation just described clearly depicts an SCR. By increasing the damping rates, we are weakening the coupling. We have increased the losses in the InP slab and also increased the exciton linewidth. The results shown in Fig. 5.4(b) remarkably contrast with those of Fig. 5.4(a). The two thin straight lines have turned into two broad resonances which get closer and farther apart as t_{i} changes. It is now difficult to identify the value of the vacuum Rabi splitting, given that the distance between the peaks oscillates. Even though one could think that the HI method could be more insensitive to t_{i}, we show in Fig. 5.4(c) that a similar result is obtained, but with a phase shift. The two white straight lines indicate the frequency of the two harmonics identified by the HI method at each t_{i}. The fact that the fitted resonance positions do not change with t_{i} supports the hypothesis that the waving structure of the contour plot has its origin on the phase difference introduced by it (see Eq. 5.5). Thus, in principle no more elements need to be introduced to understand the results shown so far.

To retrieve the whole of the information from the FDTD calculation, we have fitted the spectra located at the white lines of Fig. 5.4(b) to the general $P(\omega)$ expression derived in the previous section (the damping constants of both oscillators are not set equal anymore). The minimized objective function is defined as:

$$f_{\mathrm{obj}} = \sum_i \sum_j \left| \frac{P_{t_{\mathrm{i},i}}(\omega_j)}{\max(P_{t_{\mathrm{i},i}}(\omega))} - \frac{S_{t_{\mathrm{i},i}}(\omega_j)}{\max(S_{t_{\mathrm{i},i}}(\omega))} \right|^2, \tag{5.6}$$

where $S_{t_{\mathrm{i},i}}(\omega_j)$ represents the contour plot values of Fig. 5.4(b) at the discrete points defined by $t_{\mathrm{i},i}$ and ω_j. The function $P_{t_{\mathrm{i}}}(\omega)$ is defined by an amplitude A, frequency ω_0, phase ϕ and damping rate α for each of the two oscillators. As initial guess we set the parameters of the oscillators equal to those obtained from the HI method at t_{i}=540 fs, except for ϕ which is set to zero to not bias the

fitting process. Details of the fitting procedure appear in Appendix 5.3.6. From the comparison of the optimal parameters and those found by the HI method, we can conclude that the two oscillators were accurately determined already by the HI method. This was anticipated above, when we discussed the resonances frequencies in Fig. 5.4(c) and we found that they were insensitive to t_{i}.

One of the main results is the optimal value of $t_{\mathrm{i},0}$, *i.e.*, the t_{i} of the first fitted line: 119 fs. This means that the spectrum obtained by transforming the electric field from $t_{\mathrm{i},0}$ onwards can be reproduced by the spectrum of two oscillators just by applying the corresponding time shift. Hence, the waving pattern can be reproduced by the power spectrum of the simple model. Now we can finally show the evolution of the power spectrum from $t_{\mathrm{i}} = 0$ onwards. The contour plot in Fig. 5.5(a) shows that evolution. It contains the power spectrum of the two oscillators model with the optimal parameters. The pattern obtained as a function of t_{i} can be reproduced without introducing any frequency shift, only the interference $P_{\mathrm{c}}(\omega)$ terms suffice. The quality of the fit can graphically be attained by visual comparison of the region bounded within the two straight white lines and Fig. 5.4(b). The time scale is displayed in terms of the detuning parameter Δ (5.496 meV) to evidence the periodic character of the function predicted in Eq. 5.5. In the same Figure we have also included $|E_y(t)|$ in logarithmic scale as a semi–transparent layer at the left hand side to show the correlation between the power spectrum features and the actual electric field beating at the Rabi frequency. The spectrum obtained by setting $t_{\mathrm{i}} = 0$ is shown in Fig. 5.5(b). The solid line corresponds to $P(\omega)$ at $t_{\mathrm{i}} = 0$ calculated from the optimal values for the oscillator parameters. Analogously, the dot symbols represent the spectrum taking as input parameters the results of the HI method but setting $\phi_1 = \phi_2 = 0$, *i.e.*, the starting values of the optimization process. Both curves agree very well on the shape of the spectrum, in terms of peak positions and linewidth. We also show the power spectrum obtained by the PBA method as square symbols taking $t_{\mathrm{i}} = 458.2$ fs. This is the time origin determined by the fitting procedure (more details are reported in Appendix 5.3.6). The agreement on the power spectrum profile between the HI and PBA methods and the simple analytical model is clearly seen in the plot. Therefore, we can conclude that in order to retrieve the power spectrum from the output of the FDTD simulation it is enough to analyze the time series with the HI method, but disregarding the phase information. Indeed, in what follows we use this procedure in retrieving the frequency spectra

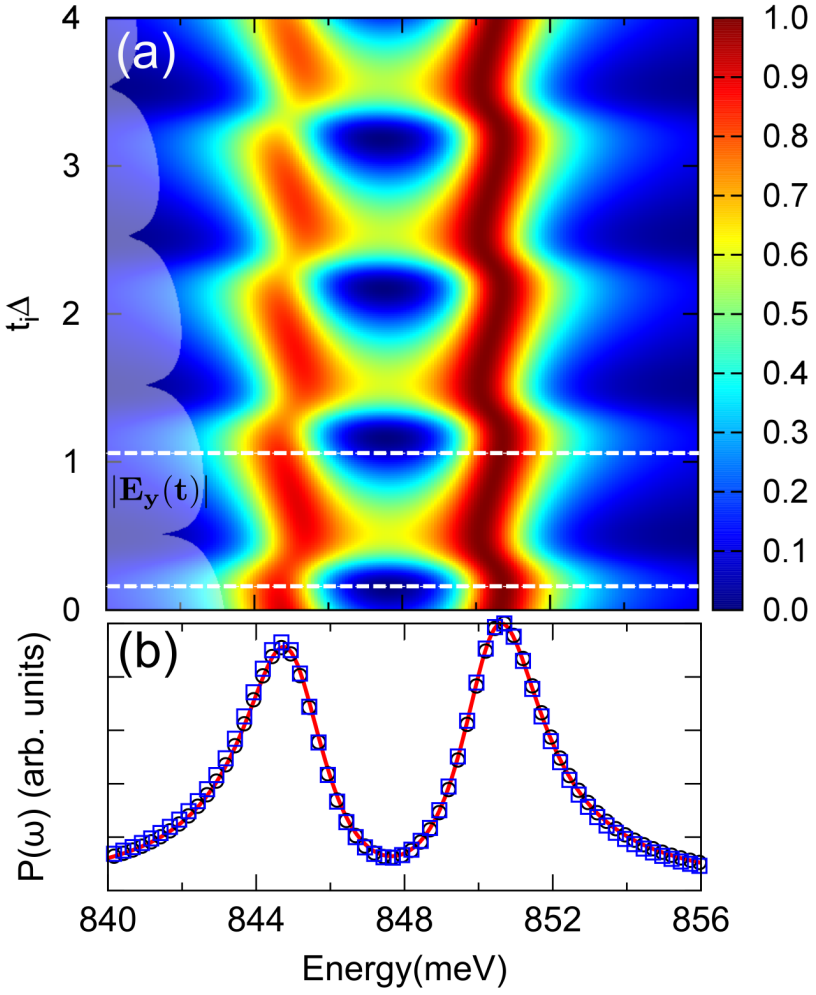

Figure 5.5: **Analysis of the Rabi splitting on the L7–photonic crystal microcavity embedding a quantum well.** (a) Contour plot of $P_{t_i}(\omega)$ generated with the parameters obtained after fitting the ten spectra indicated in Fig. 5.4(b) (see text for further details). The partial transparent plot at the left–hand side corresponds to $|E_y|$ shown in logarithmic scale. (b) Power spectrum obtained from the $P(\omega)$ expression setting $t_i = 0$ (solid line), by the HI method removing the phase difference information (dot symbols) and by the PBA method (square symbols) taking as t_i the time origin derived from the fitting.

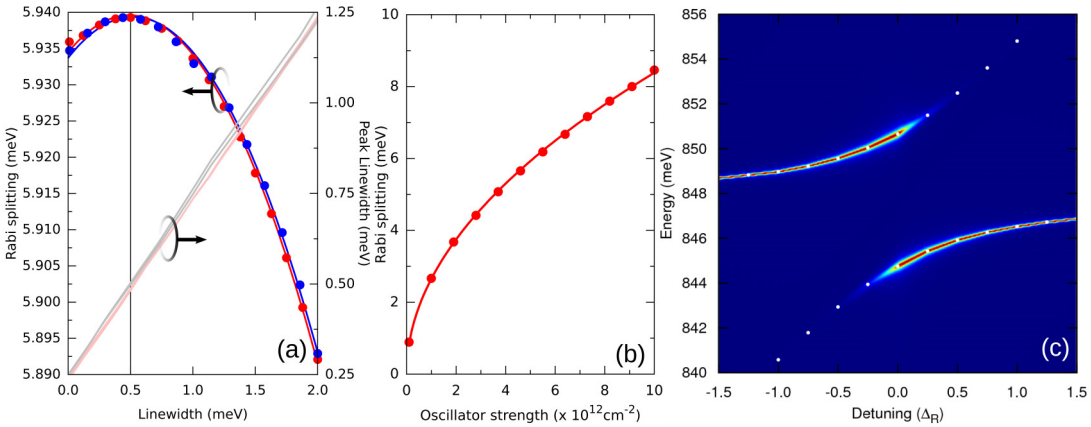

Figure 5.6: **Rabi splitting as a function of the linewidth, the oscillator strength and the detuning.** (a) Dependence of the Rabi splitting on Γ_{X_0} for $\Gamma_{\mathrm{Ph}} = 0.5$ meV (red dots) and on Γ_{Ph} for $\Gamma_{X_0} = 0.5$ meV (blue dots). The solid lines represent the fitting to a two–oscillators model (see text). Light red and blue lines indicate the evolution of the linewidth of the Rabi doublets on the respective Γ parameters. (b) Evolution of the Rabi splitting with the oscillator strength by unit area f/S for $\Gamma_{X_0} = \Gamma_{\mathrm{Ph}} = 0.5$ meV (red dots). The solid line is the result of a fitting to a square root law. (c) Contour plot of the power spectrum as a function of the detuning. Each spectrum is normalized. The white dots indicate the maxima of the Rabi doublet.

from the FDTD simulations.

Analysis of the system parameters

In the previous sections we have outlined the methodology to obtain the power spectrum of the electric field in the coupled system PCM–QW. In what follows, we show that this methodology is able to describe the characteristic features of a system in the SCR. We start the analysis by showing the dependence of the Rabi splitting and peaks linewidth on the cavity and QW losses, *i.e.*, the problem parameters Γ_{X_0} and Γ_{Ph}. In Figure 5.6(a), we show this dependence with red dots and blue squares, respectively. In both cases, the complementary linewidth is kept fixed to 0.5 meV. We also show the evolution of the peak linewidth with lines plotted in lighter colors. The two main characteristic features of this Figure are (i) Rabi splitting exhibits a maximum exactly at $\Gamma_{X_0} = \Gamma_{\mathrm{Ph}} = 0.5$ meV and (ii) the linewidth of each peak is $(\Gamma_{X_0} + \Gamma_{\mathrm{Ph}})/2$. Both results are predicted by any of the models reported in the literature where the coupling of bosonic excitations are object of study; see, for example, [100, 101, 122]. A less rigorous but

more intuitive derivation of the frequency and linewidth of the resulted coupled system can be retrieved following the quantum mechanics textbook of C. Cohen-Tannoudji *et al.*[123] Let us assume a system of two levels coupled by a purely nondiagonal perturbation g, the eigenvalues of such system are:

$$E_{\pm} = \frac{1}{2}(E_1 + E_2) \pm \sqrt{\left(\frac{E_1 - E_2}{2}\right)^2 + g^2}, \tag{5.7}$$

where E_1 and E_2 are the energies of the unperturbed levels. Now, let us suppose that the levels are unstable being characterized by the lifetime $\tau_i = \hbar/\Gamma_i$. To take into account the fact that the two levels are not isolated but are part of a larger system–*i.e.*, that they exhibit losses–it is formally sufficient to introduce complex energies: $E \to E - i\Gamma/2$. After transforming Eq. (5.7), the final energies of the coupled system become

$$E_{\pm} = \frac{E_1 + E_2}{2} - i\frac{\Gamma_1 + \Gamma_2}{4} \pm \sqrt{\left(\frac{E_1 - E_2}{2} + i\frac{\Gamma_2 - \Gamma_1}{4}\right)^2 + g^2}. \tag{5.8}$$

The linewidth can be derived from the time–energy uncertainty $\Delta E \simeq \hbar/\tau = \Gamma$, *i.e.*, $\Delta E \simeq 2\mathrm{Im}\{E_{\pm}\}$. After fitting the symbols to the real part of Eq. 5.8, we obtain $g = 2.96976 \pm 7 \times 10^{-5}$ meV and $\Gamma_{\mathrm{Ph}} = 0.491 \pm 0.004$ meV for the case of varying Γ_{X_0} (dots) and $g = 2.9697 \pm 1 \times 10^{-4}$ meV and $\Gamma_{X_0} = 0.519 \pm 0.006$ meV for the case of varying Γ_{Ph} (squares). The results are in very good agreement with the input parameters showing that the actual numerical results follow the expected theoretical behaviour.

At the condition of maximum coupling, *i.e.*, $\Gamma_{X_0} = \Gamma_{\mathrm{Ph}}$, the Rabi splitting is only a function of the oscillator strength and the cavity photon confinement, as noted by Houdré *et al.*, [124]. To show that our numerical calculation indeed reproduces such reasoning, we have computed the Rabi splitting as a function of f/S. These results and the fitting to a square root law are shown in Fig. 5.6(b). The same calculation was performed by Taniyama *et al.* [98] to show the square root dependence on the oscillator strength.

The final footprint of a system in the SCR addressed in this section is the anti–crossing of the upper and lower polariton branches as a function of the detuning between the excitonic and the microcavity mode resonances. To this end we have performed a series of simulations where we have varied E_{X_0} without modifying

the microcavity. In Figure 5.6(c) we show a contour plot composed of the power spectra at different detuning values. In this calculations we have set $\Gamma_{X_0} = 0.5$ meV and Γ_{Ph} =0.011 meV ($\mathrm{Im}\{\varepsilon_{\mathrm{InP}}\} = 0$). The abscissa axis is normalized to the Rabi splitting $\Delta_{\mathrm{R}} = 5.935$ meV. In the contour plot it is possible to recognize very easily the aforementioned anti–crossing together with the increase in the spectrum broadening as the detuning approaches zero. In this calculation, the exciton line fades out as the detuning increases, since we are feeding light into the microcavity. To help the reader in identifying the anti–crossing character, we have introduced two white dotted lines pointing to the two maxima of the spectra at each detuning value.

Impact of the QW polarization anisotropy

As is usually the case, we have assumed that the QW behaves electromagnetically as an in–plane isotropic material, *i.e.*,

$$\boldsymbol{D} = \varepsilon \begin{pmatrix} 1 & 0 & 0 \\ 0 & 1 & 0 \\ 0 & 0 & 0 \end{pmatrix} \boldsymbol{E}, \tag{5.9}$$

meaning that the induced QW polarization lies always within the QW's growth plane. This is usually the case in QWs given the small mixing between the heavy and light hole bands.[125] In this final section, we will address the question of how would impact an eventual QW material anisotropy on the Rabi splitting. We will consider only the case of a diagonal dielectric function:

$$\varepsilon_{ij}(\omega) = \varepsilon_{\infty} + \begin{pmatrix} \cos\varphi \sin\theta & 0 & 0 \\ 0 & \sin\varphi \sin\theta & 0 \\ 0 & 0 & \cos\theta \end{pmatrix} \frac{\varepsilon_{\infty}\hbar\omega_{\mathrm{LT}}}{E_{X_0} - \hbar\omega - i\Gamma/2}. \tag{5.10}$$

This is just a modification of Eq. 5.1 to introduce the tensor character. The angles φ and θ are the azimuth and polar angles, respectively. We are implicitly assuming that the QW material principal axes are parallel to the Cartesian axes of the L7–PCM.

In Figure 5.7(a), we show in foreground a polar plot of the Rabi splitting as a function of the azimuth angle for $\theta = \pi/2$. We have considered $\Gamma_{X_0} = 0.5$ meV and $\Gamma_{\mathrm{Ph}} = 0.011$ meV ($\mathrm{Im}\{\varepsilon_{\mathrm{InP}}\} = 0$) in this calculation. The value of the

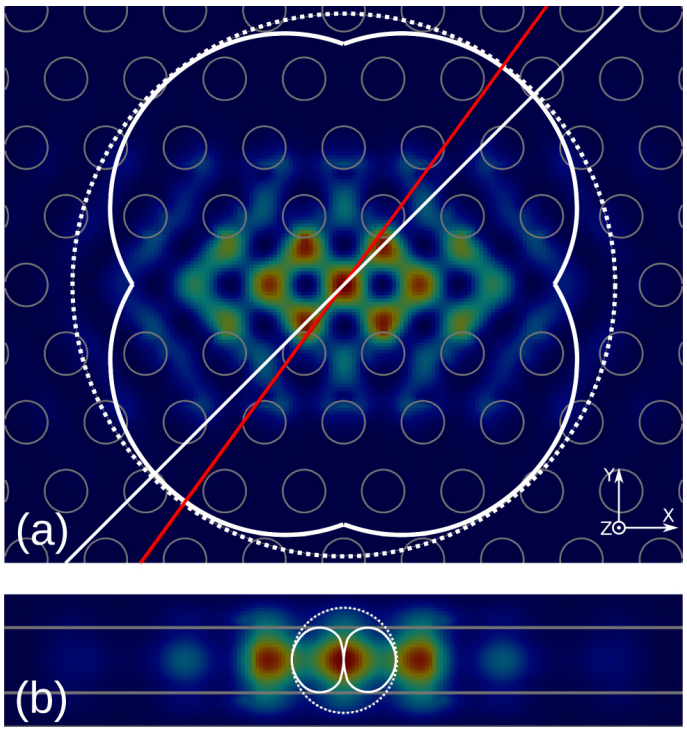

Figure 5.7: **Rabi splitting as a function of the dipole orientation.** (a) Rabi splitting as a function of the azimuth of the dipole orientation. The white dotted circle is of radius equal to the maximum value of the Rabi splitting, denoted by the diagonal red line. In background, the $|E|^2$ is plotted. The white line points to the azimuth $\pi/4$, along which $|E|^2$ is plotted in (b). In foreground of (b) we show the Rabi splitting as a function of the polar angle inscribed inside of a white circle of radius equal to the maximum of the Rabi splitting. The two horizontal white lines indicate the slab interfaces.

Rabi splitting is derived from the spectral analysis of the E_y field component. To facilitate the comparison, we have inscribed the polar plot inside a circle of the same radius as the maximum Rabi splitting, $\Delta_{\mathrm{R}} = 5.958$ meV. This value corresponds to a orientation of the in–plane dipole of $\varphi = 54°$ and it is slightly higher even than that obtained at maximum coupling in Fig. 5.6(a). In order to identify the origin of such an increase in the coupling when the polarization points along this direction, we have represented in background a schema of the L7 microcavity top–view together with a dashed line oriented 54° with respect to the X–axis. It is certainly intriguing that this angle does not coincide either with the symmetry angle of the underlying triangular photonic crystal ($\pi/3$) or with the angle connecting the maximum field intensity $|E|^2$ ($\pi/4$) (shown in the figure background for the sake of completeness). Looking more carefully at the electric field orientation angle at each node of the mesh, it is possible to calculate its average value as $\varphi = \arctan(\sum_i |E_y(\boldsymbol{r}_i)| \,/\, \sum_i |E_x(\boldsymbol{r}_i)|) = 53.53°$. Hence, the increase in the Rabi splitting coincides with the alignment of the dipole with the electric field. In addition, it is worth mentioning that the power spectrum of the E_y component exhibits a Rabi doublet even in the case that the dipole is oriented along the X-axis. It is well known that the fundamental defect mode of an L7-PCM is polarized in the far–field along the Y-axis[126]. Hence, one can not derive from this fact any sort of selection rule on whether the exciton dipole would or would not couple to the fundamental mode. Any in–plane orientation of the dipole would result in a strong coupling of QW–PCM given that E_x and E_y components are different from zero. This is not the case of $\theta \neq \pi/2$. For an ideal L7–PCM the fundamental defect mode has an exact zero E_z component in the XY plane at $z = 0$, *i.e.*, in the area occupied by the QW. Therefore as we reduce the in–plane projection of the dipole by making θ approach zero, the field–matter coupling would reduce accordingly. This is confirmed in Fig. 5.7(b), where we show a polar plot of the Rabi splitting for $\varphi = \pi/4$. The maximum value is achieved when the dipole lies in the XY–plane and it reduces in a nonlinear way as θ reaches zero. As Figure 5.7(a), we show a slice cut of $|E|^2$ in background. It can be easily appreciated that the field intensity is maximum in the direction contained in the XY–plane. Along the Z direction it is not zero, but in this case the actual meaningful magnitude is the value of the E_z component. These results show that the strong coupling is quite robust to the orientation of the dipole, only at $\theta = 0$ does the coupling vanish exactly.

5.3.5 Conclusions

We have presented a careful study on the simulation of a PCM embedding a QW within the local linear response theory by FDTD. We have shown that the analysis of the time domains electric field of a coupled system is far from being straightforward. Depending on the damping rates of the cavity mode and exciton resonances, the power spectrum greatly depends on the time window employed in the frequency transform of the signal. Moreover, the time windowing of the electric field time evolution also distorts the spectrum obtained through the HI method. Fitting the results to the analytical expression of the Fourier transform of two harmonic oscillators, we have successfully identified that the dependence of the spectra structure on the initial time has its origin on a phase difference between the oscillators. After establishing the methodology for the frequency analysis, we have successfully characterized the PCM–QW system in the SCR. Finally, we have seen that even though the far field of the fundamental mode of an L7–PCM is linearly polarized, the coupling takes place for any orientation of the material excitonic polarization.

5.3.6 Appendix

Numerical details

We have included in this appendix the numerical details needed to reproduce the results shown in this paper with the FDTD Solutions software. The different elements of the simulation are depicted in Figure 5.1 for the sake of clarity. Perfectly matching layer (PML) boundary conditions are imposed at the simulation box. The meshing of the structure is defined by three domains: the slab interface, the QW interface and the air regions. The slab and QW interface regions are discretized by means of a uniform mesh to ensure, first, that the holes of the triangular lattice are depicted by the same number of points ($\Delta x = a/n_x$ and $\Delta y = a\sin(\pi/3)/n_y$), and second, that the slab and QW interface lie exactly at half height of a Yee cell to minimize the impact of refractive index interpolations across the surfaces. The air regions are discretized by a nonuniform mesh along the Z direction to minimize the number of nodes in the calculation. Subcell accuracy is brought into the model by enabling a conformal meshing. Finally, to speed up the computation only one eighth of the whole structure is actually discretized by adding two symmetric planes (YZ and XY) and one antisymmetric

plane (ZX), *i.e.*, compatible with the fundamental mode symmetry.[20]

The dimensions of the simulation box are defined as 7 times the slab thickness d in height, and 25 times the lattice constant in the X direction and 18 holes rows in the Y directions. The uniform meshing is defined by $n_x = n_y = 20$ and $\Delta_z = 4$ nm.

The excitation source is a magnetic dipole oscillating at 205 THz, with 100 fs of pulse length, 250 fs of offset and 5 THz of bandwith for the L7 bare cavity simulation. For the coupled system we have reduced the bandwidth of the source to avoid the excitation of higher energy cavity modes, being the source settings: 205 THz frequency, with 150 fs of pulse length, 350 fs of offset and 2.94 THz of bandwith. The value of the electric field at the cutoff is about four orders of magnitude weaker than at the maximum, concluding that no artifacts are introduced in the simulation. The soruce is displaced from the origin of the simulation and located at an antinode of the H_z component to maximize the coupling with the mode. Due to the symmetry planes introduced in the model there are actually eight sources injecting light into the PCM. The time monitor is placed close to the origin, where the E_y field component presents an antinode.[20] If not said otherwise, the starting time is 540 fs and the stop time 3000 fs with a sampling rate of 0.41 fs.

Fitting details

The optimization process is initiated with the set of parameters obtained from the HI analysis. Let us denote the set of parameters for each oscillator by the array $\{A, \hbar\omega_0, \hbar\alpha/\pi, \phi\}$, A being the amplitude, ω_0 the resonance frequency, ϕ the phase origin and α the damping rate. The starting values of the parameters are: {118, 844.934, 2.75, 0} and {123, 850.430, 2.71, 0} for the oscillators. The frequency and damping rate are expressed in milli–electron volts. The time t_i of each of the curves being fitted is $t_{\mathrm{i},i} = t_0 + i\Delta t$, with $t_0 = 577.6$ fs and $\Delta t = 75.12$ fs. The optimization algorithm returns the following set of oscillators related parameters at the minimum of f_obj: {152, 844.967, 2.77, 0} and {157, 850.409, 2.71, 0}. The $t_{\mathrm{i},i}$ values found by the optimizer are almost equally spaced, with $t_0 = 119.4$ fs and the mean Δt 75 fs with a mean deviation of 8 fs. The physical meaning of t_0 is related to the time–lapse at which the cavity mode and exciton start to beat coherently, which can be located around 119 fs before $t_{\mathrm{i},0}$, *i.e.*, 458.2 fs. This time origin is physically more relevant than the exciting source

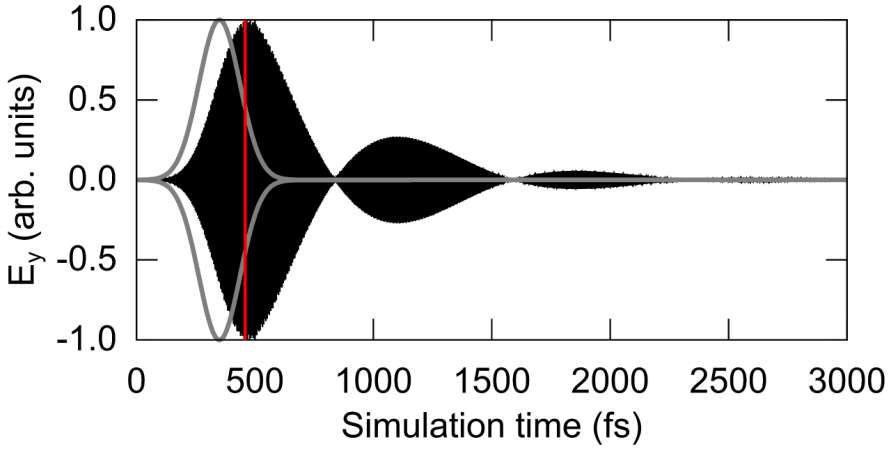

Figure 5.8: **Time evolution of the E_y.** Electric field component E_y monitored from the simulation time origin until 3000 fs (black line). Envelope of E_y of the excitation dipole (grey line). Position of t_0 with respect to the simulation time origin, 458.2 fs (vertical red line).

switch–on instant. An accurate determination of this time might be of relevance in simulations of high–speed optical switches based on strong coupling effects.[**?**] To graphically show the electric field evolution at this particular time instant, we present in Figure 5.8 $E_y(t)$ monitored since the beginning of the simulation time. The instant t_0 is denoted by a vertical line. It corresponds with the maximum of the first beat. For the sake of completeness we have also included in the Figure the excitation dipole envelope. The contribution of this electric field is not clearly seen in the black curve, because the position of the excitation dipole and the time monitor are different, as specified in Appendix 5.3.6.

5.4 On–going work

This work demonstrates the capability of the FDTD to analyse quantum phenomena occurring on photonic crystal microcavities with an embedded quantum well (QW). The next step in the research of such systems is to decrease the dimensionality of the quantum nanostructure to reproduce quantum wires (QWrs) and quantum dots (QDs). In particular, the modelling of those L7–PCMs in InP with quantum wires will give insights on the capabilities of the experimental results obtained in high–Q PCMs. Particularly interesting is also the incorporation of quantum dots in those systems. That would enable the evaluation of the

capabilities of our high–Q PCMs both in GaAs and InP embedding QDs. To go beyond the Lorentz model, we are currently describing the QWr/QD on the base of a rate equation model. In the future, we will use a guided mode of a waveguide to excite a nanostructure located inside the defect cavity. In this way we will analyze the interaction taking place in an integrated optical circuit.

Chapter 6

Different strategies towards the deterministic coupling of a single quantum dot to a photonic crystal cavity mode

I. Prieto,[1] J. Herranz,[1] Y. González,[1] J. Canet–Ferrer,[2] L. Wewior,[1] P. A. Postigo,[1] B. Alén,[1] L. González,[1] M. Kaldirim,[1] L. E. Munioz–Camuniez,[1] D. Fuster,[2] A. G. Taboada,[1] J. M. Ripalda,[1] F. Briones,[1] G. Muõz–Matutano,[2] and J. P. Martínez–Pastor[2]

13^{th} International Conference on Transparent Optical Networks (ICTON), 2011.

[1]IMM–Instituto de Microelectrónica de Madrid (CNM–CSIC), Isaac Newton 8, PTM, E–28760 Tres Cantos, Madrid, Spain

[2]UMDO, Instituto de Ciencia de Materiales, Universidad de Valencia, P.O. Box 22085, 4607 Valencia, Spain

6.1 Context & motivation

Several methods have been demonstrated to achieve strong coupling between a single quantum dot (QD) and a photonic crystal microcavity (PCM) mode.
The first achievement of QD–PCM operating in the strong coupling regime [26] stem from an statistical approach. A large array of cavities were fabricated and, eventually, one of them contained a QD exhibiting both spectral and spatial matching. The same approach was followed by Nomura et al.[28] to demonstrate lasing of a single QD strongly coupled to the L3–PCM fundamental mode. Over the years, other authors presented different strategies to increase the yield towards the deterministic QD–PCM, in samples with self–assembled QDs [8, 127] or with those fabricated in specific positions.[128] We present two different strategies that we have followed to produce such systems. They are based on the technological procedures to etch photonic crystals in GaAs, that allowed us to obtain other results in the field of c–QED using PCMs embedding quantum rings.[129, 130, 131, 29, 132, 133]

The first approach involves the fabrication of a pre–patterned PCMs on a partial GaAs slab. A single quantum dot is fabricated on a desired position by local oxidation lithography by atomic force microscopy. The last step consists of the re–growth procedure to complete the slab. The second approach is also based on the growth of a QD by LOL–AFM. This QD is grown with respect to a set of pre–patterned alignment marks and ruler defined by etching procedures in a partial slab. The completion of the slab maintain the coordinates of the QD and as a last step, the photonic crystal microcavity will be fabricated on the desired position.

6.2 Contribution

My contributions to this work are:

- Design and implementation of the different strategies
- Design of the photonic crystal microcavities by finite difference time domain
- Fabrication of the photonic crystal microcavities
- Assistance in the optical characterization of the devices

6.3 Publication

6.3.1 Abstract

In this work we show two different procedures of fabrication aiming towards the systematic positioning of single InAs quantum dots (QDs) coupled to a GaAs photonic crystal (PC) microcavity. The two approaches are based on the molecular beam epitaxial (MBE) growth of site-controlled QDs (SCQDs) on pre-patterned structures. The PC microcavity (PCM) is introduced previous or after the growth, on each case. We demonstrate the InAs SCQD nucleation on pre-patterned PCMs and a method to perform the QD nucleation respect to an etched ruler that is used to position the PC structure after growth. For both types of structures, we have carried out microphotoluminescence (μPL) spectroscopy experiments at 80 K and 4 K.

6.3.2 Introduction

A single Quantum Dot (QD) coupled to a photonic cavity mode is the fundamental system for the study of Cavity Quantum Electrodynamics (cQED) phenomena in the solid state approximation.[26] These studies are essential for the development of devices such as single photon emitters and entangled photon pair sources, key elements for quantum information technologies. The successful fabrication of this kind of systems is very challenging due to the simultaneous requirements of spatial matching (the QD has to be placed at the maximum of the photonic cavity mode field) and spectral matching (both the wavelength of the QD emission and of the photonic cavity mode have to be very close) between the QD and the photonic cavity mode. Coupling of single self–assembled QD to a photonic crystal microcavity (PCM) mode has already been demonstrated [134, 8] and promising applications have been proven. Despite these important results, in most cases, the fabrication is based on random QD distributions and it is clear that the fabrication technology of single QD devices is far from being mature and systematic. In this sense, the use of high spatial resolution lithographic techniques for site controlled QD (SCQD) formation [127, 135] is crucial in order to improve the yield of deterministic integration of a coupled QD–cavity mode.[128, 127, 136] In this work we present two strategies for the coupling of InAs QDs to the mode of GaAs–based PCMs. Both strategies are based on the combination of photonic crystal (PC)

fabrication technologies and Molecular Beam Epitaxy (MBE) growth of SCQDs. Local Oxidation by Atomic Force Microscopy (LO-AFM) is the lithographic technique selected to fabricate the pattern for SCQD growth: InAs QDs are formed at specific sites of the GaAs surface defined by the presence of nanoholes formed after desorption of the GaAs oxide points obtained by LO–AFM. The process provides high accuracy in the positioning of the nanostructures and it has been proven that the obtained SCQD has good optical properties and are efficient quantum emitters operating as single photon sources.[135] Electron-beam lithography and Cl-based reactive ion etching (RIE) techniques are employed in the fabrication process for GaAs PCMs. We consider that the technological processes used will allow us to deterministically obtain coupled single QD-cavity systems and deal with new devices.[137]

6.3.3 Design and experimental

The ability of fabricating SCQDs combined with a proper positioning of PCMs brings us the capability for getting single or several QDs coupled to a PCM mode in a deterministic way by two different techniques: either it is possible to locate the QD respect to a pre-patterned structure or the cavity respect to the position of a SCQD.

Fabrication process of Photonic Crystal Microcavities in GaAs

For both techniques we have developed a fabrication procedure to pattern PCMs on GaAs-based materials. A schematic of the process is shown in Figure 6.1. The starting material consists of a thin GaAs layer grown on an $Al_{0.75}Ga_{0.25}$ As sacrificial layer. We use the spin-coating technique for the deposition of a 380 nm thick layer of ZEP–520A resist on the GaAs slab. We have selected ZEP–520A because of its adequate well known properties (high sensitivity, hardness) for the direct transfer of the pattern to the substrate in a single etching step. The pattern is defined in the e-beam writing step. It is provided by a LEO 1455 Scanning Electron Microscope (SEM) with a Laser Interferometric Stage at 30 kV. For such conditions, it is very important to take into account the proximity effect.[40] In order to improve the size homogeneity and the accuracy in the e–beam writing, we have used the Proximity Correction Module NanoPECS integrated in the Raith ELPHY Plus lithography system.[42] After the developing step, which defines

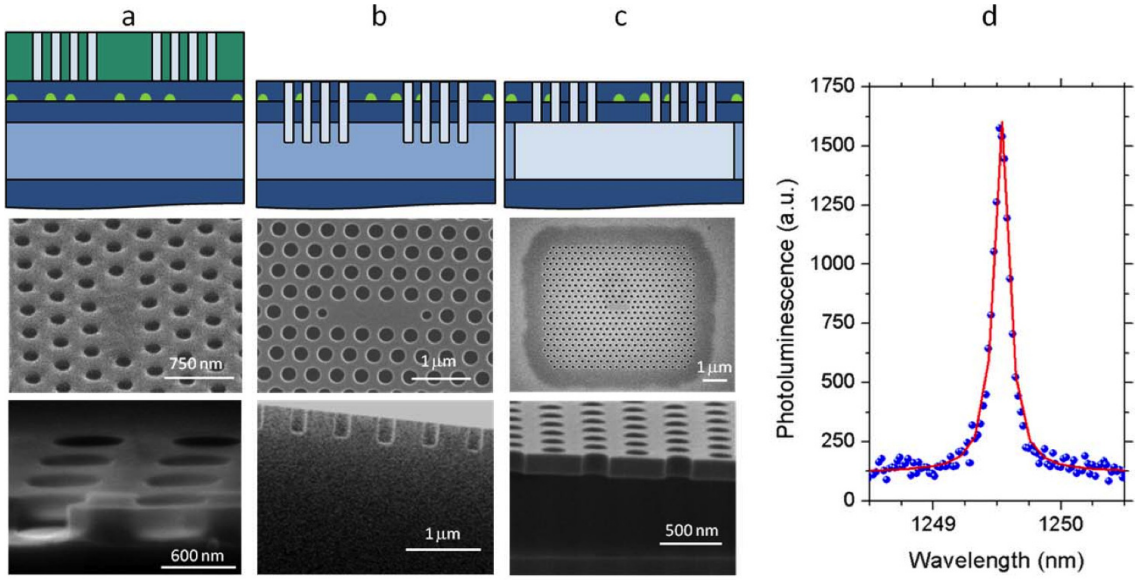

Figure 6.1: **Fabrication procedure of photonic crystal microcavities.** a) Spin coating of ZEP–520A, e–beam lithography and development. b) Cl–based ICP RIE etching with direct transfer to the active slab. c) Membrane release by immersing the sample in HF 1:5. In the middle top view of the structures are presented. In the bottom it is shown the vertical shape of the hole during the process. d) Determination of the Q for an L3-type cavity with a lattice constant $a = 330$ nm and $r/a = 0.28$. Blue dots indicate the measurement and the red line correspond to the Lorentzian fitting. We have obtained $Q = 8970$ for this structure.

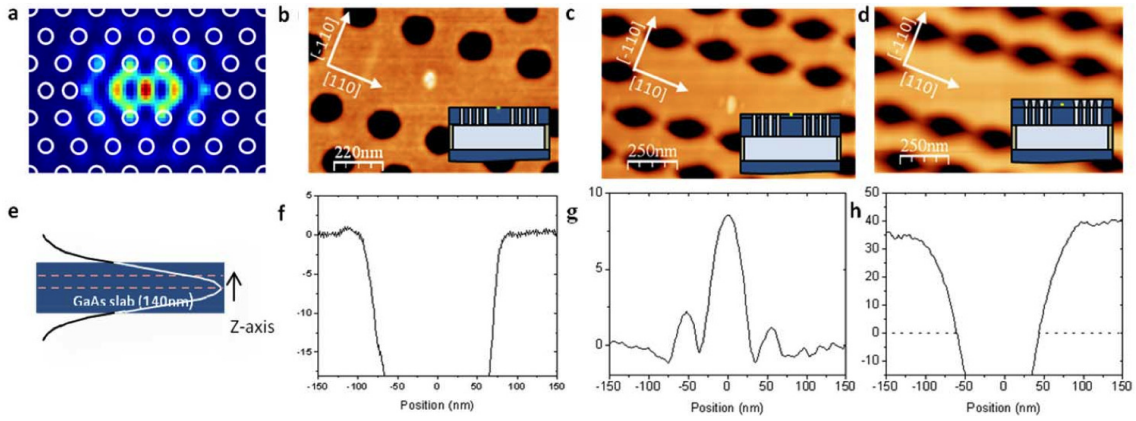

Figure 6.2: **Fabrication procedure of the site–controlled quantum dot over a pre–patterned photonic crystal microcavity.** a) In–plane FDTD (centre of the slab) electric field energy density for an L3–cavity. The position that corresponds to the maximum value (red color) is the target position for the nucleation of the SCQD. We show AFM images that correspond to different steps in the fabrication process: b) Oxide motif fabricated within the PCM by LO–AFM lithography and placed at the target position, c) InAs SCQD at the predefined position within the cavity. d) Complete photonic structure after re–growth. e) Embedded SCQD is placed 20 nm below the surface. FDTD calculations show that this position corresponds to a 64% of the maximum value for the electric field of the guided mode, being the center of the slab the optimum position. It is shown the AFM hole profile f) before and h) after the MBE re–growth. It is also shown g) the AFM profile of the InAs SCQD.

the pattern into the resist, (Figure 6.2a) the sample is post–baked in order to increase the hardness of the resist and the hole homogeneity.[138] Then, we carry out the ICP–RIE plasma etching. We have developed a Cl-based plasma etching in a Oxford ICP–RIE Plasmalab 80, that allows us to transfer the pattern to the active GaAs slab in a single step. This mixture has been used for etching GaAs material in Inductive Coupled Plasma Reactive Ion Etching (ICP-RIE) [139] due to its good properties related with the high anisotropy, smooth sidewalls and low induced defects. We have designed a plasma that consists of a $Cl_2/BCl_3/Ar$ mixture. The optimal conditions we have found for these structures in GaAs slabs are: 1.2 sccm Cl_2, 2.1 sccm BCl_3, 12.1 sccm Ar, 5 sccm He, at low pressure (2.6 mTorr) and low temperature (-11 °C), 300 W ICP power and 20 W RF generator during 90 s, where the flows of the gases are standard cubic centimetre (sccm). The low DC Bias reached and the He-flow in the backside of the sample in order to favour the temperature transfer to the sample, enables a higher selectivity.

After the removal of the remaining resist with UV illumination and remover (Figure 6.1b), a membrane formation is performed by immersing the sample in a 1:5 HF solution (Figure 6.1c). It is important to exceed the slab thickness during the plasma etching in order to favour the entrance of the HF solution through the hole array because it favours the removal of the sacrificial layer underneath the pattern. The last step involves a cleaning process that removes the dust deposited above, below and inside the holes. Following the procedure of reference,[14] we immerse the sample in a KOH solution. It provides structures that are cleaner, and subsequently, with better optical properties. In order to estimate the quality of the structures, we have carried out optical measurements at room temperature and determined the quality factor (Q) of the cavities in a sample containing InAsSb QDs (Figure 6.1d).[36] We excite the QDs within the defect with a continuous wave (c.w.) laser diode (LD) at 785 nm focused with a microscope objective ($NA = 0.5$). We collect the PL through the same objective and focused into a optical fiber connected to a 0.85 m focal length double spectrometer with a cooled InGaAs photodiode array as detector. In these structures we have measured Q-values ranging from 8000 to 10000.

Positioning a QD to a PCM mode

The first approach for the SCQD positioning (Figure 6.1) consists of the fabrication of PCMs on a 105 nm thick GaAs slab. Afterwards, the pre-patterned photonic structures are completed to the target 140 nm slab thickness in a MBE re-growth process with an embedded InAs QD at the desired position.[140] We have fabricated L3–type and H1–type cavities with different lattice constants, $a = 250$, 255 and 260 nm, aiming to cavity modes ranging from 940 nm to 1000 nm. We follow the process above described. After the ICP-RIE process and the removal of the remaining resist, it is crucial for this approximation to proceed with an additional step that provides a clean interface, free of organic contaminants, allowing us to perform a MBE re-growth. It consists of 2-cycles of UV oxidation, H_2SO_4 etching of produced oxide layer and O_2 plasma with another step of H_2SO_4. The next step involves the membrane release as described above. AFM local oxidation is then performed to define the nucleation site of a single SCQD in each structure (Figure 6.2b). Then, the structure is completed in a re-growth MBE procedure. The MBE growth starts with an *insitu* atomic hydrogen treatment ($T_S = 490$ °C, $t = 30$ min) to remove the GaAs surface oxides.

This atomic H treatment provides a flat surface and contributes to remove remaining contaminants on the surface.[141, 142] Prior to InAs deposition, a 15 nm thick GaAs buffer layer is grown by Atomic Layer MBE (ALMBE) [143] at T_S = 450 °C. On top of the GaAs buffer layer, 1.5 ML InAs is deposited at growth rate 0.01 ML/s and T = 490 °C under As_4 beam equivalent pressure (BEP) $P = 2{\times}10^{-6}$ Torr. The growth conditions are suitable for selective InAs nucleation in the predefined site (Figure 6.2c). Selective nucleation is achieved within the defect, even being surrounded by the PC holes, which may also act as InAs drains. Finally, the structure is completed with a 20 nm thick capping layer, grown by ALMBE at T = 450 ° (Figure 6.2d). Low growth temperature is kept during the process in order to reduce the evolution of the pre-patterned PCMs, but a strong change in the shape of the PC holes cannot be avoided. Circular shape evolves into rhombus shape holes. This is likely due to the preferential incorporation of Ga atoms in B-type facets (As-terminated), which intersection with the (001) surface plane is the [110] direction.[140, 144] Despite preliminary Finite Difference Time Domain (FDTD) calculations suggest that the photonic bandgap may be preserved in such structures, we believe that this behaviour can degrade the performance of the fabricated structures. Since this evolution is dependent on the crystallographic directions, a previous orientation of the pattern may reduce the impact on the photonic properties of the structures. We have carried out optical characterization of these devices by confocal microscopy at 77 K. Spectral features have been found in the range of 950 nm to 1200 nm (Figure 6.3a). Measurements outside the PC structures do not reveal any emission in this range (Figure 6.3b). The emission around 860 nm outside the PC structure can be assigned to an InGaAs wetting layer (WL). Further work is needed to clearly identify evidence of a PCM mode or any signature from the SCQD.

Positioning a PCM mode to a SCQD

The second proposed strategy is based on the use of an etched ruler and a set of alignment marks (Figure 6.4) to accurately position a PCM to a SCQD. The starting material consists of 1 μm thick $Al_{0.8}Ga_{0.2}As$ sacrificial layer and 65 nm thick GaAs layer. A set of rulers and their corresponding alignment marks are fabricated in the sample following the procedures above described. We have designed a global reference system that consists of a set of three alignment marks, a ruler and a mark that defines the origin. It is important to fabricate the whole

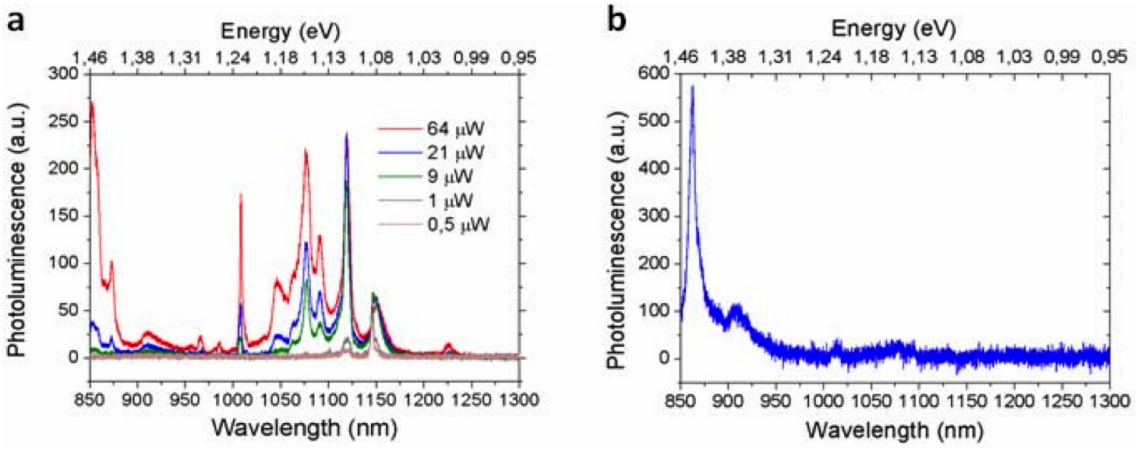

Figure 6.3: **Optical characterization by μ–PL of one of the fabricated structures.** a) PL signal collected from the cavity at different excitation powers and b) outside the entire PC structure.

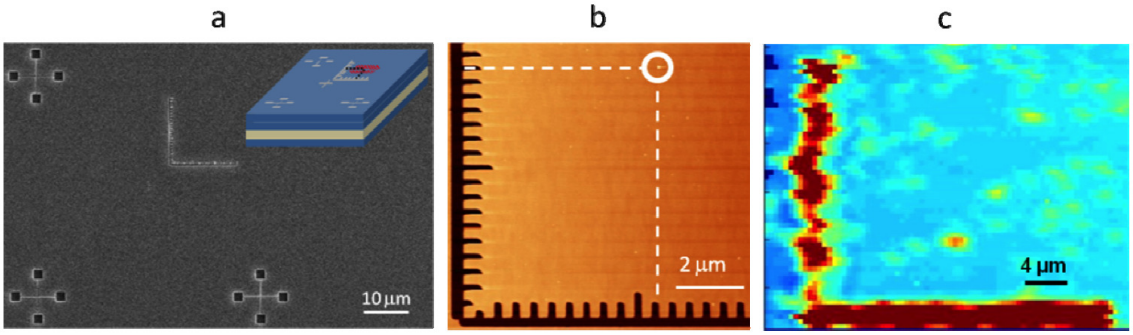

Figure 6.4: **Description of the strategy for positioning.** a) SEM image that shows a global reference system. A set of three alignment marks separated 50 μm each other and 35 μm from the origin. A schematic of the complete process with a PCM positioned respect to the coordinates of the SCQD is shown in the inset. b) We present an AFM image of the region enclosed by the ruler with an oxide dot referred to the ruler coordinates. c) μPL map obtained at 4 K integrating the emission spectrum between 920–980 nm. The ruler axes have a higher QD density.

system in the same writing field during the e-beam exposure. The alignment marks, together with the origin, will be used as a system for the calibration of the beam deflexion during the fabrication of the PCs (inset Figure 6.4a). The ruler is written during the e-beam step. Its arms are 20 μm large (Figure 6.4a), with ticks separated 500 nm (Figure 6.2b). The surface preparation process above described is also performed to allow the epitaxial re-growth. Afterwards, LO-AFM lithography is performed in a specific position within the ruler area. We assign the spatial coordinates to the fabricated oxide respect to the ruler axes. These coordinates will correspond to the InAs SCQD once the re-growth step is completed, as the oxide position defines the InAs nucleation site. The preservation of this reference system during the fabrication process is crucial in this approximation. The MBE re–growth starts with the *i*n situ atomic H–treatment. The structure is then completed with the growth of 15 nm thick GaAs buffer layer, 1.5 ML InAs and 70 nm thick GaAs capping layer. The GaAs layers are grown by ALMBE at T_S = 490 °C and Ga growth rate r_g(Ga) = 0.5 ML/s, while the InAs layer is deposited at r_g(In) = 0.01 ML/s under BEP $P(As_4)$ = 2×10^{-6} Torr. The InAs coverage is below the critical thickness on flat surfaces but it allows the nucleation of InAs inside the nanoholes, thus providing the formation of InAs SCQDs with some given coordinates. The axes of the ruler together with the alignment marks are well preserved after the MBE re–growth. Therefore, they can be used as a reference system for the later fabrication of PCMs. The proper calibration and alignment of both SEM and AFM coordinate systems allow us to subsequent fabrication of PCMs in the desired positions, in which the maximum of the electric field mode profile (Figure 6.2a) matches the position of the SCQD. Once we have determined the optical properties of the SCQD by μ–PL, the PCM mode can be designed to match the emission wavelength of the embedded QD. The final spatial accuracy of the positioning is estimated to be around 50 nm. We have carried out preliminaryμ–PL measurements at 4 K on these systems after completing the re–grown GaAs slab. We have noticed a large amount of InAs QDs nucleated next to the ruler axes. The density decreases rapidly 2 μm beyond the edges (Figure 6.4c). Far from this region, in the area enclosed by the ruler, still a small density of QDs (around 0.1 QD/μm^2) was detected. Not clear SCQD signal has been detected from the position predefined by LO–AFM. This may be due to two effects: first, the nucleation of QDs in non patterned areas that makes difficult the identification of the SCQD; second, the absolute accuracy ($\pm$1.5 μm)

when positioning our diffraction limited spot (∼1 μm diameter) with respect to the etched ruler origin. An improvement in the selective nucleation process and our positioning method will be necessary in further research.

6.3.4 Conclusions

We have presented two fabrication strategies towards the achievement of coupled SCQD-PCM mode systems. Both are based on PC structure fabrication on GaAs and MBE growth of SCQDs and pre–patterned structures. We have demonstrated selective InAs nucleation on pre–patterned PC structures, but the epitaxial re–growth process on the pre–patterned PCMs leads to a strong evolution of the hole shape that may degrade their performance. In a different fabrication strategy, the use of a set of reference system consisting of a pre-patterned ruler and alignment marks provides a method that may allow a systematic fabrication of systems to investigate the coupling of a single or several QDs to a PCM mode.

6.4 On–going work

The demonstration of the operation of QDs by LOL–AFM and the development of a fabrication procedure of PCMs allow us to construct the presented strategies towards the deterministic PCM–QD coupling. The next step with respect to the first approach involving the re–grown cavities is to test the capabilities of those cavities. Regarding the strategy of the etched ruler, we should repeat and reproduce the achievment of a "clean" sample with a clear identification of the quantum dots obtained by LOL–AFM.

Chapter 7

High quality factor GaAs–based photonic crystal microcavities by epitaxial re–growth

I. Prieto, J. Herranz, L. Wewior, Y. González, B. Alén, L. González, and P. A. Postigo

Opt. Express **21** (25), 31615 (2013)

IMM–Instituto de Microelectrónica de Madrid (CNM–CSIC), Isaac Newton 8, PTM, E–28760 Tres Cantos, Madrid, Spain

7.1 Context & motivation

A method to achive deterministic coupling between a single quantum dot (QD) and a photonic crystal microcavity mode is presented. So far, different methods for the relative positioning between QDs and cavities have been demonstrated. In particular, positioning of cavities over selected self–assembled QDs was presented,[8] as well as the positioning of cavities over positioned nanostructures in the wafer [145, 127]. An alternative method is to fabricate a photonic crystal microcavity in a partially grown slab (with a thickness below the optimum in terms of optical confinement). After that, the growth of an isolated nanostructure is performed in the desired position and the fabrication procedure ends up with the slab thickness completion in a re–growth process. Finally, we have analized the optical properties of those, named, re–grown cavities.

7.2 Contribution

My contributions to this work are:

- Design of the epitaxial material,
- Fabrication of the devices,
- Design of the photonic crystal microcavities,
- Assistance on the optical characterization of the devices,
- Analysis and interpretation of the results using finite difference time domain simulations,
- Writing of the results.

7.3 Publication

7.3.1 Abstract

We investigate L7 photonic crystal microcavities (PCMs) fabricated by epitaxial re–growth of GaAs pre–patterned substrates, containing InAs quantum dots. The resulting PCMs show hexagonal shaped nano–holes due to the development of

preferential crystallographic facets during the re–growth step. Through a careful control of the fabrication processes, we demonstrate that the photonic modes are preserved throughout the process. The quality factor (Q) of the photonic modes in the re–grown PCMs strongly depends on the relative orientation between photonic lattice and crystallographic directions. The optical modes of the re–grown PCMs preserve the linear polarization and, for the most favorable orientation, a 36% of the Q measured in PCMs fabricated by the conventional procedure is observed, exhibiting values up to 6000. The results aim to the future integration of site–controlled QDs with high–Q PCMs for quantum photonics and quantum integrated circuits.

7.3.2 Introduction

Photonic crystal microcavities (PCMs) with embedded quantum dots (QDs) have been shown as excellent test bed systems for experiments in the field of cavity quantum electrodynamics (c–QED)[8, 28] that may open doors to efficient quantum photonic devices. Single quantum dots embedded in a PCM become efficient quantum emitters which might be used for the generation of single–photons,[132, 146, 147] entangled photon pairs,[148] ultra–low threshold lasing,[28] polariton lasing[28, 119] or to explore new strong coupling phenomena.[149, 150, 151] Most c–QED applications require of a large optical quality factor (Q), a small electromagnetic mode volume (V_{eff}), and a large coupling between the QD emission and the PCM mode.[152] Therefore, an accurate positioning of the QD within the PCM while maintaining a high Q/V_{eff} ratio is a critical requirement not easily attainable with self–assembled QD growth methods.[153] Several procedures have been proposed for the fabrication of site–controlled QDs[154] coupled to PCMs.[25, 137] Among them, local oxidation lithography by atomic force microscopy (LOL–AFM) is a powerful technique for the patterning of GaAs substrates which is compatible with the epitaxial growth of site–controlled InAs QDs. LOL–AFM allows the positioning of high quality QDs in any place of a wafer in a deterministic way,[135] and therefore is very promising for quantum photonic applications.[25, 137] However, since the QD has to be embedded in the PCM slab underneath the surface, the development of a special re–growth procedure is needed to complete the photonic structure after the LOL–AFM step. The epitaxial re–growth of photonic structures[155] has been realized in distributed feedback (DFB) lasers and photonic crystal lasers by metal–organic chemical va-

por deposition (MOCVD)[156, 157] and photonic crystal surface emitting lasers (PCSELs) by metal–organic vapor phase epitaxy (MOVPE).[158] More recently, PCMs have been fabricated by re–growth processes over patterned GaN wafers by nitride–MOCVD[159, 160] showing photonic modes with Q up to 2400 at a wavelength of 383 nm.[161] In addition, cavity modes with $Q = 1800$ at 426 nm have been shown in PCMs obtained by re–growth of pre–patterned L3–PCMs on slabs of AlN material with embedded GaN/AlN QDs.[162] In this work we demonstrate that PCMs fabricated by epitaxial re–growth of a previously patterned GaAs substrate exhibit optical modes with Q factors comparable to those obtained by standard lithography and etching procedures. The studied PCMs contain self–assembled InAs QDs with emission wavelengths in the range 890–1000 nm and therefore, the developed method paves the way for the use of one or several LOL–AFM deterministically site–controlled QDs integrated with PCMs with emission in the 980 nm telecom window. We have modeled the optical properties of the re–grown PCMs, by means of finite difference time domain (FDTD) simulations, to evaluate the impact of the re–growth procedure, obtaining an explanation for the high Q–values found.

7.3.3 Design and fabrication

We have fabricated PCMs of the L7–type, which consists of a set of seven missing holes along the ΓK direction of an array of circular holes with triangular symmetry.[60, 20] The separation of the holes (with radius r) is given by the lattice constant a, which corresponds to the distance between two neighboring holes along the ΓK direction. For such a triangular lattice, the air–filling factor (FF) is given by the ratio of the volume of one hole and that of a slab unit cell, $FF =$. The L7–PCM presents two important advantages: on one side, its elongated shape is useful for the positioning of nanostructures like quantum wires[76, 21] or the use of several QDs sharing an optical mode.[137] On the other side, it provides a good Q/V_{eff} ratio without the need of tuning the holes that surround the cavity, which increases its robustness to fabrication imperfections. The L7–PCMs have been fabricated in samples from two different wafers, named hereafter, W–I and W–II (Figure 7.1). Both W–I and W–II wafers are grown by molecular beam epitaxy (MBE) and consist of a GaAs based active slab on top of an $Al_{0.70}Ga_{0.30}As$ sacrificial layer 1 μm thick underneath. A high–density self–assembled InAs QDs (SAQD) was grown 70 nm over the $Al_{0.70}Ga_{0.30}As$/GaAs

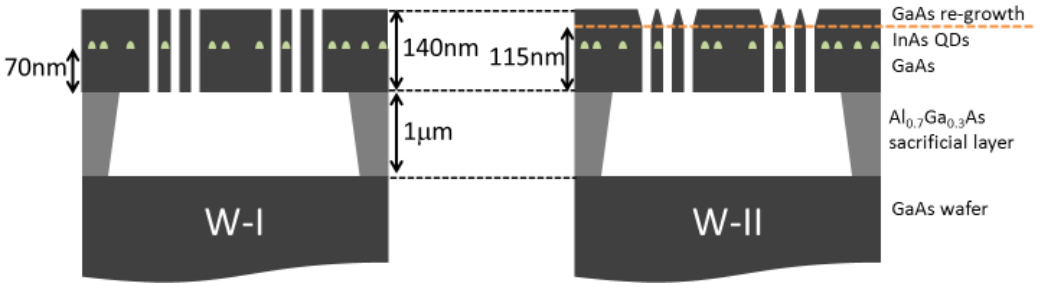

Figure 7.1: **Schematics of the epitaxial structure and the resulting structures.** Schematics of the standard (left) and re–grown (right) photonic crystal microcavities (PCMs) fabricated for this work.

interface in both W–I and W–II. The main difference between W–I and W–II is the active GaAs slab thickness, 140 nm for W–I and 115 nm for W–II. For the fabrication of the PCMs in the first wafer (W–I) we have used a standard procedure, based on electron beam lithography (EBL) and plasma ion etching. On top of the W–I wafer, a layer of 80 nm of SiO_x was deposited by plasma enhanced chemical vapor deposition (PECVD) at 300 oC as a hard mask. A 360 nm thick layer of ZEP–520A was spun coated over the SiO_x for the EBL patterning (30 kV). After EBL and a developing process, the patterns were transferred to the SiO_x layer by CHF_3/N_2 reactive ion beam etching (RIBE) that provides excellent opening of the nanoholes in the SiO_x.[20] Reactive ion etching (ICP–RIE) with a BCl_3:N_2 mixture was used to transfer the pattern to the GaAs active slab, which results in vertical and smooth holes.[45, 16] Finally, the photonic crystal membrane is released by diluted HF wet etching of the $Al_{0.70}Ga_{0.30}As$ sacrificial layer under the structures. We will refer to those PCMs as standard L7. In the W–II wafer, L7–PCMs were fabricated using the same procedure as in W–I followed by an epitaxial re–growth step to complete the slab thickness to 140 nm. After the membrane release and prior to the re–growth step, a careful cleaning process is performed in order to remove resist residuals and contaminants from the previous fabrication process. Once inside the MBE chamber, the native oxide is removed by exposure of the GaAs surface to atomic H that preserves the flatness of the surface [163] between the holes. For that, atomic hydrogen is supplied at substrate temperature of $T_S = 450$ °C during 30 minutes. The re–growth continues with the deposition of a GaAs layer by atomic layer molecular beam epitaxy (ALMBE) [143] at $T_S = 450$ °C to complete the 70 nm of GaAs over the SAQD layer. Two sets of L7–PCMs were fabricated in both W–I and W–II with the ΓK direction

of the PCM either perpendicular (L7$\perp$) or parallel (L7$\parallel$) to the GaAs [110] crystallographic direction. Four lattice constants (a = 250, 260, 270 and 280 nm) for the PCMs were fabricated to cover the luminescence of the QD emitters. For a given a, different r/a–values ranging 0.26–0.33 were practiced for a fine–tuning of the PCM optical modes with the QD emission. Figure 7.2 shows images taken by scanning electron microscopy (SEM) on the PCMs in W–I [Figures 7.2(a–b)] and in W–II [Figures 7.2(c–f)]. The fabrication process in W–I results in holes with circular shape, vertical and smooth.[45, 16] In W–II, the re–growth step induces a change from the initial circular shape of the holes towards an elongated hexagonal shape, due to the development of new crystallographic facets.[164] The long axis of the hexagon is aligned along the [110] crystalline direction. This direction corresponds to the intersection of B–type facets (As terminated) with the (001) surface plane; the short axis of the hexagon is aligned along [1$\bar{1}$0] that corresponds to the intersection of A–type facets (Ga terminated) with the (001) surface plane. A lateral flux of Ga atoms towards B–type facets and away from A–type facets during the re–growth step can explain the observed hexagonal shape. Lateral flux of Ga atoms has been previously reported [164, 165] and a similar evolution has been described during the initial overgrowth of nanoholes fabricated by EBL and dry etching [166] or by LOL–AFM and HF selective oxide etching on GaAs substrates.[140] The evolution of the shape of the holes may affect the photonic properties of the PCMs, so our task is to determine the influence of this effect in the photonic performance of the PCMs, verifying if photonic modes are still present and, in that case, evaluating the optical quality of the PCMs through the measurement of their Q.

7.3.4 Optical characterization

We have performed optical characterization by confocal microscopy at 4 K to measure the micro–photoluminescence (μ–PL) emitted from the PCMs. The excitation laser CW light at 785 nm was delivered through a single mode optical fiber to the microscope and focused onto the PCM within a diffraction limited optical spot. The light emitted by the sample was collected through a different single mode optical fiber, dispersed by a 750 mm focal length spectrometer and detected with a cooled Silicon Charge Coupled Device. The spectral linewidth of the resonances ($\Delta\lambda$) determines the Q–values ($Q = \lambda/\Delta\lambda$) of the photonic mode at the wavelength λ. We focus in the Q of the fundamental mode (FM)

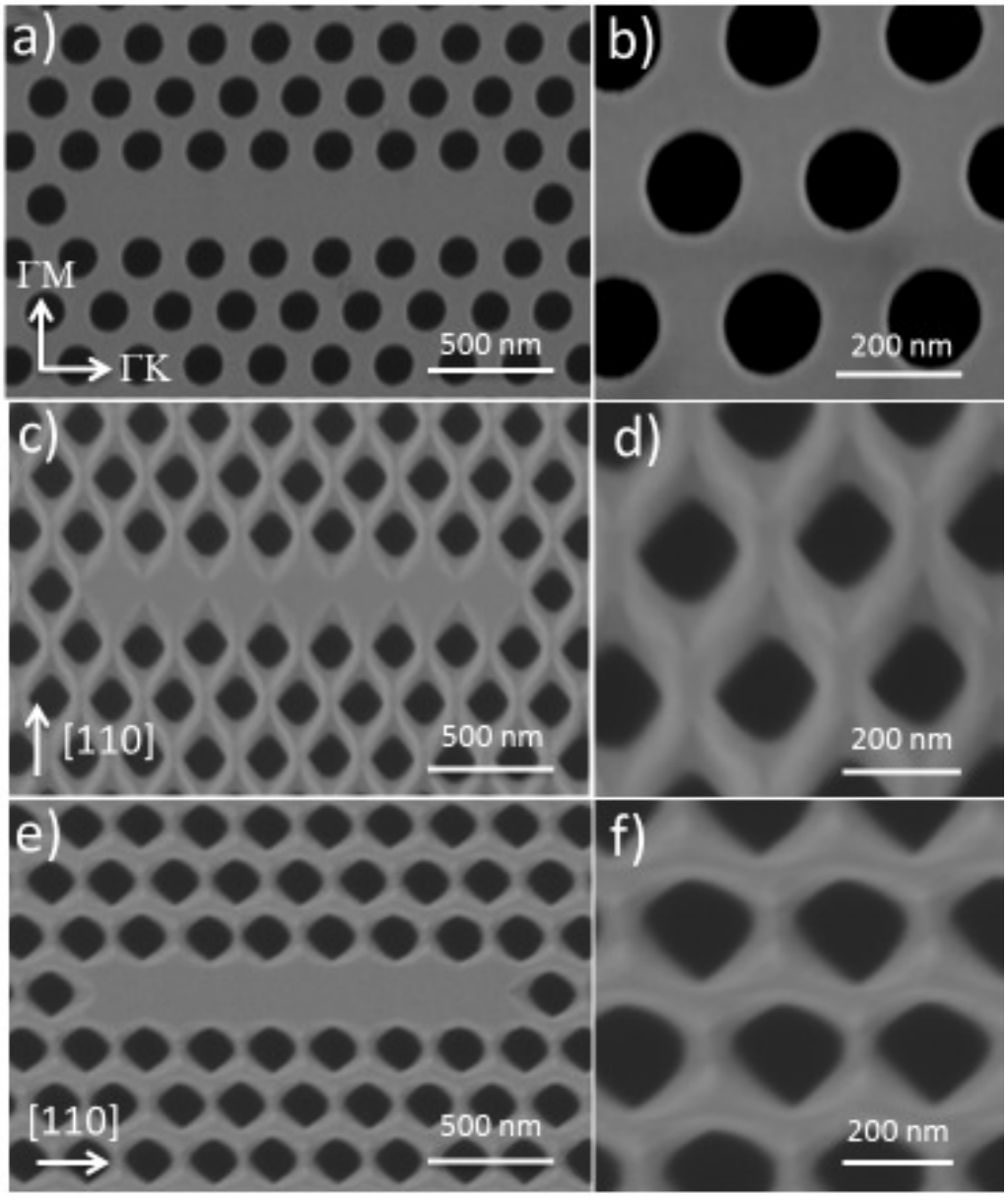

Figure 7.2: **Scanning electron microscopy (SEM) images of fabricated set of standard L7 and re–grown L7 photonic crystal microcavities (PCMs).** (a) SEM image of a standard L7–PCM, (b) close–SEM images of a L7$\perp$ PCM; (e–f) SEM images of a L7$\parallel$ PCM.

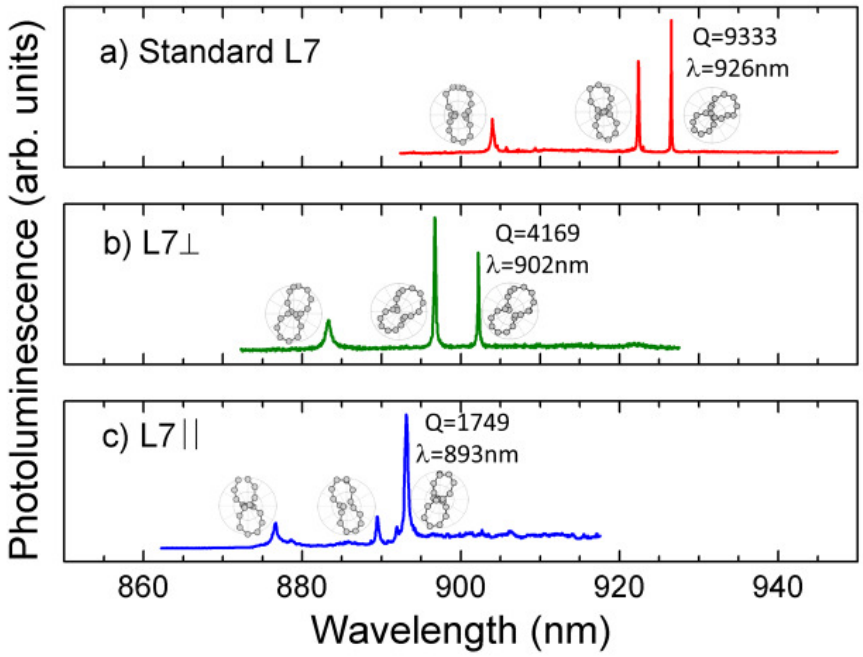

Figure 7.3: **Micro–photoluminescence (μ–PL) spectra corresponding to a set of L7 photonic crystal microcavities (PCMs).** (a) standard L7, (b) L7⊥ and (c) L7‖. Quality factor (Q) and spectral position (λ) of the fundamental mode (FM) are presented. Insets show the polarization diagrams for each of the observed L7–PCM modes.

since it provides the best Q/V_{eff} ratio.[60] Figure 3 shows the PL spectra of a representative set of L7–PCMs, one corresponding to a standard L7 in W–I [Figure 7.3(a)] and the others to the re–grown L7–PCMs, i.e. L7⊥ [Figure 7.3(b)] and L7‖ [Figure 7.3(c)] in W–II. Both the L7⊥ and L7‖ re–grown PCMs present spectral features that resemble very well those observed in standard L7. This is already indicative of the good optical performance of the re–grown PCMs, so we will refer as photonic modes the observed features in the re–grown cavities. The results obtained from a statistical study of the spectral position of the observed modes in every set of PCMs, show a blueshift of 26 ± 6 nm for the FM of the L7⊥ and of 45 ± 13 nm in the L7‖ configurations with respect to the standard L7. We attribute the observed blueshifts to the two following reasons, that will be supported by simulations: *i)* the cleaning process previous to the epitaxial re–growth that results in an isotropic removal of the GaAs oxide, which produces a slight enlargement of the radius of the holes and a decrease of the slab thickness[167]

and *ii)* the evolution of the circular shape of the holes to hexagonal during the re–growth step, which also enlarges the effective size of the holes. The standard L7–PCMs exhibit Q–values for the FM ranging from 5000 to 11000. In particular, Figure 7.3(a) shows the photonic structure of a standard L7–PCM with $Q = 9333$. Figures 3(b) and 3(c) show $Q = 4169$ for L7$\perp$ and $Q = 1749$ for L7$\parallel$. The statistical analysis shows that in the re–grown L7–PCMs the Q is preserved a 36% for L7$\perp$ and a 15% for L7$\parallel$ with respect to the standard L7–PCMs. It is found that the optical performance observed for the re–grown PCMs depends on the relative orientation between the crystallographic and the photonic crystal directions. This result could be explained as follows: in the L7$\perp$, the distance between first neighboring holes along [110] is 3 times longer than in L7$\parallel$. Since growth leads to nanoholes elongated along [110] direction, neighboring holes first collapse when ΓK is aligned along the [110] direction (L7$\parallel$). Therefore, a more robust optical performance (i.e., higher Q) is expected for L7$\perp$ than for L7$\parallel$. To further confirm the photonic mode structure of the PL spectra, we have analyzed the polarization properties of the observed resonances of the PCMs in W–I and W–II. It is well known that the Ln–type PCMs should present optical modes linearly polarized.[60, 20] The insets in Figure 7.3 show the polarization polar plots for the first three PCM modes. These plots clearly show that the first three modes present linear polarization for both standard [Figure 7.3(a)] and re–grown L7–PCMs [Figure 7.3(b) and 3(c)]. Similar behavior results from the analysis of every set of PCMs, confirming the photonic modal structure of re–grown PCMs.

7.3.5 Numerical calculations

In order to evaluate the impact of the change of the hole shape on the optical properties, we have performed three dimensional FDTD (3D–FDTD) simulations[39] of the re–grown PCMs. We focus on the determination of the Q and λ of the FM of the standard and the re–grown L7–PCMs. We consider a dipole source with a narrow bandwidth for the excitation of the FM and a point monitor located in the antinode of the FM profile registers the time evolution of the mode. The Fast Fourier Transform (FFT) of the time evolution of the electric field amplitude determines the spectral position of the mode (λ). The Q is obtained by analyzing the signal decay with the time. Further information related to FDTD simulations can be found in Ref. [68]. We have modeled the re–grown hole as a vertical circular cylinder with radius r_b on the bottom part that corresponds

to the pre–pattern. The top part of the hole affected by the re–growth step is modeled as a truncated cone with a circular bottom base, with radius r_b, that evolves to an elliptical shape in the surface, with short and long axes, r_e and r_E, respectively [Figure 7.4(a) inset]. We have taken the r_e and r_E values from AFM measurements and the r_b value from SEM images (circular base of standard L7–PCMs). In general, a reduction of the symmetry of the point lattice may affect the photonic performance of PCMs.[168, 169, 170] To evaluate the impact of the loss of symmetry due to the relative orientation of the holes with the crystallographic directions we calculate the Q–values of the re–grown PCMs while changing the angle (θ) between ΓK and the [110] crystallographic direction. Figure 7.4(a) shows the variation of Q with θ for a PCM with air filling factor, $FF = 0.31$. Compared to those measured in the experiments, the values of Q obtained from simulations are larger mainly due to surface scattering processes, which for simplicity are not considered;[138] therefore, those results are not intended to match the measured quantities, but the analysis of the simulations is key to understand the experimental results. From the simulations, we obtain the maximum Q–values for $\theta = 90°$ (L7⊥) and for $\theta = 0$ (L7∥). Extended calculations for different FF–values (not shown) reveal that $\theta = 0$ and $\theta = 90°$ are the most robust configurations (i.e., higher Q–values). Figure 7.4(b) shows the evolution of Q with the FF for the two optimum orientations ($\theta = 0, 90°$) and for the standard L7. We obtain a similar trend for the three types of PCMs. Figure 7.4(b) shows that the main impact of the change in the hole shape is a slight decrease of Q for FF below 0.35; especially in the case of L7⊥, Q–values are largely preserved for small FF–values. Therefore, the L7⊥ configuration is expected to be more robust to the evolution of the hole shape during the re–growth step, as our experiments had shown (Figure 7.3). Figure 7.4(c) shows the calculated spectral positions of the FMs for different r/a–values. For the re–grown PCMs we have taken into account the decrease in the slab thickness and the enlargement of the radius r_b due to the cleaning process. As r/a increases, the modes of the standard L7–PCMs experience a blueshift. The same trend is obtained for the re–grown (both L7⊥ and L7∥) PCMs. The relative blueshifts between the standard and re–grown PCMs are within $20 - -30$ nm for the entire considered spectral window ($910 - -1020$ nm) in good agreement with the experimental values.

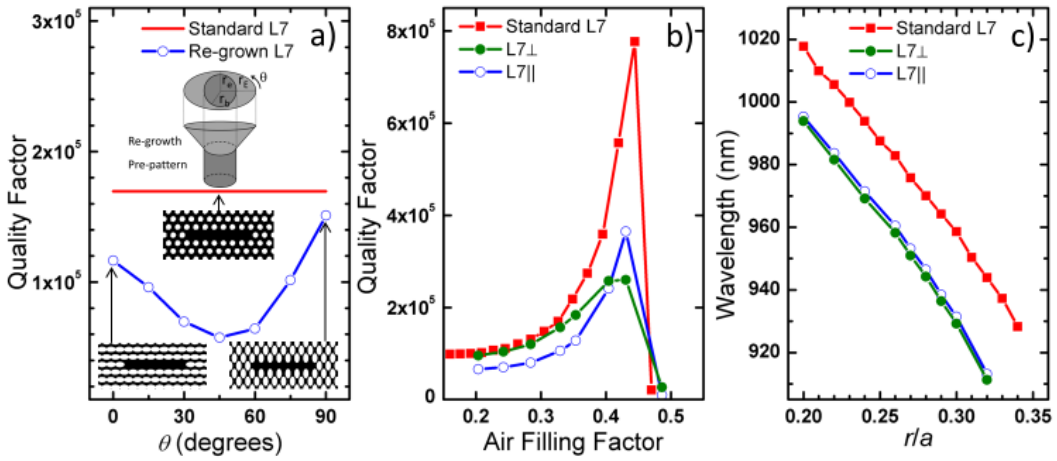

Figure 7.4: **Finite difference time domain (FDTD) simulations of standard and re–grown L7–photonic crystal microcavities (PCMs).** (a) variation of the quality factor (Q) of the fundamental mode (FM) for the standard L7 with an air filling factor, $FF = 0.31$ and for the re–grown PCMs defined by the angle (θ) between ΓK and the [110] crystallographic direction; the insets describe the model for the holes after the re–growth step and the planar views of the PCMs for $\theta = 0$, 45°, 90° and a schematics of the model for the hole shape; (b) variation of Q with FF for standard L7, L7|| ($\theta = 0$) and L7⊥ ($\theta = 90°$); (c) evolution of the spectral positions of the FM of the standard and re–grown PCMs for different values of r/a where r is the hole radius for standard PCMs and the starting hole radius for the re–grown PCMs. Solid lines represent a guide to the eye.

7.3.6 Conclusions

In summary, we have fabricated GaAs–based L7–PCMs using nano–patterned photonic crystal templates and epitaxial re–growth. The circular shape of the holes in standard L7–PCMs evolves to a hexagonal shape in the re–grown L7–PCMs. Optical characterization performed in standard and re–grown L7–PCM shows that the mode photonic structure is preserved after the re–growth step including its linear polarization. A blueshift for the fundamental mode in the re–grown structures with respect to the standard PCM has been measured and attributed to a larger effective FF. The fundamental mode of re–grown L7–PCMs present high Q–values (up to 6000) and in average maintains a 36% of its Q for L7$\perp$ PCMs and a 15% for L7$\parallel$ PCMs with respect to those in standard L7–PCMs. FDTD simulations predict that Q–values can be similar to standard cavities for a broad range of r/a values and show a better performance for re–grown PCMs with ΓK perpendicular to [110] in agreement with experiments. Overall, our result supports the use of epitaxial re–growth methods to obtain PCMs coupled to site controlled QDs.

7.4 On–going work

The demonstration of the high–Q exhibited by the re–grown cavities established the re–growth process as a rout towards the deterministic coupling between a single quantum dot and a microcavity mode. In the work presented we used epitaxial material containing self–assembled quantum dots to demonstrate the concept. The next step is to repeat the procedure on partial slabs with no active region, and fabricate the cavities as a pre–pattern. In a subsequent step, a single InAs quantum dot will be grown on the desired position by local oxidation lithography by atomic force microscopy (LOL–AFM) and molecular beam epitaxial re–growth. The expected result will be an embedded single quantum dot in the desired position within the cavity defect will be obtained

Chapter 8

Towards positioning a photonic crystal microcavity with respect to a single quantum dot

I. Prieto, D. Fuster, L. Wewior, B. Alén, Y. González, C. Robles, L. González, P. A. Postigo

Not published

IMM–Instituto de Microelectrónica de Madrid (CNM–CSIC), Isaac Newton 8, PTM, Tres Cantos, Madrid E-28760, Spain

8.1 Context & motivation

It is very challenging to realize systems that present a deterministic coupling between a single quantum dot and a photonic crystal microcavity in either the weak or the strong coupling regime. Both spatial and spectral matching are required to achieve an ultimate performance on the coupling of a single QD with a cavity mode. In the pursue of such a goal, some authors adopted a statistical alternative [26, 153, 171, 28, 172, 173] of the problem and fabricated hundreds of cavities aiming to reach at least one of them presenting such features. More elegant approaches were based on the fabrication of photonic crystal microcavities on specific locations given by those of the embedded nanostructures.[134, 8, 145, 127, 128, 21] An intermediate solution, involves the use of self–asembled QDs, with better performance, so far, than those fabricated in specific positions. For those systems, it is necessary to mark the spatial position with respect an absolute position in the wafer. To this aim, we have developed a procedure towards the fabrication of a photonic crystal microcavity in a specific position matched to a certain wavelength. We adopted the growth of the QDs through the droplet epitaxy technique in which a self–assembled nanohole template is obtained by Ga–droplet epitaxy.[174] The single QD is preferentially nucleated in those nano–holes and their location is marked through the resulting mound feature on the surface after capping. After a careful characterization of the QD optical properties, we can fabricate the adequated photonic crystal microcavity in the precise location given by the QD. In this chapter we present an approach towards the realization of such a system, together with an exposition of the different strategies adopted by other groups.

8.2 Contribution

My contributions to this work are:

- Design of the epitaxial structure,
- Design of the cavities by finite difference time domain,
- Development of the cavity fabrication procedure,
- Implementation of a procedure for positioning the cavities,

- Partial contribution on the optimization of the geometry, size, disposition and material composition of the metallic marks to obtain an accurate positioning of the PCM,
- Development of a method to fine–tune the QD–cavity resonances by KOH chemical etching, and
- Assistance in the optical characterization of the PCMs.

8.3 Report

8.3.1 Abstract

Here we present an strategy towards the realization of a photonic crystal microcavity that hosts a single quantum dot (QD) located in the maximum of the photonic crystal microcavity (PCM) mode. L7–PCMs were fabricated on a thin GaAs–slab embedding a single layer of low density InAs QDs grown on self–assembled nanohole template obtained by Ga–droplet epitaxy. A resulting mound feature on the surface after the growth of a GaAs capping layer is used to mark the location of a single embedded QD. A specific methodology involving the use of metallic marks and a metallic ruler as a reference, in together with atomic force microscopy and electron beam lithography is proposed to fabricate PCMs on specific positions. The method allows the optical characterization of a selected QD to determine its optical properties both before and after the fabrication of the photonic crysal microcavity, thus providing the possibility of study Purcell effect among other cavity quantum electrodynamics phenomena.

8.3.2 Introduction

The solid state approach to the cavity quantum electrodynamics stems from the fabrication of photonic cavities with high–quality factor (high–Q) and low–effective mode volume (low–V_{eff}) embedding a localized quantum emitter in those positions where the cavity mode is maximum. To achieve such a system, several approaches have been proposed to date. Traditionally, the fabrication of a large amount of cavities in a wafer with self–assembled QDs, spectrally tuned to the fundamental state of the ensemble were performed claiming for any of those systems to present both spatial and spectral matching.[26, 175, 153, 171, 28, 173, 172]

Several technological applications arose from the field of c–QED in the solid–state. Those often require the capability to fabricate those systems in specific positions in a wafer. Therefore, it is necessary to produce a system consisting of a photonic cavity embedding a quantum nanostructure in a deterministic way. Several strategies were proposed, each of them involving either the positioning of a cavity with respect to a nanostructure,[139, 176, 128] viceversa [177] or both the cavity and the nanostructure in an absolute position in a wafer.[145, 127, 178]

In this work we present an alternative that involves the accurate positioning of a GaAs–based photonic crystal microcavity with respect to a single self–assembled InAs QD. The method involves the fabrication of metallic nano–marks combined with a metallic a nano–ruler for alignment and purposes and is fundamented on the small mound feature that appears on the surface just above each QD on the surface. The QDs are obtained by growing InAs on a self–assembled GaAs nano–hole template fabricated by droplet epitaxy. In this way, each mound feature indicates the position where an embedded QD is hosted.

8.3.3 Starting material: droplet epitaxy

The starting material consists of a GaAs/AlGaAs heterostructure that hosts InAs QDs to operate in the 980 nm–spectral–window. Both the emission properties of the QDs and the properties of the photonic crystal microcavity to be fabricated have been considered for the design of the epitaxial structure. Figure 8.1a shows the photoluminescence (PL) spectrum of the active region. A schematic drawing of the grown structure is presented in Figure 8.1b. $Al_{0.75}Ga_{0.25}As$ layer 1 μm thick is grown over a GaAs substrate. On top of that, a thin GaAs slab (140 nm thick) is grown. A single layer of InAs QDs is grown on the mid–slab to optimize the spatial matching of the QDs with the cavity modes. The QDs were grown by droplet epitaxy.[179] As a result of this technique in combination with a specific growth procedure for the capping layer, a mound feature is released on top of each nanostructure. An atomic force microscopy image of those mounds is presented in Figure 8.1c, from which we estimate an averaged density of QDs of 2 μm^{-2} throughout the wafer. A detail of a single mound is presented in Figure 8.1d to determine its dimensions.[I]

The growth by droplet epitaxy consists of the GaAs surface etching by metallic

[I] PL characterization of the QD ensemble and AFM characterization to get the density of QDs and the morphology of the mound features were performed by Dr. David Fuster.

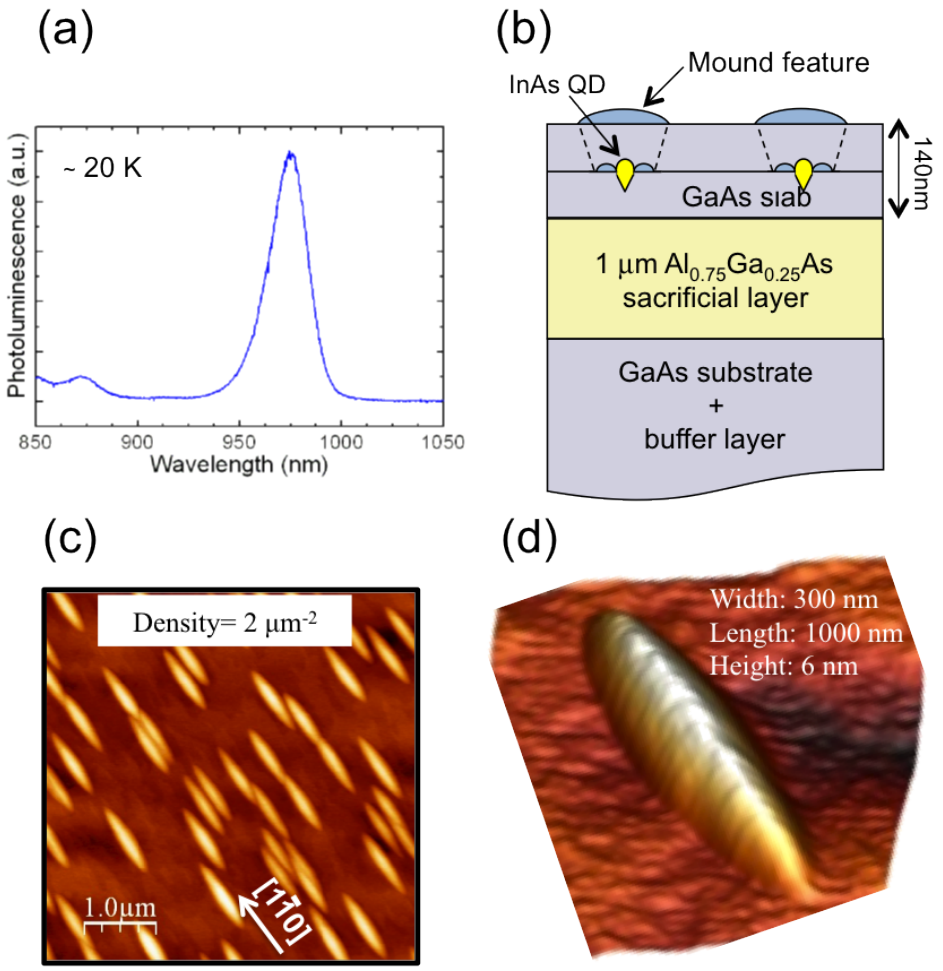

Figure 8.1: **Description of the epitaxial material.** a) Photoluminescence spectrum at low temperature of the InAs QDs showing optical emission in the 980 nm window. b) Schematics of the epitaxial material. c) Atomic force microscopy (AFM) image of the surface of the wafer, showing the mound features elongated along [1$\bar{1}$0]. d) AFM measurement showing a detail of the mound feature.

Ga droplets, thus leading to the formation of self–assembled nano–hole templates. A selective InAs nucleation is achieved on those specific locations. Growth conditions to achieve single quantum dot nucleation on the resulting hole from the droplet epitaxy technique were employed.[179] A single layer of low density InAs quantum dots (2 μm^{-2}) was grown by this method on a 140 nm thick GaAs–slab.

8.3.4 Metallic ruler and alignment marks

To analyse the spatial distribution of the QDs, we characterized the spatial mound distribution by AFM (Figure 8.1c). The QD over which the PCM will be fabricated is chosen by means of spatial isolation of its corresponding mound. To have a reference system for the posterior fabrication of the PCMs, we performed 25–sets of Au–marks and a Au–ruler (Figure 8.2a). The fabrication procedure of the reference system consists of the pattern definition by electron beam lithography (EBL) on a 200 nm thick PMMA–A4. An evaporation of Cr/Au (5/35 nm) converts the pattern into metallic marks and rulers after the lift–off process. Figure 8.2b shows a SEM image with a single set of the alignment marks and the ruler. Each of those sets of marks and ruler is necessary to fabricate the PCM on a specific position relative to the previously selected QD. Figure 8.2c presents the characteristics of the metallic ruler. It consists of two arms enclosing a region 20×20 μm^2 large. Each arm contains small ticks separated 500 nm; larger ticks every 5 μm. Those ticks are important to evaluate the correspondence between the AFM characterization, that provides a set of coordinates of the target QD, and the coordinates of the e–beam, which are used to fabricate the cavities in the desired position.

8.3.5 Optical characterization of an isolated QD: Ti–mask

Once a target QD was chosen by means of spatial isolation in each of the systems, we performed an optical characterization through optical confocal microscopy.[II] To assist the optical characterization, we have fabricated a Ti–square mask with an opened window, surrounding the target QD. The Ti–window (Figure 8.2d) was fabricated following an analogous procedure as that for the Au–marks and the Au–ruler. The choice of Ti as a metal for this marks is due to its easily removal

[II]The presented data about the optical characterization by confocal microscopy was performed by Lukasz Wewior and Dr. Benito Alén.

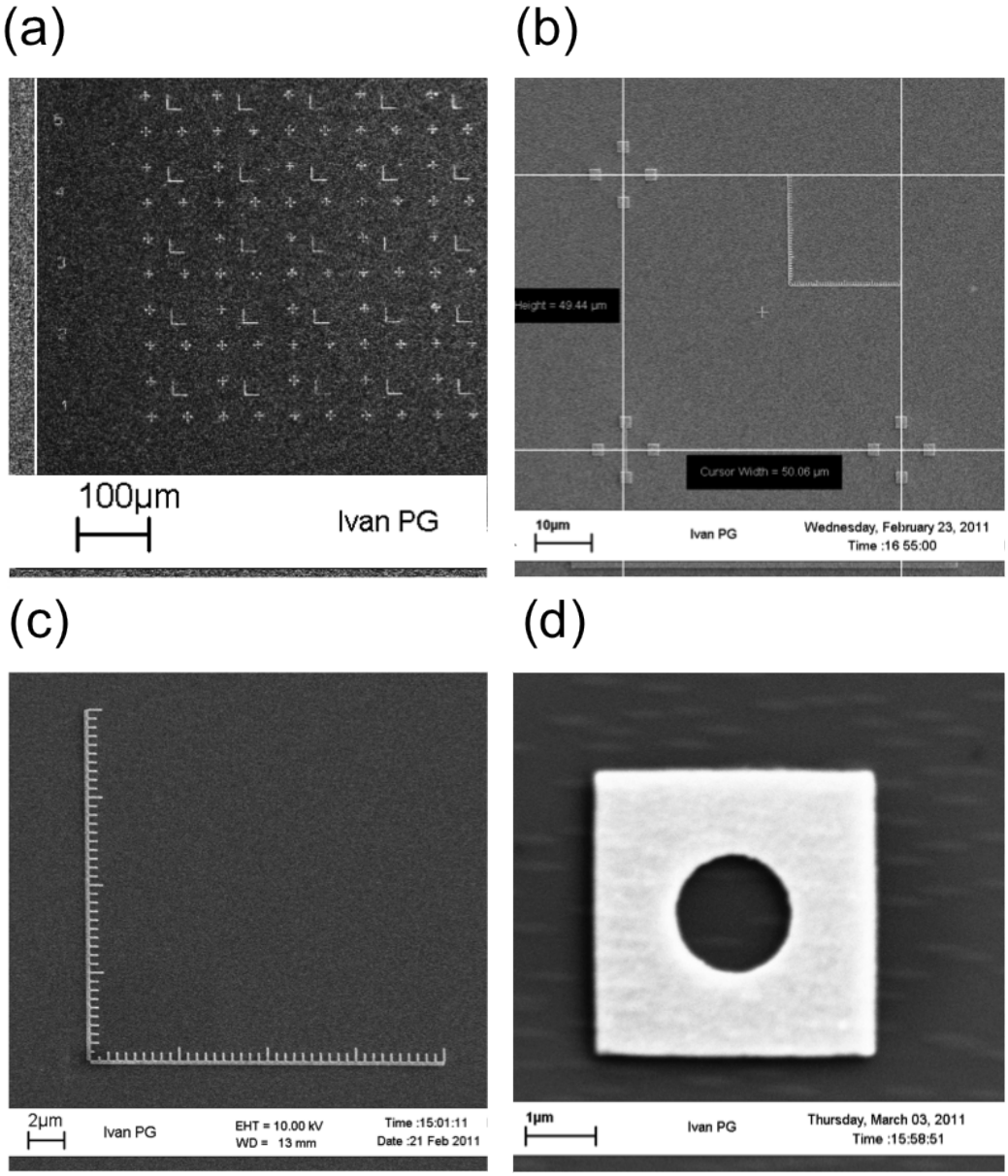

Figure 8.2: **Description of the reference systems with Au–ruler and alignment marks.** a) Scanning electron microscope (SEM) image of an array of 25–sets of reference systems. b) SEM image of the metallic alignment marks, metallic origin mark and metallic ruler. c) Close up SEM image of the metallic ruler, showing the nano–sized ticks. d) Close up SEM image of the Ti–window to assist the optical characterization of the target quantum dot.

with a diluted HF, which does not remove the Cr/Au marks. Such a metallic window makes more systematic and faster the achievement of the QD locations on the confocal microscope. Since the opening is ≤ 2 μm in diameter, we have assumed that such a Ti–mask does not affect the optical properties of the QD. It is worth noting that the fabrication of those metallic opening serves as a test to demonstrate spatial positioning of a pattern, which was useful to fabricate the L7–PCM. The Ti–window was removed after the optical characterization in order to further proceed with the fabrication of the L7–PCM. The optical characterization at this stage consisted of the determination of the spectral positions and dynamical properties of the target QDs. Figure 8.3a presents the target dot centered within the Ti–mask. A μPL map of that region occupied by the mask opening (Figure 8.3b) served to attribute the corresponding spectral region of the target QD. The μPL spectrum at the QD target position is shown in Figure 8.3c. The emission spectrum of single InAs QDs grown by droplet epitaxy consists of multiple narrow peaks as shown in figure 8.3c. Each peak corresponds to radiative recombination of an electron hole pair in the presence of a different number of excess electrons.[180] A highly charged environment is an unwanted feature for quantum information applications and its relation with the growth conditions is being investigated. Once we have determined the optical properties and the coordinates of the target QD with respect to the ruler, we proceeded with the fabrication of the photonic crystal microcavity.

8.3.6 Spatial and spectral tuning of the L7–PCM to a selected QD

Fabrication of the L7–PCM in a test–sample

We have chosen the L7–PCM since no fine–tuning of any of the holes (either in size or position) is required to achieve high–Q.[60, 181, 44] A large series of samples coming from the same wafer were fabricated to get the right fabrication parameters. Prior to the fabrication of the cavities on the sample with the target QDs, it is necessary to practice test cavities to ensure the spectral matching with the target dots. Due to the large accuracy required for the realization of PCMs operating in a specific wavelength, and considering that the sample already received several technological steps above indicated, it becomes necessary to test the fabrication procedure on the same wafer out of the regions enclosed by the

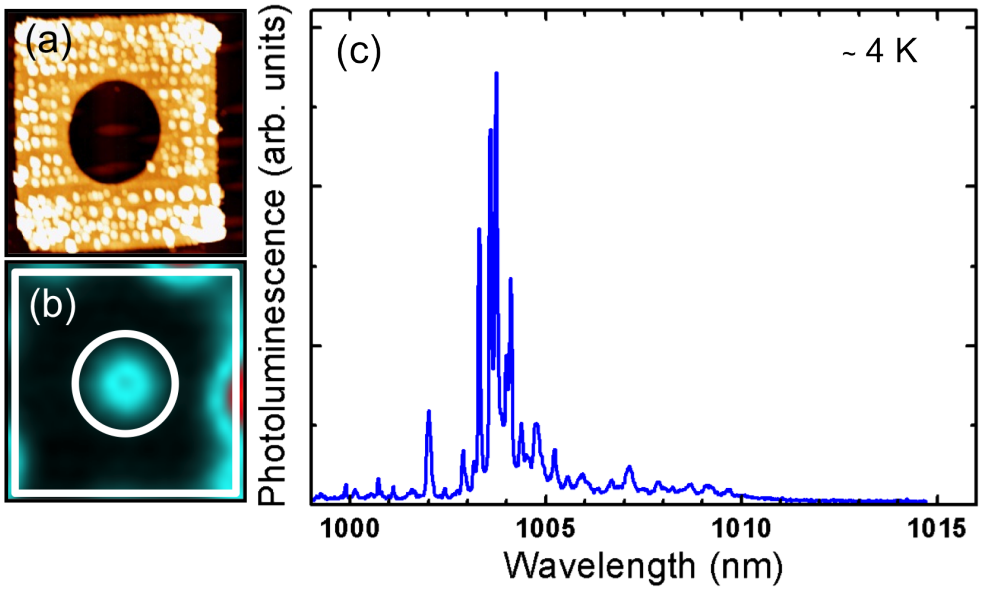

Figure 8.3: **Optical characterization at low temperature of the target quantum dot.** a) Atomic force microscopy image showing the detail of a Ti–mask with a target quantum dot (QD) in the middle. b) Photoluminesence (PL) map at low temperature demonstrating the optical emission from target QD. The white lines are guides to the eye to delimit the extension of the mask. c) PL spectrum at low temperature of the target QD to set the target wavelength.

alignment marks. With this aim, after the removal of the Ti–windows, we have deposited a thin layer (85 nm) of SiO_x layer that served as a hard mask. Next, we deposited a layer of ZEP–520A resist 460 nm thick. At this stage, we cleaved the sample into two pieces. One piece contained the target dots and the other one (test–sample) followed the same fabrication procedure as the first one. It is worth noting the importance of cleaving the sample at this stage and not before the deposition of the SiO_x and ZEP–520A. Any deviation on the thickness of any of those layers from one sample to another may induce deviations on the size of the resulting holes that may cause an unexpected shift of the cavity mode with respect to the target spectral position. In this way both pieces were at the same starting point. To complete the fabrication procedure we performed the pattern on the resist through EBL and a developing process. Next, we transferred the pattern to the hard mask assisted by the reactive ion beam etching. To transfer the pattern to the active GaAs slab, we practiced a reactive ion etching–inductively coupled plasma etching. The final step consists of a wet etching that removes the sacrificial layer underneath the photonic structures. Further information about the fabrication procedure can be found elsewhere.[16, 177] Figure 8.4 presents the results obtained on the test–sample. The general trends on the spectral positions of the fundamental mode of the L7–PCM are observed in Figure 8.4a.

It is worth noting that the same spectral position is achievable with different parameters, i. e., dose and r/a–values (Figure 8.4a). It is the lithography the step in which the differences between the structures is accomplished. The L7–PCM was designed to have the fundamental mode within the spectral window enclosed by the inhomogeneous linewidth of the ensemble. For given conditions of exposure (i. e., 30 kV and 20 pA) and developing, we can achieve a smooth evolution of the spectral position for the fundamental mode of the L7–PCM through either of the following parameters: lattice constant (a), nominal hole radius (r) and dose factor. Since several nominal parameters provide those spectral positions, we selected those parameters that maximized the Q (Figure 8.4b). Although a dispersion on the data is observed, from the analysis of Figure 8.4a–b it is worth noting that a higher Q is reached for small nominal radius and large dose factors.

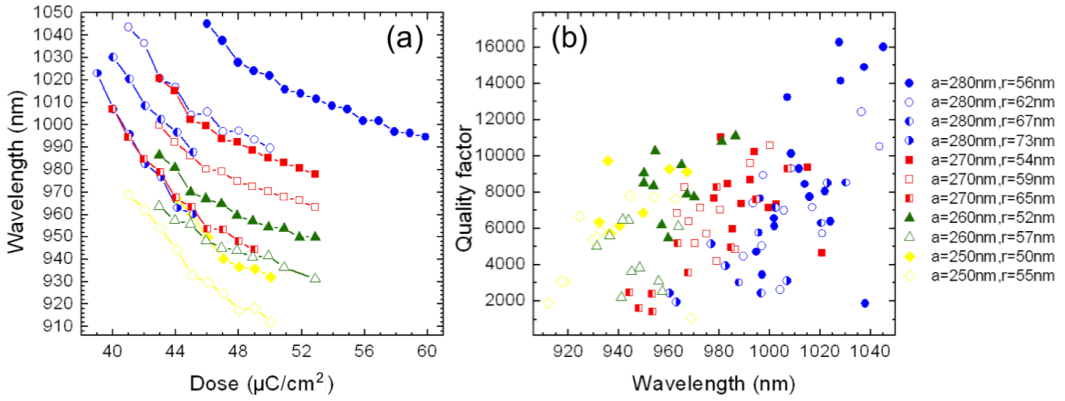

Figure 8.4: **Determination of the experimental quality factor and spectral position of the photonic crystal microcavity fundamental mode in the test–sample.** a) Evolution of the spectral position with the dose factor exposed during the electron beam lithography for the L7–photonic crystal microcavity (PCM) fundamental mode, b) Quality factor *vs.* the spectral position of the L7–PCM fundamental mode. An evolution on the lattice constant (a = 250–280 nm) and the hole radius (r = 50–73 nm) was performed.

8.3.7 Fabrication of the selected L7–PCM over the target QD

After the analysis of the data from the test–sample we proceeded to the fabrication of the selected L7–PCM over the sample containing the target QDs. Figure 8.5 present the results obtained for one of the systems. To summarize preliminary results, we presented the PL spectrum measured over the target QD before (Figure 8.5a) and after (Figure 8.5b) the fabrication of the selected L7–PCM, together with an AFM image of the QD centered within the Ti–mask (Figure 8.5a–inset) and after the fabrication of the selected L7–PCM (Figure 8.5b–inset).

The approach we have followed stems from the reproducibility in the spectral position of the L7–PCM fundamental mode for a given set of parameters, i.e., dose, a, r etc. From previous and numerous experiments we estimated that, for a given set of fabrication parameters, our reproducibility along the fabrication process sets the deviation on the spectral position of the fundamental mode from one sample to another in 5–10 nm. As it results more feasible to shift afterwards the mode resonances towards the blue by several techniques, we adopted to set the target cavity slightly redshifted (pointing to 5 to 10 nm to the red) with respect to the spectral position of the QD. We have selected a cavity with nominal values:

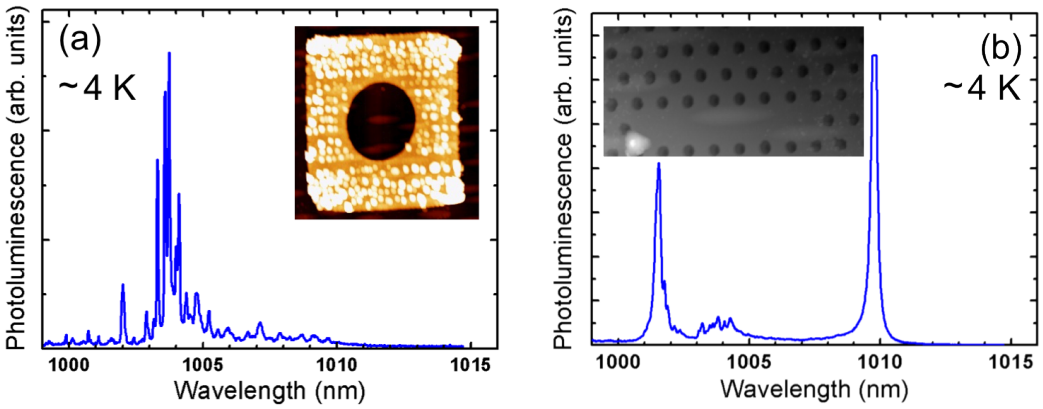

Figure 8.5: **Spectra corresponding to the target QD before and after the fabrication of the photonic crystal microcavity in specific spectral and spatial positions.** a) Photoluminescence (PL) spectrum of the QD before the fabrication of the L7–photonic crystal microcavity; the inset shows an atomic force microscopy (AFM) image the target QD within the center of the Ti–mask. b) PL spectrum of the system after the fabrication of the L7–PCM. Two resonances corresponding to the first and second modes of the L7–PCM are surrounding the QD multi–peak structure; the inset shows an AFM image of the target QD within the cavity defect. The target mound is slightly deviated upwards with respect to the center of the defect. A small particle is observed on the lower left corner of the image.

a = 280 nm, r = 56 nm, *dose* = 53 μC/cm^2. Those parameters provided in the test–sample a fundamental mode with a Q = 9200 and λ = 1012 nm. The spectral position of the resulting cavity fundamental mode (Figure 8.5b) is $\simeq$ 2 nm towards the blue (1009.8 nm) with respect that in the test–sample, which reslts in $\simeq$ 6 nm redshifted with respect to the target QD. The second mode of the cavity is also shown at 1002.4 nm which is slightly blueshifted with respect to the QD. It is worth noting that the found Q–factor for the fundamental mode is smaller ($Q \simeq 4500$) than that obtained in the test–sample. An explanation could be found in the dust or debris found in the area where we fabricated the Ti–mask (see AFM picture in Figure 8.5–inset). The Ti removal through a HF dilution might have not completely cleaned the surface. We will take advantage of the posterior wet etching necessary to make the mode and the QD overlap which hopefully will clean the surface near the defect and thus increase the Q. We have evaluated the wet etching by the technique of KOH slow etching, but other techniques can be found elsewhere.

Regarding the spatial matching the AFM image shows the target mound feature within the cavity defect. An analysis of the image suggests that the QD might be less than 100 nm off the position where the electric field is maximum. We have only showed the results for one out of 25–devices. It is worth noting that the other 24 systems exhibited troubles during the fabrication procedure, thus resulting in either low–Q, or large spectral deviation or even the absence of the mode structure. Therefore, we have presented the results to date of unique device (inset Figure 8.5b–inset) as a proof of concept. Further insights are necessary to gain experience and achieve deterministic QD–PCM coupling in a systematic way, as other authors do with other approximations.[128] Further optical characterization is neccessary in order to evaluate the coupling of the QD–PCM system.

8.3.8 Summary

We presented a fabrication procedure to achieve a photonic PCM–QD system to exhibit deterministic coupling. The approach involves a growth technique for the embedded QDs that results in the release of a mound feature on the surface. A spatial selection of a specific mound in terms of spatial isolation is referred to a metallic ruler with coordinates given by atomic force microscopy (AFM) and translated into the electron beam lithography (EBL) reference system, through the fabrication of a set of alignment marks. An L7–PCM was designed and

tested reaching Q–values up to 16000 in the 980 nm window. The fabrication of the optimum L7–PCM was released over the target QD. Further steps of optical characterization and ultra–slow wet etching process are necessary to spectrally match the cavity mode to the QD.

8.4 On–going work

As a result of our fabrication procedure we have demonstrated a method to achieve spatial matching between the center of the L7–PCM (where the field is maximum for the fundamental mode) and the QD location. The spectral position of the cavity–mode is $\simeq$6 nm red–shifted with respect to the QD. The next step is to fine–tune the optical mode towards the spectral position of the QD.[182, 183, 167, 184, 185, 175, 14] To this aim, we will proceed with a wet chemical etching based either on the KOH solution.[14] Since we developed a nm–scale wet etching on the shift of the cavity mode by means of a KOH solution, we will perform several steps consisting on wet etching and optical characterization to accurately tune the mode and, therefore, match the emission of the QD.

Chapter 9

Enhanced quantum efficiency of Ge solar cells by a two–dimensional photonic crystal nanostructured surface

I. Prieto,[1] B. Galiana,[2] P. A. Postigo,[1] C. Algora,[2] L. J. Martinez,[1] and I. Rey-Stolle[2]

Appl. Phys. Lett. **94,** 191102 (2009)

[1]IMM–Instituto de Microelectrónica de Madrid (CNM–CSIC), Isaac Newton 8, PTM, Tres Cantos, Madrid E–28760, Spain

[2]Instituto de Energía Solar–Universidad Politécnica de Madrid, E.T.S.I. Telecomunicación, Avda. Complutense s/n, 28040 Madrid, Spain

9.1 Context & motivation

The use of photonic crystals in any device working with the light–matter interaction may enhance its performance. In this Chapter a photonic crystal was fabricated on top of a solar cell to enhance the transmission of light from air to the semiconductor and to promote light–matter interaction through multi–reflection. For that purpose, a photonic crystal structure was fabricated by ion–etching on the InGaP window of a Ge p–n junction. The work, although partially related with the main topic of this Thesis, opens new ways to the use of photonic crystals in solar cells.

9.2 Contribution

My contributions to this work are:

- Design of the photonic crystal structure for e–beam lithography over a broad area (~ 1 mm^2),
- Fabrication of the photonic crystal structure

9.3 Publication

9.3.1 Abstract

A single–junction germanium solar cell with a photonic crystal nanostructured surface has been developed. The solar cell comprises a Ge p–n junction and an InGaP window layer. The InGaP window layer has been nano–patterned with an extended photonic crystal structure consisting on a triangular lattice of holes with submicronic sizes. Enhancements of the external quantum efficiency of 22% for a wide range of wavelengths and up to a 46% for specific wavelengths have been measured, which implies an increase in photocurrent between 11% and 22%. A clear correlation with the area of photonic crystal patterned has been observed.

9.3.2 Introduction

During the last years, much attention has been paid to photonic crystals (PCs) [2, 186] for different applications. PCs and photonic bandgap materials have been

also proposed and used for solar cells.[187, 188, 189, 190] Moreover, there has been an important amount of work on light extraction out of light-emitting diode devices by 2D PCs.[191, 192, 193] In a similar way, transmission of the incident light inside a device can be enhanced by a 2D-PC layer and there are a number of theoretical [194, 195, 196] and experimental [197, 198] works related to this. Nevertheless, little work has been done in the actual manufacture and characterization of a complete solar cell with a 2D PC on its front surface, conceived as a periodic distribution of the dielectric constant in the plane (the surface of the solar cell) and involving subwavelength motifs. In this case, the PC effect is slightly different from that in slabs or suspended membranes [199] and lacks of the confinement in the vertical direction provided by total internal reflection. Despite the partial vertical confinement, all the above mentioned reasons can justify to try to use a PC front surface with subwavelength motifs. Consequently, the aim of this work is to prove the validity of a 2D PC as an additional strategy to improve solar cells performance. With this aim, we have manufactured a single p–n junction solar cell based on Ge with a PC nanopatterned InGaP window layer. In order to quantify the improvement introduced by the PC, the external quantum efficiency (EQE) and the I-V curves under illumination of the solar cells manufactured in the same batch with and with- out the PC have been measured. We have found an increase in EQE around 22% in average for the solar cells with the PC structure, which in terms of photocurrent implies an increase between 16% and 25% for direct terrestrial spectrum (AM1.5D).

9.3.3 The device

A layout of the device is shown in Fig. 9.1. The solar cell is composed by a single p-n junction formed by the diffusion of phosphorus to the p-type Ge substrate during the metal–organic vapor phase epitaxy growth of a GaInP window layer. Ge wafers, 150 μm thick, (100) 6° off toward (111) have been used as substrates. The thickness of the InGaP window layer is 1000 nm and it is n-type doped with Si with a concentration $N_D = 1{\times}10^{18}$ cm^3. A GaAs cap layer has been grown to ease the front Ohmic contact. The back contact is carried out with Au. Front Ohmic contacts by deposition of the AuGe–Ni–Au system outside of a circular pattern made by photolithographic techniques were performed. No antireflection coating has been deposited. The whole diameter of the uncovered front surface ranges from 1.4 to 1.6 mm on different devices with zero shadowing factor (no fingers

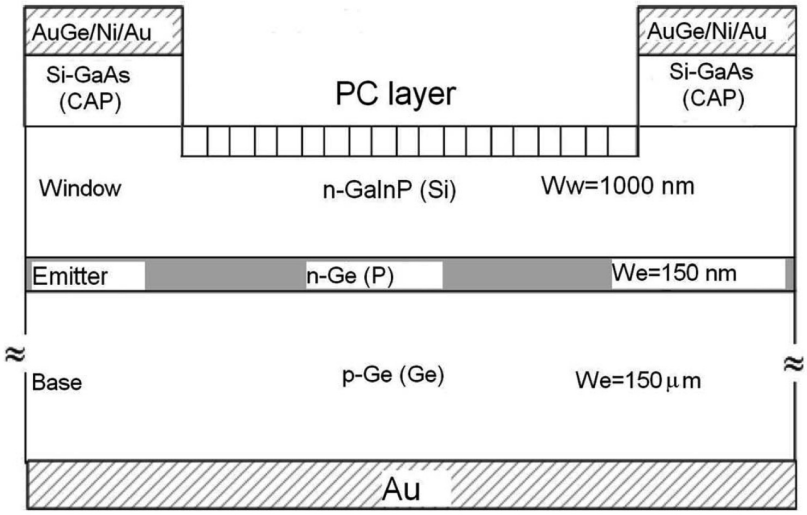

Figure 9.1: **Schematics of the solar cell patterned with the photonic crystal.** Layout of the cross section of the solar cell patterned with the photonic crystal (PC) layer formed by a triangular lattice of holes with radius $r = 200$ nm, lattice constant $a = 600$ nm, and depth $d = 300$ nm.

have been defined). The major advantage of a PC window layer is, in principle, to introduce diffraction, where the photon momentum ($\mathbf{k}$) can be scattered away from the specular direction with ($\mathbf{k} = k_{\mathrm{i}} + G$), where G is a reciprocal lattice vector and k_{rmi} is the incident wave vector. The dielectric contrast of the air to InGaP (~ 3) is large enough for sufficient diffraction of light by the PC. Maximum diffraction is expected when the Fourier components of the dielectric function of the 2D PC is a maximum. Moreover, it has been shown16 that discrete spots of diffraction pattern in a weakly modulated PC, including those of conventional diffraction gratings, become continuous when the dielectric modulation becomes finite. Furthermore, in a finite–modulated PC, the diffraction can take place even in the region prohibited by Braggs law producing available states for the incident light, which are evanescent in the case of a diffraction grating.

9.3.4 Design

Using a triangular lattice of holes of radius r and lattice parameter a, a value of $r/a \sim 0.3$ maximizes the strength of the first Fourier component (2π/a).[195] We take this value to fabricate a subwavelength periodic pattern (a PC in the horizontal plane) and to measure its actual performance. Nevertheless this design

may need of careful optimization for future devices. The depth of the holes for the top transmission PC grating (d) needs to be further optimized but a good starting value is for d/a around 0.5. Since this value depends on the wavelength, we have chosen an optimized thickness in average for the spectral region near the band edge (800–1600 nm). This is because the main applications of Ge solar cells are as forming part of GaInP/GaInAs/Ge triple–junction cells and for thermophotovoltaic applications. In both cases, the best performance of the Ge cell is pretended in the infrared. As a rule of thumb the lattice spacing should be near the wavelength of diffracted light inside the InGaP. However values of a can still offer improvement and may be more convenient for fabrication. For diffraction to the PC, it is necessary for a to be larger than the wavelength of light in the absorber layer ($a > \lambda/n$) where n is the index of refraction. We have used an averaged $n = 3.3$ for the InGaP in the spectral region considered (600–1800 nm). Since the maximum is around 1850 nm, the above condition is well satisfied for $a = 600$ nm. It is necessary to have several diffraction resonances within the wavelength window below the band edge, where the absorption length of photons is longer than the absorber layer thickness. Under all of these assumptions, the optimized solar cell with the PC can reduce considerably its reflection than without the PC.[195, 196]

9.3.5 Fabrication

We have manufactured the PC nanopattern on the front exposed surface of the device. For this purpose we have employed electron-beam lithography over an extended area of a square about 1×1 mm^2. The PC pattern is made on a poly–methyl–methacrylate (PMMA) layer deposited by spin–coating. The PC pattern is made by circular holes of radius $r = 200$ nm and a separation (lattice parameter) of $a = 600$ nm. The holes are distributed following a triangular–symmetry lattice and inside squares of 200×200 μm^2 separated 20 μm each. This is done to eliminate any photonic induced effect by misalignment during stitching of the writing fields. Also, the PC pattern is placed well inside the circular exposed surface, avoiding border effects or possible damage to the electrical contacts. In this way around a 60% of the total surface of the solar cell is patterned. After developing of the PMMA resist, the pattern is transferred to the InGaP layer by Ar–based reactive ion beam etching. The deep of the etched holes is 200 nm. Finally, the remains of the PMMA layer are eliminated by oxygen–plasma etch-

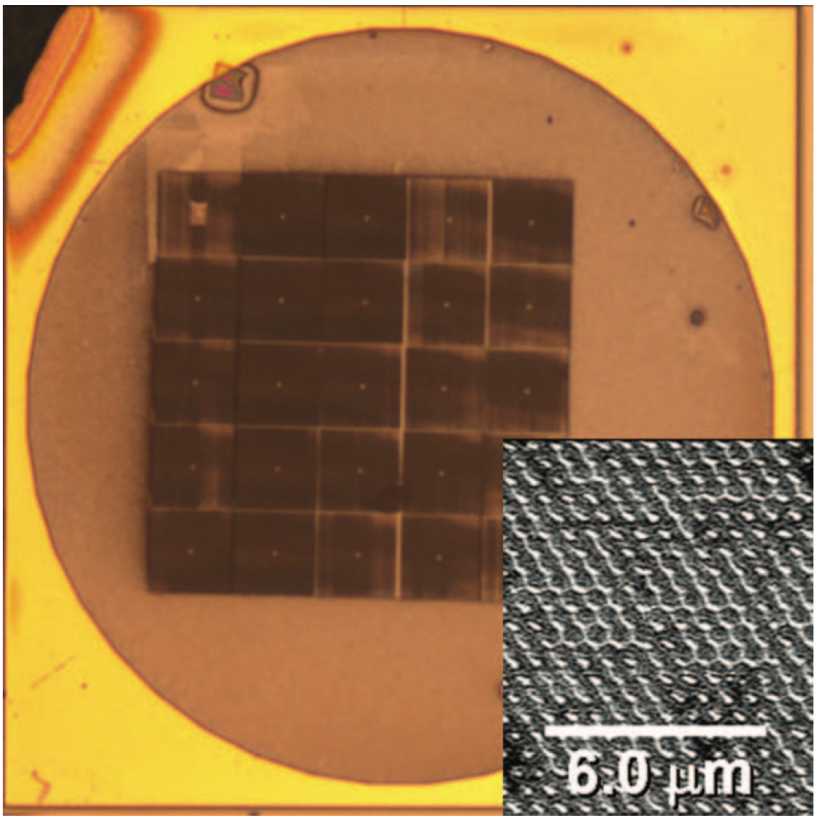

Figure 9.2: **Top view of the solar cell patterned with the photonic crystal.** Microscope picture of the solar cell device with the area patterned with a photonic crystal (1 mm^2).

ing. Figure 9.2 shows a microscope picture of the device with an inset showing a scanning electron microscope (SEM) picture of the PC nanopatterned structure. Solar cells with and without the PC pattern are fabricated together in order to facilitate experimental comparison. Non–homogeneities due to change in material or processing technology are inexistent on these structures.

9.3.6 Characterization

I-V curves under illumination and EQE measurements have been carried out in a monochromator–based system with a light-beam chopper. The primary light source is a 1000 W Xe lamp. The system has a monitor cell to assess the real–time fluctuations of the lamp. Both the monitor cell and the test cell are connected to two independent lock–in amplifiers, which permits the simultaneous measurement of both the monitor cell and the reference/test cell. This setup allows the

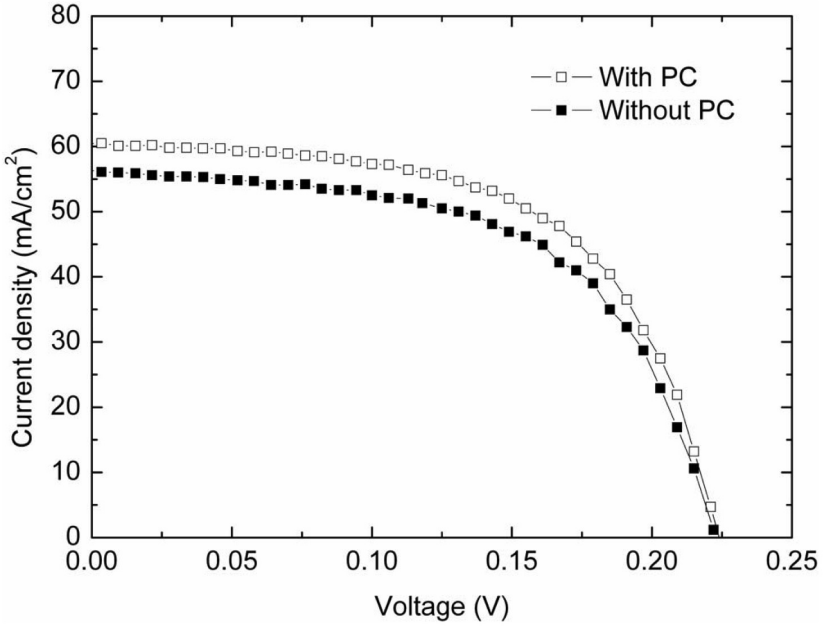

Figure 9.3: **I–V characterization of the solar cell.** I–V curves under illumination for the photonic crystal (PC)–patterned and non–patterned solar cells.

minimization of the measurement errors resulting from lamp fluctuations, very significant in certain spectral ranges. The chuck for the test cell is temperature controlled by a Peltier element. The spectral range goes from 300 to 2000 nm but the relevant range for the cell is between 600 and 1800 nm. In order to calibrate the system status at the beginning of every measurements session, a GaSb solar cell is used as reference. The spot light impinging the cells was in all cases of 1.2 mm of diameter. Figure 9.3 shows the I–V curves under illumination of two solar cells, one with PC pattern and one without it, otherwise identical. Despite the intrinsic performance of the used solar cells as not optimum (filling factors around 52%) due to their experimental nature (these cells were obtained with heteroepitaxial techniques), there is an improvement of the efficiency of about 11% for the cell with PC pattern. In this prototype, only a 40% of the surface was patterned with the PC. By linear extrapolation, an enhancement of 25%–26% can be obtained for a solar cell with the entire surface patterned by a PC. The measured increment in the photocurrent is 8%, which gives an enhancement in the photocurrent of 22% for a fully covered surface. The open–circuit voltage (VOC) was not degraded. Also, the dark I–V curves of both devices, with and without PC were observed to be exactly the same, which implied that none

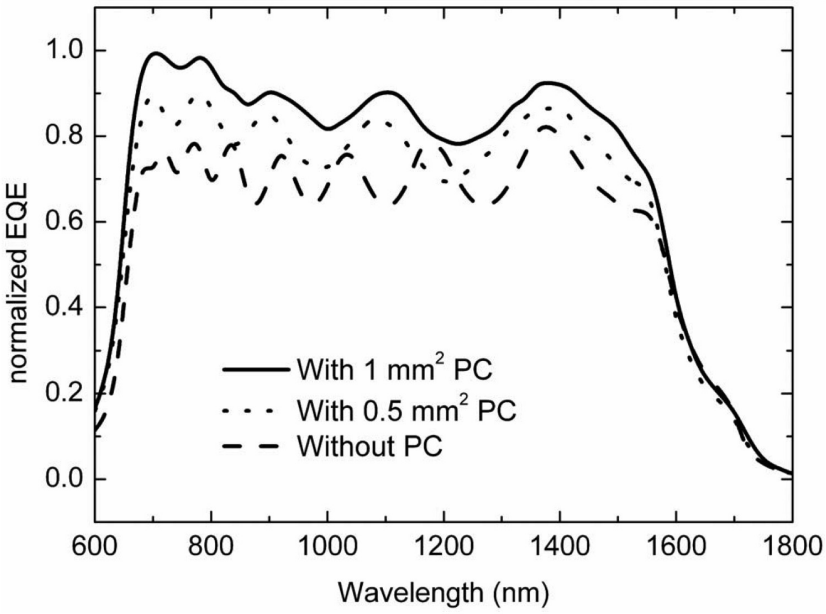

Figure 9.4: **External quantum efficiency of the solar cell** Relative EQE for two photonic crystal (PC)–patterned solar cells with two different areas patterned, 1 mm^2 (black line) and 0.5 mm^2 (dotted line) and for a non–patterned solar cell of the same size (dashed line).

degradation has been introduced to the device due to the PC pattern fabrication. Figure 9.4 shows the relative EQE for two PC–patterned solar cells with two different areas patterned, 1 mm^2 and 0.5 mm^2. The experimental EQE–data have been normalized to the highest EQE–value. Figure 9.3 shows also the EQE for a non–patterned solar cell of the same size. The EQE in both the PC–patterned solar cells are always higher than in the non–patterned cell. For the cell with PC-pattern covering 1 mm^2 the enhancement of current using the spectrum AM1.5D is 25%, whereas for the cell with half of the area patterned the increase is 16%. Figure 9.5 shows the reflectivity measured in the solar cell with the 1 mm^2 patterned PC and in the bare solar cell. The size of the spot is around 250 μm in diameter. The reflectivity measured at 45° incidence is smaller for the PC solar cell for most of the wavelengths. Measurements performed at normal incidence give very similar values and are not included. All of this shows the validity of our approach to enhance the performance of solar cells, which could be also applied to other photon–sensing devices such as photodetectors and thermophotovoltaic devices. Further work is needed to understand in deep all the possible photonic effects involved, such as subwavelength diffraction, variation of

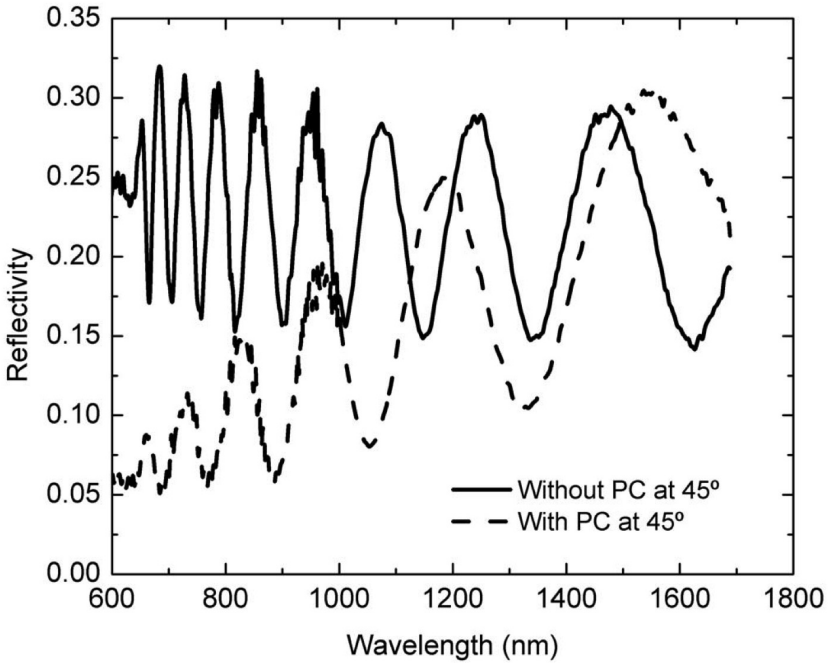

Figure 9.5: **Reflectivity of the solar cell.** Reflectivity of the photonic crystal–patterned solar cell and the non–patterned reference cell.

the index of refraction due to the photonic bands, change of the lifetime of the photons by the PC layer, or role of the submicronic roughness produced during the etching. Moreover, especial efforts should be made in order to find optimized PC patterns for the above mentioned devices.

9.3.7 Conclusions

In summary, we have manufactured a single–junction Ge/InGaP solar cell with a PC nanostructured surface. An increase in the photocurrent up to 8% has been achieved on a solar cell with 40% of its surface covered with a PC pattern. Enhancements of the EQE of 22% for a wide range of wavelengths and up to 46% for specific wavelengths have been measured. A correlation with the area of PC patterned has been observed. Further work is needed for the optimization of the PC pattern and to asses the advantages of using a PC–pattern versus antireflection coatings, which can be compatible with the PC structure, and to establish its performance with the angle of incidence.

Chapter 10

Conclusions

The main results of this Thesis are:

1. We have developed a fabrication procedure for the release of high–Q photonic crystal microcavities (PCMs) on GaAs–based material. A thin layer (85 nm) of SiO_x is deposited by plasma enhanced chemical vapour deposition (PECVD) and serves as a hard mask for etching. After the coating of 360 nm of ZEP–520A resist, electron beam lithography (EBL) and developing procedures define the holes on the resist. Two dry etching procedures, i. e., reactive ion beam etching (RIBE) and inductively coupled plasma etching–reactive ion etching (ICP–RIE) are performed to define the pattern on the active slab. Optimum conditions for the partial N_2 flux content in a BCl_3:N_2 gax mixture for the ICP–RIE process have been found to yield vertical and smooth sidewalls. The suspended membrane is released by removing the $Al_{0.70}Ga_{0.30}As$ sacrificial layer with diluted HF. A careful control of both the duration of the wet etching and the concentration of the hydrofluoric dilution is needed to prevent the formation of the flake structures. Q–factors up to 30000 are obtained in samples containing InAsSb quantum dots (QDs) emitting at room temperature (RT) in the 1.3 μm telecom window.

2. Continuous wave and near thresholdless laser operation (power threshold $P_{\text{th}} = 840$ nW and spontaneous emission coupling factor $\beta = 0.85$) in the 1.3 μm telecom window at room temperature was demonstrated for a system combining a single layer of InAsSb QDs with a photonic crystal microcavity. We showed that thermally activated processes, such as

non–radiative recombination, are not an insurmountable obstacle to the realization of laser sources with characteristics similar to those observed in near thresholdless lasers at temperatures few degrees above absolute zero. Such highly–efficient systems are very promising candidates for applications in optical integrated circuits, potentially enabling low consumption electrically–injected devices based on PCMs at RT.

3. We have developed a methodology to simulate a PCM embedding a QW within the local linear response theory by finite difference time domain (FDTD). Depending on the damping rates of the cavity mode and exciton resonances, the power spectrum greatly depends on the time window employed in the frequency transform of the signal. Moreover, the time windowing of the electric field time evolution also distorts the spectrum obtained through the harmonic inversion (HI) method. Fitting the results to the analytical expression of the Fourier transform of two harmonic oscillators, we have successfully identified that the dependence of the spectra structure on the initial time has its origin on a phase difference between the oscillators. After establishing the methodology for the frequency analysis, we have successfully characterized the PCM–QW system in the strong coupling regime (SCR). Finally, we have seen that even though the far field of the fundamental mode of an L7–PCM is linearly polarized, the coupling takes place for any orientation of the material excitonic polarization.

4. We have presented three fabrication strategies towards the achievement of coupled site controlled quantum dot (SCQD)–PCM mode systems. Two of them are based on PC structure fabrication on GaAs and MBE growth of SCQDs and pre–patterned structures.

4.1. In the first approach (referred to as re–grown cavity) we have demonstrated selective InAs nucleation on pre–patterned PC structures. The epitaxial re–growth process on the pre–patterned PCMs leads to a strong evolution of the hole shape that may degrade the performance. The photonic properties of the re–grown cavities have been studied in comparison to that of standard cavities. The circular shape of the holes in standard L7–PCMs evolves to a hexagonal shape in the re-grown L7–PCMs. Optical characterization performed in standard and re-grown L7–PCM shows that the mode photonic structure is preserved after the re–growth step including its linear polar-

ization. A blueshift for the fundamental mode in the re-grown structures with respect to the standard PCM has been measured and attributed to a larger effective FF. The fundamental mode of re-grown L7–PCMs presents high Q–values (up to 6000) and in average maintains a 36% of its Q for L7$\perp$ PCMs and a 15% for L7$\parallel$ PCMs with respect to those in standard L7–PCMs. FDTD simulations predict that Q–values can be similar to standard cavities for a broad range of r/a values and show a better performance for re–grown PCMs with ΓK perpendicular to [110] in agreement with experiments. Overall, our result supports the use of epitaxial re–growth methods to obtain PCMs coupled to site controlled QDs.

4.2. The second approach we have addressed is the so–called "Etched ruler". The use of a set of reference system consisting of a pre–patterned ruler and alignment marks provides a method that may allow a systematic fabrication of systems to investigate the coupling of a single or several QDs to a PCM mode. We have noticed a large amount of InAs QDs nucleated next to the ruler axes. The density decreases rapidly 2 μm beyond the edges. Far from this region, in the area enclosed by the ruler, still a small density of QDs (around 0.1 μm^2) was detected.

4.3. As a third strategy to achieve a PCM–QD system to exhibit deterministic coupling, we presented the "golden ruler". The approach involves a growth technique of self–asembled QDs that results in the release of a mound feature on the surface. A spatial selection of a specific mound in terms of spatial isolation is referred to a metallic ruler whith coordinates given by AFM. The coordinates are translated into the EBL reference system, through the fabrication of a set of alignment marks. An L7–PCM was designed and tested reaching Q–values up to 16000 in the 980 nm window. The fabrication of the optimum L7–PCM was released over the target QD.

5. As an application of the potential of the photonic crystals, we have manufactured a single–junction Ge/InGaP solar cell with a PC nanostructured surface. An increase in the photocurrent up to 8% has been achieved on a solar cell with 40% of its surface covered with a PC–pattern. Enhancements of the external quantum efficiency (EQE) of 22% for a wide range of wavelengths and up to 46% for specific wavelengths have been measured. A correlation with the area of PC–patterned has been observed. Further

work is needed for the optimization of the PC–pattern and to asses the advantages of using a PC–pattern versus antireflection coatings, which can be compatible with the PC structure, and to establish its performance with the angle of incidence.

Chapter 11

Conclusiones

Los principales resultados de esta Tesis son:

1. Hemos desarrollado un proceso de fabricación para la obtención de cavidades de cristal fotónico de alto factor de calidad en materiales basados en GaAs. Una lámina delgada (85 nm) de SiO_x es depositada mediante PECVD y sirve como máscara dura para ataque por plasma. Tras depositar una capa de resina ZEP–520A de 360 nm, practicamos litografía por haz de electrones y revelado para definir los agujeros en la resina. Dos procesos de ataque seco, esto es, RIBE y RIE–ICP son realizados para definir el patrón en la lámina activa. Las condiciones óptimas para el contenido parcial de N_2 en una mezcla de gases de BCl_3:N_2 para el proceso RIE–ICP han sido encontradas para obtener paredes verticales y poco rugosas. La membrana suspendida se realiza eliminando la capa sacrificial de $Al_{0.70}Ga_{0.30}As$ con ataque húmedo de ácido fluorhídrico. Un cuidadoso control en la duración del ataque y la concentración de la disolución es necesario para prevenir la formación de residuos Factores de calidad de hasta 30000 han sido obtenidos en muestras que contienen puntos cuánticos de InAsSb emitiendo a temperatura ambiente en la ventana de telecomunicaciones de 1.3 μm.

2. Un laser quasi sin umbral operando bajo excitación continua (umbral de $P_{\mathrm{th}} = 840$ nW y factor de acoplamiento de emisión espontánea $\beta = 0.85$) en la ventana de telecomunicaciones de 1.3 μm a temperatura ambiente ha sido demostrada en sistemas combinando una capa de puntos cuánticos de InAsSb embebidos en una cavidad de cristal fotónico. Hemos demostrado que los procesos de activación térmica, como recombinación no radiativa,

no son un obstáculo insalvable para la realización de fuentes laser con características similares a las observadas en régimen de quasi sin umbral a temperaturas pocos grados por encima del cero absoluto. Estas fuentes altamente eficientes son candidatos muy prometedoras para aplicaciones en integración de circuitos ópticos, potencialmente habilitando la obtención de dispositivos de inyección eléctrica de bajo consumo en cavidades de cristal fotónico a temperatura ambiente.

3. Hemos desarrollado una metodología para simular una cavidad de cristal fotónico embebiendo un pozo cuántico con teoría de respuesta local lineal mediante la técnica de elementos finitos en el dominio temporal (del inglés, FDTD). Dependiendo de las pérdidas de la cavidad y las resonancias excitónicas, el espectro de potencia depende enormemente de la ventana temporal empleada en la transformación frecuencial de la seal. Más aún, la ventana temporal de la evolución temporal del campo eléctrico también altera el espectro obtenido a través del método HI. Ajustando los resultados a una expresión analítica de la transformación de Fourier de dos osciladores armónicos, hemos identificado exitosamente que la dependencia de la estructura de los espectros en el tiempo inicial tiene su origen en la diferencia de fase entre osciladores. Tras establecer la metodología para el análisis frecuencial, hemos caracterizado exitosamente el sistema cavidad–pozo cuántico en el régimen de acoplamiento fuerte (del inglés, SCR). Finalmente, hemos visto que a pesar de que en campo lejano el modo fundamental de la cavidad está linealmente polarizado, el acoplamiento tiene lugar para cualquier orientación de la polarización excitónica del material.

4. Hemos presentado tres estrategias de fabricación hacia la consecución de un sistema de acoplamiento de punto cuántico con control en posición y un modo de cavidad de cristal fotónico. Dos de ellas están basadas en la fabricación de estructuras de cristal fotónico en GaAs y recrecimiento mediante MBE del punto cuántico posicionado y en estructuras pre–fabricadas.

4.1. En la primera aproximación (referida como cavidad re–crecida) hemos demostrado nucleación selectiva de InAs sobre estructuras de cristal fotónico pre–fabricadas. El proceso de re–crecimiento epitaxial en cavidades pre–fabricadas conlleva una fuerte evolución de la forma del agujero que puede degradar sus especificaciones. Las propiedades fotónicas de las cavidades

re–crecidas han sido estudiadas en comparación con cavidades estándar. La forma circular de los agujeros en cavidades estándar y cavidades re–crecidas muestra que la estructura de modos se preserva después del paso de re–growth, incluyendo su polarización lineal. Una desviación hacia el azul del modo fundamental en estructuras re–crecidas con respecto a las cavidades estándar ha sido medida y atribuida al mayor factor efectivo de llenado en estas estructuras. El modo fundamental de las cavidades L7 re–crecidas presenta alto factor de calidad (hasta 6000) y en promedio mantiene un 36% del correspondiente para L7$\perp$ y un 15% para L7$\parallel$ con respecto a las estándar. Simulaciones FDTD predicen que los valores del factor de calidad pueden ser similares a las cavidades estándar para un rango amplio de valores de r/a y muestran unas mejores especificaciones para las cavidades re–crecidas con ΓK perpendicular a [110] de acuerdo con los experimentos. Nuestros resultados apoyan el uso de métodos de re–crecimiento epitaxial para obtener cavidades de cristal fotónico acopladas a puntos cuánticos con control en posición.

4.2. La segunda aproximación que hemos desarrollado ha sido llamada "Regla atacada". El uso de un conjunto de sistemas de referencia consistentes en reglas pre–fabricadas y de marcas de alineamiento proporciona un método que puede permitir una fabricación sistemática de sistemas para investigar el acoplamiento de un único o varios puntos cuánticos a un modo de cavidad. Hemos advertido una gran cantidad de puntos cuánticos de InAs nucleados próximos a los ejes de la regla. La densidad disminuye rápidamente a 2 μm de los bordes. Conforme nos alejamos de los bordes, en el área encerrada por la regla, una densidad muy baja de puntos cuánticos (aproximadamente 0.1 μm^2) ha sido detectada.

4.3. Como tercera estrategia para la consecución de un sistema cavidad-punto exhibiendo acoplamiento determinista, hemos presentado la "regla de oro". La aproximación involucra una técnica de crecimiento de puntos cuánticos autoensamblados que resulta en la manifestación de un montículo en la superficie. Una selección espacial del montículo en términos de aislamiento espacial es referido a una regla metálica con coordenadas dadas por AFM. Las coordenadas son correspondidas al sistema de litografía por haz de electrones, a través de la fabricación de un conjunto de marcas de alineamiento.

Una cavidad L7 ha sido diseada y comprobada consiguiendo valores del factor de calidad de hasta 16000 en la ventana espectral de 980 nm. La fabricación de la cavidad óptima ha sido realizada sobre el QD previamente seleccionado y estudiado.

5. Como aplicación del potencial de los cristales fotónicos, hemos fabricado una célula solar de unión simple Ge/InGaP con una nanoestructura de cristal fotónico en la superficie. Un aumento en la fotocorriente de hasta un 8% ha sido conseguido en células solares con un 40% de su superficie con un patrón de cristal fotónico. Aumentos de la eficiencia cuántica externa del 22% para un rango de longitudes de onda y de hasta un 46% para longitudes de onda específicas han sido medidas. Una correlación con el área con patrón de cristal fotónico ha sido observado. Es necesaria una optimización del cristal fotónico para establecer las ventajas del uso de un cristal fotónico con respecto a los recubrimientos anti–reflectantes, que pueden ser compatibles con la estructura de cristal fotónico; asímismo, también es necesario mejorar las especificaciones con el ángulo de incidencia.

Chapter 12

List of publications

Published

16. I. Prieto, L. E. Muñoz–Camúñez, A. G. Taboada, C. Robles, J. M. Ripalda, and P. A. Postigo, Fabrication of high quality factor GaAs/InAsSb air suspended photonic crystal microcavities by inductively plasma etching and fast wet etching, *Journal of Vacuum Science Technology B*, 32 (1) 011204 (2014).

15. I. Prieto, J. Herranz, Y. González, L. González, L. Wewior, B. Alén, P. A. Postigo, High quality factor GaAs–based photonic crystal microcavities by epitaxial re–growth, *Optics Express*, 21 (25), 31615 (2013).

14. M. Maragkou, C. Sánchez–Muñoz, S. Lazić, E. Chernysheva, H. P. van der Meulen, A. González–Tudela, C. Tejedor, L. J. Martínez, I. Prieto, P. A. Postigo, and J. M. Calleja, Bichromatic dressing of a quantum dot detected by a remote second quantum dot, *Physical Review B*, 88, 075309 (2013).

13. J. Canet–Ferrer, I. Prieto, G. Muñoz–Matutano, L. J. Martínez, L. E. Muñoz–Camúñez, J. M. Llorens, D. Fuster, B. Alén, Y. González, L. González, P. A. Postigo, and J. P. Martínez–Pastor, Excitation power dependence of the Purcell effect in photonic crystal microcavity lasers with quantum wires, *Applied Physics Letters*, 102, 201105 (2013).

12. J. Llorens, I. Prieto, L. E. Muñoz-Camúñez, and P. A. Postigo, Analysis of the strong coupling regime of a quantum well in a photonic crystal microcavity and its polarization dependence studied by the finite–difference

time–domain method, *Journal of the Optical Society of America B* 30 (5) 1222 (2013).

11. M. Maragkou, A. K. Nowak, E. Gallardo, H. P. van der Meulen, I. Prieto, L. J. Martínez, P. A. Postigo, J. M. Calleja, Controlling the properties of single photon emitters via the Purcell effect, *Physical Review B* 86 (8) 085316 (2012).

10. J. Canet–Ferrer, L. J. Martínez, I. Prieto, B. Alén, G. Muñoz–Matutano, D. Fuster, Y. González, M. L. Dotor, L. González, P. A. Postigo, and J. P. Martnez–Pastor Purcell effect in photonic crystal microcavities embedding InAs/InP quantum wires, *Optics Express*, 20 (7) 7901–7914 (2012).

9. E. Gallardo, L. J. Martínez, A. K. Nowak, H. P. van der Meulen, J. M. Calleja, C. Tejedor, I. Prieto, D. Granados, A. G. Taboada, J.M. García and P. A. Postigo, Emission polarization control in semiconductor quantum dots coupled to a photonic crystal microcavity, *Optics Express*, 18 (12), 13301 (2010).

8. E. Gallardo, L. J. Martínez, A. K. Nowak, D. Sarkar, D. Sanvitto, H. P. van der Meulen, J. M. Calleja, I. Prieto, D. Granados, A. G. Taboada, J. M. García, and P. A. Postigo, Single–photon emission by semiconductor quantum rings in a photonic crystal *Journal of the Optical Society of America B–Optical Physics*, 27 (6) A21 (2010).

7. E. Gallardo, L. J. Martínez, A. K. Nowak, D. Sarkar, H. P. van der Meulen, J. M. Calleja, C. Tejedor, I. Prieto, D. Granados, A. G. Taboada, J.M. García and P. A. Postigo, Optical coupling of two distant InAs/GaAs quantum dots by a photonic crystal microcavity, *Physical Review B*, 193301, 81 (2010).

6. L. J. Martínez, B. Alén, I. Prieto, D. Fuster, L. González, Y. González, M. L. Dotor, and P. A. Postigo, Room temperature continuous wave operation in a photonic crystal microcavity laser with a single layer of InAs/InP self–assembled quantum wires, *Optics Express*, 17 (17), 14993 (2009).

5. L. J. Martínez, B. Alén, I. Prieto, J. F. Galisteo-López, M. Galli, L. C. Andreani, C. Seassal, P. Viktorovitch, and P. A. Postigo, Two-dimensional sur-

face emitting photonic crystal laser with hybrid triangular–graphite structure, *Optics Express*, 17(17), 15043 (2009).

4. L. J. Martínez, I. Prieto, B. Alén, and P. A. Postigo, Fabrication of high quality factor photonic crystal microcavities in InAsP/InP membranes combining reactive ion beam etching and reactive ion etching, *Journal of Vacuum Science and Technology B*, 27(4), 1081 (2009).

3. I. Prieto, B. Galiana, P. A. Postigo, C. Algora, L. J. Martínez, and I. Rey–Stolle, Enhanced quantum efficiency of Ge solar cells by a two–dimensional photonic crystal nanostructured surface, *Applied Physics Letters*, 94, 191102 (2009).
(Selected for the *Vir. J. Nan. Sci. & Tech.* / Volume 19 /Issue 21 / Optical properties and quantum optics, and Devices and Applications, Small, No. 12, 1365, 2009)

2. F. Olsson, M. Xie, S. Lourdudoss, I. Prieto, and P. A. Postigo, Epitaxial lateral overgrowth of InP on Si from nano–openings: Theoretical and experimental indication for defect filtering throughout the grown layer, *Journal of Applied Physics*, 104, 093112 (2008).

1. D. Sarkar, L. J. Martínez, I. Prieto–González, H. P. van der Meulen, J. M. Calleja, D. Granados, A. G. Taboada, J. M. García, A. R. Alija, P. A. Postigo, Optical Emission of InAs/GaAs Quantum Rings Coupled to a two–dimensional Photonic Crystal Microcavity, *Physica E*, 40 (6), 2156 (2008).

Conference proceedings

8. L. J. Martínez, B. Alén, I. Prieto, D. Fuster, L. González, Y. González, M. L. Dotor, and P. A. Postigo, Continuous and Pulsed Room Temperature Lasing Behaviour at 1.55 μm on High Quality Factor Photonic Crystal Microcavities, *12*$^{\text{th}}$ *International Conference on Transparent Optical Networks–ICTON*, (2011).

7. E. Gallardo, L. J. Martínez, A. K. Nowak, H. P. van der Meulen, J. M. Calleja, C. Tejedor, I. Prieto D. Granados, A. G. Taboada, J. M. García, and P. A. Postigo, Microcavity–Mediated Coupling of Two Distant InAs/

GaAs Quantum Dots, *Physics of Semiconductors: 30th International Conference on the Physics of Semiconductors, AIP Conference Proceedings*, 1399 (2011).

6. I. Prieto, J. Herranz, Y. González, J. Canet–Ferrer, L. Wewior, P. A. Postigo, B. Alén, L. González, M. Kaldirim, L. E. Muñoz–Camúñez, D. Fuster, A. G. Taboada, J. M. Ripalda, F. Briones, G. Muñoz–Matutano, and J. Martínez–Pastor, Different Strategies Towards the Deterministic Coupling of a Single Quantum Dot to a Photonic Crystal Cavity Mode, *13th International Conference on Transparent Optical Networks*, (2011).

5. E. Gallardo, L. J. Martínez, A. K. Nowak, D. Sarkar, D. Sanvitto, H. P. van der Meulen, J. M. Calleja, I. Prieto, A. R. Alija, D. Granados, A. G. Taboada, J. M. García, and P. A. Postigo, Single photon emission and quantum ring–cavity coupling in InAs/GaAs quantum rings, *11th International Conference on Optics of Excitons in Confined Systems, Journal of Physics Conference Series*, 210, 012037 (2010).

4. P. A. Postigo, M. Kaldirim, I. Prieto, L. J. Martínez, M. L. Dotor, M. Galli, L. C. Andreani, C. Seassal, Enhancement of solar cell efficiency using two–dimensional photonic crystals, *Photonic Crystal Materials and Devices IX, Proceedings of SPIE–The International Society for Optical Engineering*, 7713, 771307 (2010).

3. P. A. Postigo, L. J. Martínez, B. Alén, I. Prieto, D. Fuster, Y. González, L. González, M. L. Dotor, L. E. Muñoz, and M. Kaldirim, Continuous and pulsed room temperature lasing behaviour at 1.55 μm on high quality factor photonic crystal microcavities, *Active Photonic Materials III, Proceedings of SPIE–The International Society for Optical Engineering*, 7756, 77560X (2010).

2. L. J. Martínez, B. Alén, I. Prieto, C. Seassal, P. Viktorovitch, J. F. Galisteo–López, M. Galli, L. C. Andreani, and P. A. Postigo, Two–dimensional surface emitting photonic crystal laser with hybrid triangular–graphite structure, *ICTON 2009 11th International Conference on Transparent Optical Networks*, Vol 1 and 2, 1276–1279 (2009).

1. F. Olsson, M. Xie, F. Gerard, A. R. Alija, I. Prieto, P. A. Postigo, S. Lourdudoss, Epitaxial lateral overgrowth of InP in micro line and submicro

mesh openings, *2007 International Conference on Indium Phosphide and Related Materials, Conference Proceedings.*

Other publications

2. L. J. Martínez, I. Prieto, P. A. Postigo, Record quality factor on photonic crystal lasers fabricated on InP substrates, *Raith Application Note* 2010.

1. G. Santoro, I. Prieto–González, J. B. González–Díaz, L. J. Martínez, P. A. Postigo, Triangular air–hole based two–dimensional photonic crystal slabs design: a parametrical study, *Óptica Pura y Aplicada*, 40, 185 (2007).

In Preparation

4. I. Prieto, C. Robles, A. G. Taboada, J. M. Ripalda, L. E. Muñoz–Camúñez, and P. A. Postigo, Fabrication of high quality factor photonic crystal microcavities in GaAs and InP

3. I. Prieto, G. Muñoz–Matutano, C. Robles, J. Llorens, D. Fuster, J. P. Martínez–Pastor, and P. A. Postigo, Selective modal suppression of photonic crystal microcavity modes

2. I. Prieto, L. E. Muñoz–Camúñez, J. M. Llorens, A. G. Taboada, J. Canet–Ferrer, C. Robles, J. M. Ripalda, G. Muñoz–Matutano, J. Martínez–Pastor, and P. A. Postigo, Near thresholdless laser operation at room temperature

1. E. Pérez, J. Buencuerpo, I. Fernández, I. Prieto, B. Alén, A. Vitrey, A. García, J. M. Llorens, S. R. J. Brueck, J. M. Ripalda, Shadowless solar cell contacts

Bibliography

[1] R. P. Feynman. There is plenty of room at the bottom. *Technion Yearbook*, 19(29-33):137–141, 1962.

[2] Eli Yablonovitch. Inhibited spontaneous emission in solid-state physics and electronics. *Phys. Rev. Lett.*, 58(20):2059–2062, May 1987. Cited by 12278.

[3] Sajeev John. Strong localization of photons in certain disordered dielectric superlattices. *Phys. Rev. Lett.*, 58(23):2486–2489, June 1987.

[4] Axel Lorke, R. Johannes Luyken, Alexander O. Govorov, Jrg P. Kotthaus, J. M. Garcia, and P. M. Petroff. Spectroscopy of nanoscopic semiconductor rings. *Phys. Rev. Lett.*, 84(10):2223–2226, March 2000.

[5] Masahiro Nomura, Naoto Kumagai, Satoshi Iwamoto, Yasutomo Ota, and Yasuhiko Arakawa. Photonic crystal nanocavity laser with a single quantum dot gain. *Opt. Express*, 17(18):15975–15982, August 2009. 00000.

[6] Yoshihiro Akahane, Takashi Asano, Bong-Shik Song, and Susumu Noda. High-q photonic nanocavity in a two-dimensional photonic crystal. *Nature*, 425(6961):944–947, October 2003.

[7] S. Strauf, K. Hennessy, M. T. Rakher, Y.-S. Choi, A. Badolato, L. C. Andreani, E. L. Hu, P. M. Petroff, and D. Bouwmeester. Self-tuned quantum dot gain in photonic crystal lasers. *Phys. Rev. Lett.*, 96(12):127404, March 2006. Cited by 0359.

[8] K. Hennessy, A. Badolato, M. Winger, D. Gerace, M. Atatre, S. Gulde, S. Flt, E. L. Hu, and A. Imamolu. Quantum nature of a strongly coupled single quantum dotcavity system. *Nature*, 445(7130):896–899, February 2007.

[9] Bong-Shik Song, Susumu Noda, Takashi Asano, and Yoshihiro Akahane. Ultra-high-q photonic double-heterostructure nanocavity. *Nat Mater*, 4(3):207–210, March 2005.

[10] Eiichi Kuramochi, Masaya Notomi, Satoshi Mitsugi, Akihiko Shinya, Takasumi Tanabe, and Toshifumi Watanabe. Ultrahigh-q photonic crystal nanocavities realized by the local width modulation of a line defect. *Applied Physics Letters*, 88(4):041112, January 2006.

[11] Simon Frdrick, Dan Dalacu, Jean Lapointe, Philip J. Poole, Geof C. Aers, and Robin L. Williams. Experimental demonstration of high quality factor, x-dipole modes in InAsInP quantum dot photonic crystal microcavity membranes. *Applied Physics Letters*, 89(9):091115, August 2006. 00024.

[12] Masayuki Shirane, Shunsuke Kono, Jun Ushida, Shunsuke Ohkouchi, Naoki Ikeda, Yoshimasa Sugimoto, and Akihisa Tomita. Mode identification of high-quality-factor single-defect nanocavities in quantum dot-embedded photonic crystals. *Journal of Applied Physics*, 101(7):073107–073107–7, April 2007. Cited by 0042.

[13] A. Y. Cho. Film deposition by molecular-beam techniques. *Journal of Vacuum Science & Technology*, 8(5):S31–S38, September 1971.

[14] J. Sweet, B.C. Richards, J.D. Olitzky, J. Hendrickson, G. Khitrova, H.M. Gibbs, D. Litvinov, D. Gerthsen, D.Z. Hu, D.M. Schaadt, M. Wegener, U. Khankhoje, and A. Scherer. GaAs photonic crystal slab nanocavities: Growth, fabrication, and quality factor. *Photonics and Nanostructures - Fundamentals and Applications*, 8(1):1–6, January 2010. Cited by 0011.

[15] S. A. Rishton and D. P. Kern. Point exposure distribution measurements for proximity correction in electron beam lithography on a sub-100 nm scale. *Journal of Vacuum Science & Technology B: Microelectronics and Nanometer Structures*, 5(1):135–141, 1987.

[16] Ivn Prieto Gonzlez, Luis Enrique Muoz Camuez, Alfonso Gonzlez Taboada, Carmen Robles Urdiales, Jose Mara Ripalda Cobin, and Pablo Aitor Postigo Resa. Fabrication of high quality factor GaAs/InAsSb photonic crystal microcavities by inductively coupled plasma etching and fast wet etching.

Journal of Vacuum Science & Technology B, 32(1):011204, December 2013. 00000.

[17] T. Suhr, N. Gregersen, M. Lorke, and J. Mrk. Modulation response of quantum dot nanolight-emitting-diodes exploiting purcell-enhanced spontaneous emission. *Applied Physics Letters*, 98(21):211109–211109–3, May 2011.

[18] Susumu Noda. Seeking the ultimate nanolaser. *Science*, 314(5797):260–261, October 2006. PMID: 17038610.

[19] Masahiro Nomura, Satoshi Iwamoto, Katsuyuki Watanabe, Naoto Kumagai, Yoshiaki Nakata, Satomi Ishida, and Yasuhiko Arakawa. Room temperature continuous-wave lasing in photonic crystal nanocavity. *Opt. Express*, 14(13):6308–6315, June 2006.

[20] Luis Javier Martinez, Benito Aln, Ivan Prieto, David Fuster, Luisa Gonzlez, Yolanda Gonzlez, Mara Luisa Dotor, and Pablo A. Postigo. Room temperature continuous wave operation in a photonic crystalmicrocavity laser with a single layer of InAs/InP self-assembled quantum wires. *Opt. Express*, 17(17):14993–15000, August 2009.

[21] Kirill A. Atlasov, Milan Calic, Karl Fredrik Karlsson, Pascal Gallo, Alok Rudra, Benjamin Dwir, and Eli Kapon. Photonic-crystal microcavity laser with site-controlled quantum-wire active medium. *Opt. Express*, 17(20):18178–18183, September 2009. Cited by 0021.

[22] N. Gregersen, T. Suhr, M. Lorke, and J. Mrk. Quantum-dot nano-cavity lasers with purcell-enhanced stimulated emission. *Applied Physics Letters*, 100(13):131107–131107–4, March 2012. Cited by 0004.

[23] Xuetao Gan, Hannah Clevenson, Cheng-Chia Tsai, Luozhou Li, and Dirk Englund. Nanophotonic filters and integrated networks in flexible 2D polymer photonic crystals. *Sci. Rep.*, 3, July 2013.

[24] P. Michler, A. Kiraz, C. Becher, W. V. Schoenfeld, P. M. Petroff, Lidong Zhang, E. Hu, and A. Imamoglu. A quantum dot single-photon turnstile device. *Science*, 290(5500):2282–2285, December 2000. PMID: 11125136.

[25] A. Imamoglu, D. D. Awschalom, G. Burkard, D. P. DiVincenzo, D. Loss, M. Sherwin, and A. Small. Quantum information processing using quantum dot spins and cavity QED. *Phys. Rev. Lett.*, 83(20):4204–4207, November 1999.

[26] T. Yoshie, A. Scherer, J. Hendrickson, G. Khitrova, H. M. Gibbs, G. Rupper, C. Ell, O. B. Shchekin, and D. G. Deppe. Vacuum rabi splitting with a single quantum dot in a photonic crystal nanocavity. *Nature*, 432(7014):200–203, November 2004.

[27] Dirk Englund, Arka Majumdar, Andrei Faraon, Mitsuru Toishi, Nick Stoltz, Pierre Petroff, and Jelena Vukovi. Resonant excitation of a quantum dot strongly coupled to a photonic crystal nanocavity. *Phys. Rev. Lett.*, 104(7):073904, February 2010. Cited by 0080.

[28] M. Nomura, N. Kumagai, S. Iwamoto, Y. Ota, and Y. Arakawa. Laser oscillation in a strongly coupled single-quantum-dotnanocavity system. *Nature Physics*, 6(4):279–283, 2010. Cited by 0139.

[29] E. Gallardo, L. J. Martnez, A. K. Nowak, H. P. van der Meulen, J. M. Calleja, C. Tejedor, I. Prieto, D. Granados, A. G. Taboada, J. M. Garca, and P. A. Postigo. Emission polarization control in semiconductor quantum dots coupled to a photonic crystal microcavity. *Opt. Express*, 18(12):13301–13308, June 2010. Cited by 0006.

[30] M. Francardi, L. Balet, A. Gerardino, C. Monat, C. Zinoni, L. H. Li, B. Alloing, N. Le Thomas, R. Houdr, and A. Fiore. Quantum dot photonic crystal nanocavities at 1300 nm for telecom-wavelength single-photon sources. *physica status solidi (c)*, 3(11):36933696, 2006. Cited by 0029.

[31] M. Francardi, L. Balet, A. Gerardino, N. Chauvin, D. Bitauld, L. H. Li, B. Alloing, and A. Fiore. Enhanced spontaneous emission in a photonic-crystal light-emitting diode. *Applied Physics Letters*, 93(14):143102, October 2008.

[32] Yiyang Gong, Bryan Ellis, Gary Shambat, Tomas Sarmiento, James S. Harris, and Jelena Vuckovic. Nanobeam photonic crystal cavity quantum dot laser. *Opt. Express*, 18(9):8781–8789, April 2010. Cited by 0042.

[33] Kartik Srinivasan, Matthew Borselli, Oskar Painter, Andreas Stintz, and Sanjay Krishna. Cavity q, mode volume, and lasing threshold in small diameter AlGaAs microdisks with embedded quantum dots. *Opt. Express*, 14(3):1094–1105, February 2006. Cited by 0000.

[34] L. Balet, M. Francardi, A. Gerardino, N. Chauvin, B. Alloing, C. Zinoni, C. Monat, L. H. Li, N. Le Thomas, R. Houdre, and A. Fiore. Enhanced spontaneous emission rate from single InAs quantum dots in a photonic crystal nanocavity at telecom wavelengths. *Applied Physics Letters*, 91(12):123115, 2007. Cited by 0034.

[35] Masahiro Nomura, Satoshi Iwamoto, Naoto Kumagai, and Yasuhiko Arakawa. Temporal coherence of a photonic crystal nanocavity laser with high spontaneous emission coupling factor. *Phys. Rev. B*, 75(19):195313, May 2007.

[36] A. G. Taboada, A. M. Snchez, A. M. Beltrn, M. Bozkurt, D. Alonso-lvarez, B. Aln, A. Rivera, J. M. Ripalda, J. M. Llorens, J. Martn-Snchez, Y. Gonzlez, J. M. Ulloa, J. M. Garca, S. I. Molina, and P. M. Koenraad. Structural and optical changes induced by incorporation of antimony into InAs/GaAs(001) quantum dots. *Phys. Rev. B*, 82(23):235316, December 2010.

[37] A. G. Taboada, J. M. Llorens, D. Alonso-lvarez, B. Aln, A. Rivera, Y. Gonzlez, and J. M. Ripalda. Effect of sb incorporation on the electronic structure of InAs quantum dots. *Phys. Rev. B*, 88(8):085308, August 2013.

[38] J. M. Ripalda, D. Alonso-lvarez, B. Aln, A. G. Taboada, J. M. Garca, Y. Gonzlez, and L. Gonzlez. Enhancement of the room temperature luminescence of InAs quantum dots by GaSb capping. *Applied Physics Letters*, 91(1):012111–012111–3, July 2007.

[39] Lumerical solutions, inc, 2003.

[40] K. Hennessy, C. Reese, A. Badolato, C. F. Wang, A. Imamoglu, P. M. Petroff, and E. Hu. Fabrication of high q square-lattice photonic crystal microcavities. *Journal of Vacuum Science & Technology B: Microelectronics and Nanometer Structures*, 21(6):2918–2921, 2003. Cited by 0019.

[41] See www.raith.com for raith NanoPECS tool.

[42] L. J. Martinez, I Prieto, and P. A. Postigo. Record quality factors on photonic crystals lasers fabricated on InP substrates. *Raith Application Note*, 2010.

[43] Jos Ramn Sendra and Jos Anguita. Reactive ion beam etching of indium phosphide in electron cyclotron resonance plasma using Methane/Hydrogen/Nitrogen mixtures. *Japanese Journal of Applied Physics*, 33(Part 2, No. 3A):L390–L393, 1994. Cited by 0034.

[44] L. J. Martinez, I. Prieto, B. Alen, and P. A. Postigo. Fabrication of high quality factor photonic crystal microcavities in InAsP/InP membranes combining reactive ion beam etching and reactive ion etching. *Journal of Vacuum Science & Technology B: Microelectronics and Nanometer Structures*, 27(4):1801–1804, 2009.

[45] Kirill A. Atlasov, Pascal Gallo, Alok Rudra, Benjamin Dwir, and Eli Kapon. Effect of sidewall passivation in BCl[sub 3]/N[sub 2] inductively coupled plasma etching of two-dimensional GaAs photonic crystals. *Journal of Vacuum Science & Technology B: Microelectronics and Nanometer Structures*, 27(5):L21–L24, 2009. Cited by 0000.

[46] Andreas Kress, Felix Hofbauer, Norbert Reinelt, M. Kaniber, Max Bichler, Dieter Schuh, Gerhard Boehm, and Jonathan J. Finley. Fabrication and investigation of photonic crystal microcavities for solid state quantum optics. pages 114–124, April 2005. Cited by 0006.

[47] M. Asada, Y. Miyamoto, and Y. Suematsu. Gain and the threshold of three-dimensional quantum-box lasers. *IEEE Journal of Quantum Electronics*, 22(9):1915–1921, September 1986.

[48] Y. Arakawa and H. Sakaki. Multidimensional quantum well laser and temperature dependence of its threshold current. *Applied Physics Letters*, 40(11):939–941, June 1982. 03130.

[49] T. Yoshie, O.B. Shchekin, H. Chen, D.G. Deppe, and A. Scherer. Quantum dot photonic crystal lasers. *Electronics Letters*, 38(17):967–968, 2002.

[50] Larry A Coldren, Scott W Corzine, and Milan Mashanovitch. *Diode lasers and photonic integrated circuits*. Wiley, Hoboken, N.J., 2012. 02475.

[51] Shinji Matsuo, Akihiko Shinya, Takaaki Kakitsuka, Kengo Nozaki, Toru Segawa, Tomonari Sato, Yoshihiro Kawaguchi, and Masaya Notomi. High-speed ultracompact buried heterostructure photonic-crystal laser with 13fJ of energy consumed per bit transmitted. *Nat Photon*, 4(9):648–654, September 2010. 00108.

[52] M. Khajavikhan, A. Simic, M. Katz, J. H. Lee, B. Slutsky, A. Mizrahi, V. Lomakin, and Y. Fainman. Thresholdless nanoscale coaxial lasers. *Nature*, 482(7384):204–207, February 2012.

[53] O. Painter, J. Vu?kovi?, and A. Scherer. Defect modes of a two-dimensional photonic crystal in an optically thin dielectric slab. *J. Opt. Soc. Am. B*, 16(2):275–285, February 1999.

[54] Gunnar Bjrk, Anders Karlsson, and Yoshihisa Yamamoto. Definition of a laser threshold. *Phys. Rev. A*, 50(2):1675–1680, August 1994.

[55] F. De Martini and G. R. Jacobovitz. Anomalous spontaneousstimulated-decay phase transition and zero-threshold laser action in a microscopic cavity. *Phys. Rev. Lett.*, 60(17):1711–1714, April 1988. Cited by 0215.

[56] I. Protsenko, P. Domokos, V. Lefvre-Seguin, J. Hare, J. M. Raimond, and L. Davidovich. Quantum theory of a thresholdless laser. *Phys. Rev. A*, 59(2):1667–1682, February 1999.

[57] David A. B. Miller. Are optical transistors the logical next step? *Nat Photon*, 4(1):3–5, January 2010.

[58] Gary Shambat, Sri-Rajasekhar Kothapalli, J Provine, Tomas Sarmiento, James Harris, Sanjiv Sam Gambhir, and Jelena Vukovi. Single-cell photonic nanocavity probes. *Nano Lett.*, 13(11):4999–5005, 2013. 00002.

[59] Masahiro Nomura, Yasutomo Ota, Naoto Kumagai, Satoshi Iwamoto, and Yasuhiko Arakawa. Zero-cell photonic crystal nanocavity laser with quantum dot gain. *Applied Physics Letters*, 97(19):191108, November 2010. 00012.

[60] Se-Heon Kim, Guk-Hyun Kim, Sun-Kyung Kim, Hong-Gyu Park, Yong-Hee Lee, and Sung-Bock Kim. Characteristics of a stick waveguide resonator in a two-dimensional photonic crystal slab. *Journal of Applied Physics*, 95(2):411–416, January 2004. Cited by 0038.

[61] M. Geller, A. Marent, T. Nowozin, D. Bimberg, N. Akay, and N. ncan. A write time of 6ns for quantum dotbased memory structures. *Applied Physics Letters*, 92(9):092108, March 2008.

[62] W. Lei, M. Offer, A. Lorke, C. Notthoff, C. Meier, O. Wibbelhoff, and A. D. Wieck. Probing the band structure of InAsGaAs quantum dots by capacitance-voltage and photoluminescence spectroscopy. *Applied Physics Letters*, 92(19):193111, May 2008.

[63] Y. T. Dai, J. C. Fan, Y. F. Chen, R. M. Lin, S. C. Lee, and H. H. Lin. Temperature dependence of photoluminescence spectra in InAs/GaAs quantum dot superlattices with large thicknesses. *Journal of Applied Physics*, 82(9):4489–4492, November 1997. 00117.

[64] S. Sanguinetti, M. Henini, M. Grassi Alessi, M. Capizzi, P. Frigeri, and S. Franchi. Carrier thermal escape and retrapping in self-assembled quantum dots. *Phys. Rev. B*, 60(11):8276–8283, September 1999. 00291.

[65] J. Canet-Ferrer, I. Prieto, G. Muoz-Matutano, L. J. Martnez, L. E. Muoz-Camuniez, J. M. Llorens, D. Fuster, B. Aln, Y. Gonzlez, L. Gonzlez, P. A. Postigo, and J. P. Martnez-Pastor. Excitation power dependence of the purcell effect in photonic crystal microcavity lasers with quantum wires. *Applied Physics Letters*, 102(20):201105–201105–4, May 2013.

[66] Gunnar Bjrk, Anders Karlsson, and Yoshihisa Yamamoto. On the linewidth of microcavity lasers. *Applied Physics Letters*, 60(3):304, January 1992.

[67] Bryan Ellis, Marie A. Mayer, Gary Shambat, Tomas Sarmiento, James Harris, Eugene E. Haller, and Jelena Vukovi. Ultralow-threshold electrically pumped quantum-dot photonic-crystal nanocavity laser. *Nat Photon*, 5(5):297–300, May 2011. 00128.

[68] Jose M. Llorens, Ivan Prieto, Luis E. Munioz-Camuniez, and Pablo Aitor Postigo. Analysis of the strong coupling regime of a quantum well in a

photonic crystal microcavity and its polarization dependence studied by the finite-difference time-domain method. *J. Opt. Soc. Am. B*, 30(5):1222–1231, May 2013. Cited by 0000.

[69] R. Coccioli, M. Boroditsky, K. W. Kim, Y. Rahmat-Samii, and E. Yablonovitch. Smallest possible electromagnetic mode volume in a dielectric cavity. *Optoelectronics, IEE Proceedings* -, 145(6):391–397, 1998.

[70] Kevin Hennessy. *Photonic Crystal Nanocavities Positioned and Tuned for Cavity-QED*. PhD thesis, University of California Santa Barbara, June 2006.

[71] Kartik Srinivasan, Paul E. Barclay, Oskar Painter, Jianxin Chen, Alfred Y. Cho, and Claire Gmachl. Experimental demonstration of a high quality factor photonic crystal microcavity. *Applied Physics Letters*, 83(10):1915–1917, September 2003.

[72] Atlasov Atlasov. *Light Control and Microcavity Lasers Based on Quantum Wires Integrated in Photonic-Crystal Cavities*. PhD thesis, COLE POLYTECHNIQUE FDRALE DE LAUSANNE, Switzerland, 2009.

[73] M. P. van Exter, G. Nienhuis, and J. P. Woerdman. Two simple expressions for the spontaneous emission factor . *Phys. Rev. A*, 54(4):3553–3558, October 1996. 00049.

[74] M. Bayer and A. Forchel. Temperature dependence of the exciton homogeneous linewidth in in_{0.60}ga_{0.40}As/GaAs self-assembled quantum dots. *Phys. Rev. B*, 65(4):041308, January 2002. 00389.

[75] Allen Taflove and Susan C. Hagness. *Computational Electrodynamics: The Finite-Difference Time-Domain Method*. Artech House, 2000.

[76] Josep Canet-Ferrer, Luis J. Martnez, Ivan Prieto, Benito Aln, Guillermo Muoz-Matutano, David Fuster, Yolanda Gonzlez, Mara L. Dotor, Luisa Gonzlez, Pablo A. Postigo, and Juan P. Martnez-Pastor. Purcell effect in photonic crystal microcavities embedding InAs/InP quantum wires. *Opt. Express*, 20(7):7901–7914, March 2012. Cited by 0001.

[77] C. Weisbuch, M. Nishioka, A. Ishikawa, and Y. Arakawa. Observation of the coupled exciton-photon mode splitting in a semiconductor quantum microcavity. *Phys. Rev. Lett.*, 69(23):3314–3317, December 1992.

[78] Benoit Deveaud, editor. *The Physics of Semiconductor Microcavities: From Fundamentals to Nanoscale Devices*. Wiley-VCH Verlag GmbH & Co. KGaA, February 2007.

[79] daniele sanvitto and vladislav timofeev. *Exciton Polaritons in Microcavities - New Frontiers*, volume 172 of *Springer Series in Solid-State Sciences*. 2012.

[80] Dario Gerace, Mario Agio, and Lucio Claudio Andreani. Quantum theory of photonic crystal polaritons. *phys. stat. sol. (c)*, 1(3):446–449, February 2004.

[81] M. Sugawara, T. Fujii, S. Yamazaki, and K. Nakajima. Optical characteristics of excitons in in1-xGaxAsyP1-y/InP quantum wells. *Phys. Rev. B*, 44(4):1782–1791, July 1991.

[82] Y. Sidor, B. Partoens, F. M. Peeters, J. Maes, M. Hayne, D. Fuster, Y. Gonzlez, L. Gonzlez, and V. V. Moshchalkov. Exciton confinement in InAsInP quantum wires and quantum wells in the presence of a magnetic field. *Phys. Rev. B*, 76(19):195320, November 2007.

[83] T. Gutbrod, M. Bayer, A. Forchel, J. P. Reithmaier, T. L. Reinecke, S. Rudin, and P. A. Knipp. Weak and strong coupling of photons and excitons in photonic dots. *Phys. Rev. B*, 57(16):9950–9956, April 1998.

[84] Giovanna Panzarini and Lucio Claudio Andreani. Quantum theory of exciton polaritons in cylindrical semiconductor microcavities. *Phys. Rev. B*, 60(24):16799–16806, December 1999.

[85] R. Houdr, C. Weisbuch, R. P. Stanley, U. Oesterle, P. Pellandini, and M. Ilegems. Measurement of cavity-polariton dispersion curve from angle-resolved photoluminescence experiments. *Phys. Rev. Lett.*, 73(15):2043–2046, October 1994.

[86] R. Houdr, R. P. Stanley, U. Oesterle, M. Ilegems, and C. Weisbuch. Room-temperature cavity polaritons in a semiconductor microcavity. *Phys. Rev. B*, 49(23):16761–16764, June 1994.

[87] E. L. Ivchenko and G. Pikus. *Superlattices and Other Heterostructures: Symmetry and Optical Phenomena*. Number 978-3-642-64493-1. Springer Series in Solid-State Sciences, 1997.

[88] R. Shimada, A.L. Yablonskii, S.G. Tikhodeev, and T. Ishihara. Transmission properties of a two-dimensional photonic crystal slab with an excitonic resonance. *IEEE Journal of Quantum Electronics*, 38(7):872–879, July 2002.

[89] Lucio Claudio Andreani, Dario Gerace, and Mario Agio. Exciton-polaritons and nanoscale cavities in photonic crystal slabs. *phys. stat. sol. (b)*, 242(11):2197–2209, September 2005.

[90] Marco Liscidini, Dario Gerace, Daniele Sanvitto, and Daniele Bajoni. Guided bloch surface wave polaritons. *Applied Physics Letters*, 98(12):121118, March 2011.

[91] G. Tarel and V. Savona. Linear spectrum of a quantum dot coupled to a nanocavity. *Phys. Rev. B*, 81(7):075305, February 2010.

[92] S. Hughes and H. Kamada. Single-quantum-dot strong coupling in a semiconductor photonic crystal nanocavity side coupled to a waveguide. *Phys. Rev. B*, 70(19):195313, November 2004. Cited by 0046.

[93] L. A. Dunbar, R. P. Stanley, M. Lynch, J. Hegarty, U. Oesterle, R. Houdr, and M. Ilegems. Excitation-induced coherence in a semiconductor microcavity. *Phys. Rev. B*, 66(19):195307, November 2002.

[94] M. S. Skolnick, P. R. Tapster, S. J. Bass, A. D. Pitt, N. Apsley, and S. P. Aldred. Investigation of InGaAs-InP quantum wells by optical spectroscopy. *Semicond. Sci. Technol.*, 1(1):29, July 1986.

[95] M. S. Skolnick, K. J. Nash, M. K. Saker, S. J. Bass, P. A. Claxton, and J. S. Roberts. Freecarrier effects on luminescence linewidths in quantum wells. *Applied Physics Letters*, 50(26):1885–1887, June 1987.

[96] J. Vuckovic, O. Painter, Yong Xu, A. Yariv, and Axel Scherer. Finite-difference time-domain calculation of the spontaneous emission coupling factor in optical microcavities. *IEEE Journal of Quantum Electronics*, 35(8):1168–1175, August 1999.

[97] G.M. Slavcheva, J.M. Arnold, and R.W. Ziolkowski. FDTD simulation of the nonlinear gain dynamics in active optical waveguides and semiconductor microcavities. *IEEE Journal of Selected Topics in Quantum Electronics*, 10(5):1052–1062, September 2004.

[98] Hideaki Taniyama, Hisashi Sumikura, and Masaya Notomi. Finite-difference time-domain analysis of photonic crystal slab cavities with two-level systems. *Opt. Express*, 19(23):23067–23077, November 2011.

[99] Vladimir A. Mandelshtam and Howard S. Taylor. Harmonic inversion of time signals and its applications. *The Journal of Chemical Physics*, 107(17):6756–6769, November 1997.

[100] V. Savona, Z. Hradil, A. Quattropani, and P. Schwendimann. Quantum theory of quantum-well polaritons in semiconductor microcavities. *Phys. Rev. B*, 49(13):8774–8779, April 1994.

[101] A Kavokin and G. Malpuech. *Cavity polaritons*. Academic Press, 2003.

[102] K Cho. *Optical Response of Nanostructures - Microscopic Nonlocal Theory*. 2003.

[103] Yifu Zhu, Daniel J. Gauthier, S. E. Morin, Qilin Wu, H. J. Carmichael, and T. W. Mossberg. Vacuum rabi splitting as a feature of linear-dispersion theory: Analysis and experimental observations. *Phys. Rev. Lett.*, 64(21):2499–2502, May 1990.

[104] Lucio Claudio Andreani. Exciton-polaritons in superlattices. *Physics Letters A*, 192(1):99–109, August 1994.

[105] Daniele Bajoni. Polariton lasers. hybrid lightmatter lasers without inversion. *J. Phys. D: Appl. Phys.*, 45(31):313001, August 2012. Cited by 0005.

[106] Benoit Deveaud-Pldran. On the condensation of polaritons. *J. Opt. Soc. Am. B*, 29(2):A138–A145, February 2012.

[107] R. P. Stanley, S. Pau, U. Oesterle, R. Houdr, and M. Ilegems. Resonant photoluminescence of semiconductor microcavities:The role of acoustic phonons in polariton relaxation. *Phys. Rev. B*, 55(8):R4867–R4870, February 1997.

[108] G. Cassabois, A. L. C. Triques, F. Bogani, C. Delalande, Ph. Roussignol, and C. Piermarocchi. Polaritonacoustic-phonon interaction in a semiconductor microcavity. *Phys. Rev. B*, 61(3):1696–1699, January 2000.

[109] H. M. Gibbs, G. Khitrova, and S. W. Koch. Exciton-polariton light-semiconductor coupling effects. *Nat Photon*, 5(5):273–273, May 2011.

[110] M. Kira and S. W. Koch. Many-body correlations and excitonic effects in semiconductor spectroscopy. *Progress in Quantum Electronics*, 30(5):155–296, 2006.

[111] Klaus Bhringer and Ortwin Hess. A full-time-domain approach to spatio-temporal dynamics of semiconductor lasers. i. theoretical formulation. *Progress in Quantum Electronics*, 32(56):159–246, 2008.

[112] Shih-Hui Chang and Allen Taflove. Finite-difference time-domain model of lasing action in a four-level two-electron atomic system. *Opt. Express*, 12(16):3827–3833, August 2004.

[113] Yingyan Huang and Seng-Tiong Ho. Computational model of solid-state, molecular, or atomic media for FDTD simulation based on a multi-level multi-electron system governed by pauli exclusion and fermi-dirac thermalization with application to semiconductor photonics. *Opt. Express*, 14(8):3569–3587, April 2006.

[114] S. G. Johnson. Harminv.

[115] J. Brest, S. Greiner, B. Boskovic, M. Mernik, and V. Zumer. Self-adapting control parameters in differential evolution: A comparative study on numerical benchmark problems. *IEEE Transactions on Evolutionary Computation*, 10(6):646–657, December 2006.

[116] Francesco Biscani, Dario Izzo, and Chit Hong Yam. A global optimisation toolbox for massively parallel engineering optimisation. *arXiv:1004.3824 [cs, math]*, April 2010.

[117] E. Palik. *Handbook of Optical Constants of Solids*. Number 978-0-12-544415-6. Academic Press Handbook Series, 1985.

[118] D. Bajoni, D. Gerace, M. Galli, J. Bloch, R. Braive, I. Sagnes, A. Miard, A. Lematre, M. Patrini, and L. C. Andreani. Exciton polaritons in two-dimensional photonic crystals. *Phys. Rev. B*, 80(20):201308, November 2009.

[119] Stefano Azzini, Dario Gerace, Matteo Galli, Isabelle Sagnes, Rmy Braive, Aristide Lematre, Jacqueline Bloch, and D. Bajoni. Ultra-low threshold polariton lasing in photonic crystal cavities. *Applied Physics Letters*, 99(11):111106–111106–3, September 2011. Cited by 0014.

[120] Yejin Zhang, Wanhua Zheng, Mingxin Xing, Gang Ren, Hailing Wang, and LiangHui Chen. Application of fast pade approximation in simulating photonic crystal nanocavities by FDTD technology. *Optics Communications*, 281(10):2774–2778, May 2008.

[121] A Kavokin and G. Malpuech. *Thin Films and Nanostructures: Cavity polaritons*, volume 32. Elsevier, 2010.

[122] Fabrice P. Laussy, Elena del Valle, and Carlos Tejedor. Luminescence spectra of quantum dots in microcavities. i. bosons. *Phys. Rev. B*, 79(23):235325, June 2009.

[123] Claude Cohen-Tannoudji, Bernard Diu, and Frank Laloe. *Quantum Mechanics*, volume 1. Wiley, 1992.

[124] R. Houdr, R. P. Stanley, U. Oesterle, M. Ilegems, and C. Weisbuch. Room temperature exciton-photon rabi splitting in a semiconductor microcavity. *Le Journal de Physique IV*, 03(C5):51–58, October 1993.

[125] Claude Weisbuch and Borge Vinter. *Quantum Semiconductor Structures: Fundamentals and Applications*. 1991.

[126] C. F. Wang, R. Hanson, D. D. Awschalom, E. L. Hu, T. Feygelson, J. Yang, and J. E. Butler. Fabrication and characterization of two-dimensional photonic crystal microcavities in nanocrystalline diamond. *Applied Physics Letters*, 91(20):201112–201112–3, November 2007. Cited by 0155.

[127] Thomas Snner, Christian Schneider, Micha Strau, Alexander Huggenberger, Daniel Wiener, Sven Hfling, Martin Kamp, and Alfred Forchel. Scalable fabrication of optical resonators with embedded site-controlled quantum dots. *Opt. Lett.*, 33(15):1759–1761, August 2008. Cited by 0032.

[128] Susanna M. Thon, Matthew T. Rakher, Hyochul Kim, Jan Gudat, William T. M. Irvine, Pierre M. Petroff, and Dirk Bouwmeester. Strong coupling through optical positioning of a quantum dot in a photonic crystal cavity. *Applied Physics Letters*, 94(11):111115, March 2009.

[129] D. Sarkar, L.J. Martnez, I. Prieto-Gonzlez, H.P. van der Meulen, J.M. Calleja, D. Granados, A.G. Taboada, J.M. Garca, A.R. Alija, and P.A. Postigo. Optical emission of InAs/GaAs quantum rings coupled to a two-dimensional photonic crystal microcavity. *Physica E: Low-dimensional Systems and Nanostructures*, 40(6):2156–2159, April 2008. Cited by 0000.

[130] E. Gallardo, L. J. Martnez, A. K. Nowak, D. Sarkar, H. P. van der Meulen, J. M. Calleja, C. Tejedor, I. Prieto, D. Granados, A. G. Taboada, J. M. Garca, and P. A. Postigo. Optical coupling of two distant InAs/GaAs quantum dots by a photonic-crystal microcavity. *Phys. Rev. B*, 81(19):193301, May 2010.

[131] E. Gallardo, L. J. Martnez, A. K. Nowak, D. Sarkar, D. Sanvitto, H. P. van der Meulen, J. M. Calleja, I. Prieto, D. Granados, A. G. Taboada, J. M. Garca, and P. A. Postigo. Single-photon emission by semiconductor quantum rings in a photonic crystal. *J. Opt. Soc. Am. B*, 27(6):A21–A24, June 2010.

[132] M. Maragkou, A. K. Nowak, E. Gallardo, H. P. van der Meulen, I. Prieto, L. J. Martinez, P. A. Postigo, and J. M. Calleja. Controlling the properties of single photon emitters via the purcell effect. *Phys. Rev. B*, 86(8):085316, August 2012. Cited by 0000.

[133] M. Maragkou, C. Snchez-Muoz, S. Lazi, E. Chernysheva, H. P. van der Meulen, A. Gonzlez-Tudela, C. Tejedor, L. J. Martnez, I. Prieto, P. A. Postigo, and J. M. Calleja. Bichromatic dressing of a quantum dot detected by a remote second quantum dot. *Phys. Rev. B*, 88(7):075309, August 2013. 00000.

[134] Antonio Badolato, Kevin Hennessy, Mete Atatre, Jan Dreiser, Evelyn Hu, Pierre M. Petroff, and Atac Imamolu. Deterministic coupling of single quantum dots to single nanocavity modes. *Science*, 308(5725):1158–1161, May 2005. PMID: 15905398.

[135] J. Martin-Sanchez, G. Munoz-Matutano, J. Herranz, J. Canet-Ferrer, B. Alen, Y. Gonzalez, P. Alonso-Gonzalez, D. Fuster, L. Gonzalez, J. Martinez-Pastor, and F. Briones. Single photon emission from site-controlled InAs quantum dots grown on GaAs(001) patterned substrates. *ACS Nano*, 3(6):1513–1517, June 2009.

[136] C. Schneider, T. Heindel, A. Huggenberger, P. Weinmann, C. Kistner, M. Kamp, S. Reitzenstein, S. Hfling, and A. Forchel. Single photon emission from a site-controlled quantum dot-micropillar cavity system. *Applied Physics Letters*, 94(11):111111, March 2009.

[137] A. Imamolu, S. Flt, J. Dreiser, G. Fernandez, M. Atatre, K. Hennessy, A. Badolato, and D. Gerace. Coupling quantum dot spins to a photonic crystal nanocavitya). *Journal of Applied Physics*, 101(8):081602, April 2007.

[138] Matthew Borselli, Thomas Johnson, and Oskar Painter. Beyond the rayleigh scattering limit in high-q silicon microdisks: theory and experiment. *Opt. Express*, 13(5):1515–1530, March 2005. 00252.

[139] K. Hennessy, A. Badolato, P. M. Petroff, and E. Hu. Positioning photonic crystal cavities to single InAs quantum dots. *Photonics and Nanostructures - Fundamentals and Applications*, 2(2):65–72, October 2004.

[140] J. Martn-Snchez, P. Alonso-Gonzlez, J. Herranz, Y. Gonzlez, and L. Gonzlez. Site-controlled lateral arrangements of InAs quantum dots grown on GaAs(001) patterned substrates by atomic force microscopy local oxidation nanolithography. *Nanotechnology*, 20(12):125302, March 2009. Cited by 0011.

[141] J. Martn-Snchez, Y. Gonzlez, P. Alonso-Gonzlez, and L. Gonzlez. Improvement of InAs quantum dots optical properties in close proximity to GaAs(001) substrate surface. *Journal of Crystal Growth*, 310(22):4676–4680, November 2008.

[142] P. A. Postigo, C. G. Fonstad Jr, S. Choi, and W. D. Goodhue. Solid-source molecular-beam epitaxy for monolithic integration of laser emitters and photodetectors on GaAs chips. *Applied Physics Letters*, 77(23):3842–3844, December 2000.

[143] F. Briones, L. Gonzlez, and A. Ruiz. Atomic layer molecular beam epitaxy (almbe) of IIIV compounds: Growth modes and applications. *Appl. Phys. A*, 49(6):729–737, December 1989. Cited by 0127.

[144] Shigeru Kohmoto, Hitoshi Nakamura, Tomonori Ishikawa, Satoshi Nishikawa, Tetsuya Nishimura, and Kiyoshi Asakawa. Site-controlled self-organization of InAs quantum dots. *Materials Science and Engineering: B*, 88(23):292–297, January 2002.

[145] K. A. Atlasov, K. F. Karlsson, E. Deichsel, A. Rudra, B. Dwir, and E. Kapon. Site-controlled single quantum wire integrated into a photonic-crystal membrane microcavity. *Applied Physics Letters*, 90(15):153107, April 2007.

[146] I. J. Luxmoore, E. D. Ahmadi, N. A. Wasley, A. M. Fox, A. I. Tartakovskii, A. B. Krysa, and M. S. Skolnick. Control of spontaneous emission from InP single quantum dots in GaInP photonic crystal nanocavities. *Applied Physics Letters*, 97(18):181104–181104–3, November 2010.

[147] Susumu Noda, Masayuki Fujita, and Takashi Asano. Spontaneous-emission control by photonic crystals and nanocavities. *Nat Photon*, 1(8):449–458, August 2007. Cited by 0410.

[148] David Fattal, Kyo Inoue, Jelena Vukovi, Charles Santori, Glenn S. Solomon, and Yoshihisa Yamamoto. Entanglement formation and violation of bells inequality with a semiconductor single photon source. *Phys. Rev. Lett.*, 92(3):037903, January 2004. Cited by 0125.

[149] Arne L. Grimsmo and Scott Parkins. Cavity-QED simulation of qubit-oscillator dynamics in the ultrastrong-coupling regime. *Phys. Rev. A*, 87(3):033814, March 2013.

[150] A. Laucht, J. M. Villas-Bas, S. Stobbe, N. Hauke, F. Hofbauer, G. Bhm, P. Lodahl, M.-C. Amann, M. Kaniber, and J. J. Finley. Mutual coupling

of two semiconductor quantum dots via an optical nanocavity. *Phys. Rev. B*, 82(7):075305, August 2010. Cited by 0035.

[151] Andrei Faraon, Arka Majumdar, Hyochul Kim, Pierre Petroff, and Jelena Vukovi. Fast electrical control of a quantum dot strongly coupled to a photonic-crystal cavity. *Phys. Rev. Lett.*, 104(4):047402, January 2010. Cited by 0047.

[152] J. M. Grard, B. Sermage, B. Gayral, B. Legrand, E. Costard, and V. Thierry-Mieg. Enhanced spontaneous emission by quantum boxes in a monolithic optical microcavity. *Phys. Rev. Lett.*, 81(5):1110–1113, August 1998. Cited by 0782.

[153] Dirk Englund, David Fattal, Edo Waks, Glenn Solomon, Bingyang Zhang, Toshihiro Nakaoka, Yasuhiko Arakawa, Yoshihisa Yamamoto, and Jelena Vukovi. Controlling the spontaneous emission rate of single quantum dots in a two-dimensional photonic crystal. *Phys. Rev. Lett.*, 95(1):013904, July 2005.

[154] P. Atkinson, M.B. Ward, S.P. Bremner, D. Anderson, T. Farrow, G.A.C. Jones, A.J. Shields, and D.A. Ritchie. Site control of InAs quantum dot nucleation by ex situ electron-beam lithographic patterning of GaAs substrates. *Physica E: Low-dimensional Systems and Nanostructures*, 32(12):21–24, May 2006. Cited by 0020.

[155] John Stephen Smith, Pamela L. Derry, Shlomo Margalit, and Amnon Yariv. High quality molecular beam epitaxial growth on patterned GaAs substrates. *Applied Physics Letters*, 47(7):712–715, October 1985. Cited by 0078.

[156] Hideki Watanabe and Toshihiko Baba. High-efficiency photonic crystal microlaserintegrated with a passive waveguide. *Opt. Express*, 16(4):2694–2698, February 2008. Cited by 0000.

[157] Adam C. Scofield, Se-Heon Kim, Joshua N. Shapiro, Andrew Lin, Baolai Liang, Axel Scherer, and Diana L. Huffaker. Bottom-up photonic crystal lasers. *Nano Lett.*, 11(12):5387–5390, December 2011. Cited by 0014.

[158] David M. Williams, Kristian M. Groom, Ben J. Stevens, David T. D. Childs, Richard J. E. Taylor, Salam Khamas, Richard A. Hogg, Naoki Ikeda, and Yoshimasa Sugimoto. Optimisation of coupling between photonic crystal and active elements in an epitaxially regrown GaAs based photonic crystal surface emitting laser. *Japanese Journal of Applied Physics*, 51(2):02BG05, 2012.

[159] Ganapathi Subramania, Qiming Li, Yun-Ju Lee, Jeffrey J. Figiel, George T. Wang, and Arthur J. Fischer. Gallium nitride based logpile photonic crystals. *Nano Lett.*, 11(11):4591–4596, November 2011. Cited by 0007.

[160] Erik C. Nelson, Neville L. Dias, Kevin P. Bassett, Simon N. Dunham, Varun Verma, Masao Miyake, Pierre Wiltzius, John A. Rogers, James J. Coleman, Xiuling Li, and Paul V. Braun. Epitaxial growth of three-dimensionally architectured optoelectronic devices. *Nat Mater*, 10(9):676–681, September 2011.

[161] M. Arita, S. Ishida, S. Kako, S. Iwamoto, and Y. Arakawa. AlN air-bridge photonic crystal nanocavities demonstrating high quality factor. *Applied Physics Letters*, 91(5):051106–051106–3, July 2007.

[162] D. Neel, S. Sergent, M. Mexis, D. Sam-Giao, T. Guillet, C. Brimont, T. Bretagnon, F. Semond, B. Gayral, S. David, X. Checoury, and P. Boucaud. AlN photonic crystal nanocavities realized by epitaxial conformal growth on nanopatterned silicon substrate. *Applied Physics Letters*, 98(26):261106, 2011. Cited by 0013.

[163] A. Khatiri, T.J. Krzyzewski, C.F. McConville, and T.S. Jones. Atomic hydrogen cleaning of low-index GaAs surfaces. *Journal of Crystal Growth*, 282(12):1–6, August 2005.

[164] Xu-Qiang Shen and Tatau Nishinaga. Arsenic pressure dependence of the surface diffusion in molecular beam epitaxy on (111)B-(001) mesa-etched GaAs substrates studied by *In Situ* scanning microprobe reflection high-energy electron diffraction. *Japanese Journal of Applied Physics*, 32(Part 2, No. 8B):L1117–L1119, 1993. Cited by 0000.

[165] S. Koshiba, Y. Nakamura, M. Tsuchiya, H. Noge, H. Kano, Y. Nagamune, T. Noda, and H. Sakaki. Surface diffusion processes in molecular beam

epitaxial growth of GaAs and AlAs as studied on GaAs (001)(111)B facet structures. *Journal of Applied Physics*, 76(7):4138–4144, October 1994.

[166] H Heidemeyer, C Mller, and O.G Schmidt. Highly ordered arrays of in(Ga)As quantum dots on patterned GaAs(001) substrates. *Journal of Crystal Growth*, 261(4):444–449, February 2004. Cited by 0000.

[167] A. R. Alija, L. J. Martnez, A. Garca-Martn, M. L. Dotor, D. Golmayo, and P. A. Postigo. Tuning of spontaneous emission of two-dimensional photonic crystal microcavities by accurate control of slab thickness. *Applied Physics Letters*, 86(14):141101–141101–3, March 2005. Cited by 0009.

[168] Zhenyu Yuan, Joseph Haus, and Kazuaki Sakoda. Eigenmode symmetry for simple cubic lattices and the transmission spectra. *Optics Express*, 3(1):19–27, July 1998. Cited by 0011.

[169] Sei-ichi Takayama, Hitoshi Kitagawa, Yoshinori Tanaka, Takashi Asano, and Susumu Noda. Experimental demonstration of complete photonic band gap in two-dimensional photonic crystal slabs. *Applied Physics Letters*, 87(6):061107–061107–3, August 2005.

[170] Lucio Claudio Andreani and Dario Gerace. Photonic-crystal slabs with a triangular lattice of triangular holes investigated using a guided-mode expansion method. *Phys. Rev. B*, 73(23):235114, June 2006. Cited by 0109.

[171] A. Laucht, F. Hofbauer, N. Hauke, J. Angele, S. Stobbe, M. Kaniber, G. Bhm, P. Lodahl, M.-C. Amann, and J. J. Finley. Electrical control of spontaneous emission and strong coupling for a single quantum dot. *New J. Phys.*, 11(2):023034, February 2009.

[172] Hyochul Kim, Deepak Sridharan, Thomas C. Shen, Glenn S. Solomon, and Edo Waks. Strong coupling between two quantum dots and a photonic crystal cavity using magnetic field tuning. *Opt. Express*, 19(3):2589–2598, January 2011.

[173] Ryuichi Ohta, Yasutomo Ota, Masahiro Nomura, Naoto Kumagai, Satomi Ishida, Satoshi Iwamoto, and Yasuhiko Arakawa. Strong coupling between a photonic crystal nanobeam cavity and a single quantum dot. *Applied Physics Letters*, 98(17):173104, April 2011.

[174] P Alonso-Gonzlez, L Gonzlez, D Fuster, J Martn-Snchez, and Yolanda Gonzlez. Surface localization of buried III-V semiconductor nanostructures. *Nanoscale Res Lett*, 4(8):873–877, 2009. PMID: 20596455 PMCID: PMC2893929.

[175] J. P. Reithmaier, G. Sk, A. Lffler, C. Hofmann, S. Kuhn, S. Reitzenstein, L. V. Keldysh, V. D. Kulakovskii, T. L. Reinecke, and A. Forchel. Strong coupling in a single quantum dotsemiconductor microcavity system. *Nature*, 432(7014):197–200, November 2004.

[176] A. Dousse, L. Lanco, J. Suffczyski, E. Semenova, A. Miard, A. Lematre, I. Sagnes, C. Roblin, J. Bloch, and P. Senellart. Controlled light-matter coupling for a single quantum dot embedded in a pillar microcavity using far-field optical lithography. *Phys. Rev. Lett.*, 101(26):267404, December 2008.

[177] Ivan Prieto, Jess Herranz, Lukasz Wewior, Yolanda Gonzlez, Benito Aln, Luisa Gonzlez, and Pablo A. Postigo. High quality factor GaAs-based photonic crystal microcavities by epitaxial re-growth. *Opt. Express*, 21(25):31615–31622, December 2013.

[178] I. Prieto, J. Herranz, Y. Gonzalez, J. Canet-Ferrer, L. Wewior, P.A. Postigo, B. Alen, L. Gonzalez, M. Kaldirim, L. Munioz-Camuniez, D. Fuster, A. G. Taboada, J. M. Ripalda, F. Briones, G. Munoz-Matutano, and J. Martinez-Pastor. Different strategies towards the deterministic coupling of a single quantum dot to a photonic crystal cavity mode. In *2011 13th International Conference on Transparent Optical Networks (ICTON)*, pages 1–5, 2011. 00000.

[179] Pablo Alonso-Gonzlez, Luisa Gonzlez, David Fuster, Yolanda Gonzlez, Alfonso G. Taboada, Jos Mara Ripalda, Ana M. Beltrn, David L. Sales, Teresa Ben, and Sergio I. Molina. Formation of spatially addressed ga(As)Sb quantum rings on GaAs(001) substrates by droplet epitaxy. *Crystal Growth & Design*, 9(2):1216–1218, February 2009.

[180] P. Alonso-Gonzlez, B. Aln, D. Fuster, Y. Gonzlez, L. Gonzlez, and J. Martnez-Pastor. Formation and optical characterization of single InAs quantum dots grown on GaAs nanoholes. *Applied Physics Letters*, 91(16):163104, October 2007.

[181] Y.-S. Choi, K. Hennessy, R. Sharma, E. Haberer, Y. Gao, S. P. DenBaars, S. Nakamura, E. L. Hu, and C. Meier. GaN blue photonic crystal membrane nanocavities. *Applied Physics Letters*, 87(24):243101–243101–3, December 2005. Cited by 0072.

[182] K. Hennessy, A. Badolato, A. Tamboli, P. M. Petroff, E. Hu, M. Atatre, J. Dreiser, and A. Imamolu. Tuning photonic crystal nanocavity modes by wet chemical digital etching. *Applied Physics Letters*, 87(2):021108–021108–3, July 2005. Cited by 0101.

[183] K. Hennessy, C. Hgerle, E. Hu, A. Badolato, and A. Imamolu. Tuning photonic nanocavities by atomic force microscope nano-oxidation. *Applied Physics Letters*, 89(4):041118–041118–3, July 2006. Cited by 0091.

[184] Michael Gehl, Ricky Gibson, Joshua Hendrickson, Andrew Homyk, Antti Syntjoki, Tapani Alasaarela, Lasse Karvonen, Ari Tervonen, Seppo Honkanen, Sander Zandbergen, Benjamin C. Richards, J. D. Olitzky, Axel Scherer, Galina Khitrova, Hyatt M. Gibbs, Ju-Young Kim, and Yong-Hee Lee. Effect of atomic layer deposition on the quality factor of silicon nanobeam cavities. *J. Opt. Soc. Am. B*, 29(2):A55–A59, February 2012.

[185] S. Mosor, J. Hendrickson, B. C. Richards, J. Sweet, G. Khitrova, H. M. Gibbs, T. Yoshie, A. Scherer, O. B. Shchekin, and D. G. Deppe. Scanning a photonic crystal slab nanocavity by condensation of xenon. *Applied Physics Letters*, 87(14):141105, October 2005.

[186] K. Ohtaka. Energy band of photons and low-energy photon diffraction. *Phys. Rev. B*, 19(10):5057–5067, May 1979.

[187] A. Mihi, M. E. Calvo, J. A. Anta, and H. Mguez. Spectral response of opal-based dye-sensitized solar cells. *J. Phys. Chem. C*, 112(1):13–17, January 2008.

[188] Peter Bermel, Chiyan Luo, Lirong Zeng, Lionel C. Kimerling, and John D. Joannopoulos. Improving thin-film crystalline silicon solar cell efficiencies with photonic crystals. *Opt. Express*, 15(25):16986–17000, December 2007.

[189] L. Zeng, Y. Yi, C. Hong, J. Liu, N. Feng, X. Duan, L. C. Kimerling, and B. A. Alamariu. Efficiency enhancement in si solar cells by textured

photonic crystal back reflector. *Applied Physics Letters*, 89(11):111111, September 2006.

[190] Christian Seassal, Yeonsang Park, Alain Fave, Emmanuel Drouard, Erwann Fourmond, Anne Kaminski, Mustapha Lemiti, Xavier Letartre, and Pierre Viktorovitch. Photonic crystal assisted ultra-thin silicon photovoltaic solar cell. volume 7002, pages 700207–700207–8, 2008.

[191] B. S. Cheng, C. H. Chiu, K. J. Huang, C. F. Lai, H. C. Kuo, C. H. Lin, T. C. Lu, S. C. Wang, and C. C. Yu. Enhanced light extraction of InGaN-based green LEDs by nano-imprinted 2D photonic crystal pattern. *Semicond. Sci. Technol.*, 23(5):055002, May 2008.

[192] J. Shakya, K. H. Kim, J. Y. Lin, and H. X. Jiang. Enhanced light extraction in III-nitride ultraviolet photonic crystal light-emitting diodes. *Applied Physics Letters*, 85(1):142–144, June 2004.

[193] Kyung-Hyun Kim, Jae-Heon Shin, Nae-Man Park, Chul Huh, Tae-Youb Kim, Kwan-Sik Cho, Jong Cheol Hong, and Gun Yong Sung. Enhancement of light extraction from a silicon quantum dot light-emitting diode containing a rugged surface pattern. *Applied Physics Letters*, 89(19):191120, November 2006.

[194] P.S. Dutta. High efficiency solar photovoltaic and thermo-photovoltaic device technologies. In *International Workshop on Physics of Semiconductor Devices, 2007. IWPSD 2007*, pages 828–828, December 2007.

[195] R Biswas and D Zhou. In *Mater. Res. Soc. Symp. Proc.*, volume 989, pages 35–40, 2007.

[196] K. R. Catchpole and M. A. Green. A conceptual model of light coupling by pillar diffraction gratings. *Journal of Applied Physics*, 101(6):063105, March 2007.

[197] Y. Kanamori, M. Sasaki, and K. Hane. Broadband antireflection gratings fabricated upon silicon substrates. *Opt. Lett.*, 24(20):1422–1424, October 1999.

[198] Y. Kanamori, E. Roy, and Y. Chen. Antireflection sub-wavelength gratings fabricated by spin-coating replication. *Microelectronic Engineering*, 7879:287–293, March 2005.

[199] Steven G. Johnson, Shanhui Fan, Pierre R. Villeneuve, J. D. Joannopoulos, and L. A. Kolodziejski. Guided modes in photonic crystal slabs. *Phys. Rev. B*, 60(8):5751–5758, August 1999.